

A multi-measure approach for assessing the performance of fMRI preprocessing strategies in resting-state functional connectivity

Michalis Kassinos¹, Georgios D. Mitsis²

¹Graduate Program in Biological and Biomedical Engineering, McGill University, Montreal, QC, Canada

²Department of Bioengineering, McGill University, Montreal, QC, Canada

Abstract

1 It is well established that head motion and physiological processes (e.g. cardiac and breathing activity) should be taken
2 into consideration when analyzing and interpreting results in fMRI studies. However, even though recent studies aimed
3 to evaluate the performance of different preprocessing pipelines there is still no consensus on the *optimal* strategy. This
4 is partly due to the fact that the quality control (QC) metrics used to evaluate differences in performance across pipelines
5 have often yielded contradictory results. Furthermore, preprocessing techniques based on physiological recordings or
6 data decomposition techniques (e.g. aCompCor) have not been comprehensively examined. Here, to address the
7 aforementioned issues, we propose a framework that summarizes the scores from eight previously proposed and novel
8 QC metrics to a reduced set of two QC metrics that reflect the signal-to-noise ratio and the reduction in motion artifacts
9 and biases in the preprocessed fMRI data. Using this framework, we evaluate the performance of three commonly used
10 practices on the quality of data: 1) Removal of nuisance regressors from fMRI data, 2) discarding motion-contaminated
11 volumes (i.e., scrubbing) before regression, and 3) low-pass filtering the data and the nuisance regressors before their
12 removal. Using resting-state fMRI data from the Human Connectome Project, we show that the scores of the examined
13 QC metrics improve the most when the global signal (GS) and about 17% of principal components from white matter
14 (WM) are removed from the data. Finally, we observe a small further improvement with low-pass filtering at 0.20 Hz
15 and milder variants of WM denoising, but not with scrubbing.

16
17 **Keywords:** aCompCor; physiological noise; fMRI artifacts; noise correction techniques; FIX; motion biases

18 19 Corresponding author:

20 Michalis Kassinos,
21 Graduate Program in Biological and Biomedical Engineering, McGill University,
22 350 McConnell Engineering Building,
23 3480 University Street, Montreal,
24 QC, H3A 0E9, Canada.
25 E-mail address: michalis.kassinopoulos@mail.mcgill.ca
26

27 1. Introduction

28 Functional connectivity (FC) using resting-state functional magnetic resonance imaging (fMRI) has attracted much
29 attention since Biswal and colleagues first demonstrated that, during rest, the blood-oxygen-level-dependent (BOLD)
30 signals in distinct areas of the somatomotor network are temporally correlated (Biswal et al., 1995). Strategies for
31 studying resting-state FC have advanced in the last two decades, allowing the identification of large-scale functional
32 networks, termed resting-state networks (RSNs; Fox et al., 2005; Smith et al., 2013b) that are also known to activate (or
33 deactivate in the case of the default mode network) on a range of tasks (Raichle et al., 2001; Smith et al., 2009). The
34 whole-brain functional connectivity (FC) is similar across subjects but at the same time has a subject-specific component
35 as well. (Finn et al., 2015). FC estimates have been shown to predict behavioral measures in individuals (Smith et al.,
36 2015), while differences in FC have been reported in patients with a range of cerebrovascular and mental disorders
37 compared to healthy subjects (Demirtaş et al., 2016; Leonardi et al., 2013; Woodward and Cascio, 2015). These findings
38 suggest that FC has the potential to improve our understanding regarding the functional organization over development,
39 aging, and diseases states, as well as assist in the development of new biomarkers.

40 However, a main problem in fMRI is that significant variance on the BOLD signal is driven by head motion, which has
41 been shown to have severe consequences on FC studies (Power et al., 2015; Satterthwaite et al., 2019). Motion artifacts
42 tend to be more similar in nearby regions compared to distant regions (Power et al., 2012; Satterthwaite et al., 2012; van
43 Dijk et al., 2012). As a result, correlations between regions that are close to each other (short-distance correlations) tend
44 to be inflated by motion more compared to distant regions (long-distance correlations; see for example Fig. 5 in
45 Satterthwaite et al., 2013). Consequently, in studies comparing differences in FC between populations that exhibit
46 different levels of motion, motion artifacts can cause artificial differences in FC between the examined populations.
47 Therefore, this should be carefully considered in the preprocessing and analysis of the data. This phenomenon is
48 particularly problematic for studies of development, aging and disease as children, elderly and patients tend to move
49 more during the scan than young or control subjects (Power et al., 2015).

50 Importantly, confounds in fMRI arise also from physiological noise (Caballero-Gaudes and Reynolds, 2017; Liu, 2016;
51 Murphy et al., 2013). Cardiac pulsatility in large vessels caused by cardiac-related pressure changes generates small
52 movements in and around large vessels. In turn, these movements introduce fast pseudo-periodic fluctuations (~1 Hz) in
53 the BOLD signal (Dagli et al., 1999), particularly in areas around the brainstem as well as areas in the superior sagittal
54 sinus and lateral sulcus. Similarly, breathing motion introduces high-frequency artifacts (~0.3 Hz) particularly at the
55 edges of the brain. Slow-frequency fluctuations in heart rate and breathing pattern (<0.1 Hz) are also typically observed
56 during rest which have a direct effect on the levels of oxygenated hemoglobin in the brain (Birn et al., 2006; Chang et
57 al., 2009; Kassinopoulos and Mitsis, 2021, 2019; Shmueli et al., 2007). As a result, they affect widespread regions in the
58 gray matter (GM). Group-level statistical maps generated in our previous work with areas affected by the aforementioned
59 physiological processes are available on <https://neurovault.org/collections/5654/> (Fig. 12 in Kassinopoulos and Mitsis,
60 2019). Finally, widespread regions in GM are also prone to artifacts induced by slow spontaneous fluctuations in levels
61 of arterial carbon dioxide (Prokopiou et al., 2019; Wise et al., 2004) and blood pressure (Whittaker et al., 2019). fMRI
62 fluctuations induced by changes in physiological signals are of particular concern as there is accumulating evidence that
63 physiological processes can considerably affect FC estimates if not taken into account during the preprocessing stage
64 (Birn, 2012; Birn et al., 2008a; Chang and Glover, 2009; Chen et al., 2020; Tong et al., 2019).

65 Several noise correction techniques (NCTs) have been proposed to correct for head motion artifacts and physiological
66 noise that can be classified as model-based or model-free techniques. In the case of head motion, model-based techniques
67 are based on the motion parameters (MPs) estimated from volume realignment performed in the initial steps of
68 preprocessing. Three translational and three rotational displacement parameters are estimated from volume realignment
69 that describe the rigid-body movement of head in space, yielding in total 6 MPs. The most common practice used in FC
70 studies to account for motion is to remove the 6 MPs from the data through linear regression (Power et al., 2015).
71 Sometimes the derivatives of the 6 MPs or even the squared terms of these 12 time series are also removed from the data
72 (Satterthwaite et al., 2013). Another practice employed in recent studies, termed scrubbing, is to identify volumes

73 contaminated by strong motion artifacts and discard them from the data or replace them with values from the adjacent
74 volumes using interpolation (Lemieux et al., 2007; Power et al., 2015).

75 With regards to physiological noise, model-based techniques utilize physiological recordings collected during the fMRI
76 scan. Typically, cardiac and breathing activity are recorded through a pulse oximeter and a respiratory bellow
77 respectively, and are used to model their associated artifacts. The RETROICOR model proposed by Glover et al. (2000)
78 employs the physiological recordings to generate nuisance regressors of sinusoidal signals that are in phase with the
79 cardiac and breathing cycle. Subsequently, the extracted nuisance regressors are removed from the data through linear
80 regression to account for artifacts related to cardiac pulsatility and breathing motion. Similarly, the convolution models
81 proposed by Birn et al. (2008) and Chang et al. (2009) employ the physiological signals to extract heart rate and
82 respiratory measures which are subsequently convolved with the so-called cardiac and respiration response functions.
83 The outputs of these convolutions are used as nuisance regressors to account for the effects of heart rate and breathing
84 (Birn et al., 2008b, 2006; Chang et al., 2009; Kassinopoulos and Mitsis, 2019).

85 An alternative option for noise correction in fMRI are model-free techniques that, in contrast to model-based techniques,
86 do not require external physiological recordings and, have the theoretical benefit to be independent of a pre-established
87 model. Some model-free techniques are based on principal component analysis (PCA) or independent component
88 analysis (ICA), which decompose the fMRI data into a number of components (Behzadi et al., 2007; Perlberg et al.,
89 2007; Pruim et al., 2015b; Salimi-Khorshidi et al., 2014). Following this, components associated to noise are identified
90 based on criteria such as their spatial pattern or frequency content and are subsequently removed from the data.
91 Furthermore, low-pass filtering at about 0.08 Hz is commonly used to remove high-frequency noise as RSNs are known
92 to exhibit slow oscillations below 0.1 Hz (Damoiseaux et al., 2006). Finally, the mean time series across voxels in the
93 whole brain, referred to as global signal (GS), as well as mean time series from voxels in the three tissue compartments,
94 GM, white matter (WM) and cerebrospinal fluid (CSF), are sometimes considered as nuisance regressors to account for
95 global artifacts (Power et al., 2017).

96 Even though combining a variety of NCTs and removing a large set of nuisance regressors from the data may effectively
97 suppress the effects of motion and physiological noise, this approach also leads to a reduction in the degrees of freedom
98 in the data and potentially a loss in the signal of interest. Due to this, the set of regressors chosen for a particular dataset
99 needs to be considered in conjunction with the degrees of freedom in the data, which in turn depend on the duration of
100 the data and sampling frequency. Importantly, preprocessing steps that often precede the removal of nuisance regressors,
101 such as temporal filtering and scrubbing, can also diminish the effective degrees of freedom in the data and increase the
102 likelihood for spurious connectivity (Bright et al., 2017; Yan et al., 2013), which further complicates the task of choosing
103 the *optimal* preprocessing pipeline.

104 Recent studies have attempted to compare the performance of a variety of NCTs as well as preprocessing pipelines that
105 consist of a combination of techniques mentioned earlier (Birn et al., 2014; Burgess et al., 2016; Ciric et al., 2017; Parkes
106 et al., 2018). A number of quality control (QC) metrics reflecting properties such as the identifiability of RSNs or the
107 mitigation of motion effects were used in these studies. However, a common finding in these studies is that the scores
108 obtained from the QC metrics for the examined NCTs or pipelines often yielded contradictory results. For example,
109 pipelines yielding the highest score in terms of RSN identifiability were found to be less successful in reducing motion
110 artifacts (Ciric et al., 2017). Moreover, even though there is strong evidence that model-free techniques based on PCA
111 or ICA are able to reduce artifacts due to head motion or physiological noise (Behzadi et al., 2007; Muschelli et al., 2014;
112 Pruim et al., 2015a; Salimi-Khorshidi et al., 2014), it is still an open question whether combining them with model-
113 based techniques can result in superior performance.

114 In this work, we propose a framework for summarizing the scores of different signal and motion-related QC metrics by
115 weighting these metrics according to their sensitivity. We define the sensitivity of a metric as the consistency of its scores
116 across subgroups of subjects with similar levels of motion. Subsequently, using this multi-measure approach for assessing
117 fMRI data quality, we compare the performance of several NCTs on multi-session resting-state fMRI data provided by
118 the Human Connectome Project (Van Essen et al., 2013). The comparison of NCTs is done in a series of stages that

119 allows us to better understand the role of each technique (e.g. low-pass filtering) in noise correction. With respect to
120 model-free approaches, we examine FIX (“fMRIB’s ICA-based X-noiseifier”; Salimi-Khorshidi et al., 2014) as well as
121 variants of aCompCor (Behzadi et al., 2007). FIX consists of whole-brain ICA decomposition followed by removal of
122 noisy components identified using a multi-level classifier (Salimi-Khorshidi et al., 2014). Besides evaluating the
123 performance of the original aCompCor approach, we examine whether removing more components than previously
124 suggested, either from WM or CSF, is beneficial. Finally, for the variant of aCompCor that exhibits the best improvement
125 in QC scores, we investigate the additional benefit of: 1) removing nuisance regressors derived from the MPs and
126 physiological recordings, 2) excluding motion-contaminated volumes from the analysis, and 3) performing low-pass
127 filtering before the removal of regressors.

128 **2. Methodology**

129 Unless stated otherwise, the preprocessing and analysis described below were performed in Matlab (R2018b; Mathworks,
130 Natick MA).

131 **2.1 Human Connectome Project (HCP) Dataset**

132 We used resting-state scans from the HCP S1200 release (Glasser et al., 2016; Van Essen et al., 2013). The HCP dataset
133 includes, among others, resting-state (eyes-open and fixation on a cross-hair) data from healthy young individuals (age
134 range: 22-35 years) acquired on two different days. On each day, two 15-minute scans were collected. We refer to the
135 two scans collected on days 1 and 2 as R1a/R1b and R2a/R2b, respectively. fMRI acquisition was performed with a
136 multiband factor of 8, spatial resolution of 2 mm isotropic voxels, and a repetition time TR of 0.72 s (Glasser et al.,
137 2013).

138 The minimal preprocessing pipeline for the resting-state HCP dataset is described in Glasser et al. (2013). In brief, the
139 pipeline includes gradient-nonlinearity-induced distortion correction, motion correction, EPI image distortion correction,
140 non-linear registration to MNI space and mild high-pass (2000 s) temporal filtering. The motion parameters are included
141 in the database for further correction of motion artifacts. Apart from the minimally preprocessed data, the HCP provides
142 a cleaned version of the data whereby time series corresponding to ICA components that FIX classified as noisy as well
143 as 24 motion-related regressors (i.e., the 6 MPs estimated during volume realignment along with their temporal
144 derivatives and the squared terms of these 12 time series) were regressed out of the data (Smith et al., 2013a). The cleaned
145 fMRI data are referred to later as FIX-denoised data.

146 Both minimally-preprocessed and FIX-denoised data are available in volumetric MNI152 and grayordinate space. The
147 grayordinate space combines cortical surface time series and subcortical volume time series from GM, and has more
148 accurate spatial correspondence across subjects than volumetrically aligned data (Glasser et al., 2013; Glasser et al.,
149 2016), particularly when the fMRI data have high spatial resolution such as in HCP.

150 In the present work, we examined minimally-preprocessed and FIX-denoised data in both volumetric and grayordinate
151 (MSMall registration; Glasser et al., 2016) space from 390 subjects with good quality physiological signals (cardiac and
152 breathing waveforms) in all four scans, as assessed by visual inspection. The cardiac and breathing signals were collected
153 with a photoplethysmograph and respiratory bellow respectively.

154 **2.2 Parcellation of the fMRI data**

155 The following three fMRI-based atlases were considered in this study:

- 156 a. The Gordon atlas (Gordon et al., 2016): This atlas is composed of 333 cortical regions with 286 parcels belonging
157 to one of twelve large-scale networks and the rest being unassigned. Only the 286 parcels that are assigned to
158 networks were considered in the present study.
- 159 b. The Seitzman atlas (Seitzman et al., 2020): This atlas consists of 239 cortical, 34 subcortical and 27 cerebellar
160 volumetric parcels. Among the 300 parcels, 285 parcels are assigned to one of thirteen large-scale networks and
161 only these ones were considered here.
- 162 c. The MIST atlas (Urchs et al., 2017): The MIST atlas is available in several resolutions ranging from 7 to 444
163 parcels. In this study, we considered the MIST_444 parcellation that consists of 444 regions from the whole
164 brain that are assigned to the 7 networks of the MIST_7 parcellation.

165 All three atlases were defined on resting-state fMRI data and all (MIST) or the majority of (Gordon and Seitzman) their
166 parcels were assigned to large-scale networks. The association of the parcels to networks is required for three of the
167 quality control (QC) metrics described later (i.e., *FCC*, *FD-FCC* and *ICCC*). Therefore, as mentioned earlier, parcels that
168 do not belong to a specific network were excluded from the study.

169 Before the parcellation, in the case of the Seitzman atlas, we performed spatial smoothing on the fMRI data with a
170 Gaussian smoothing kernel of 5 mm full width half maximum (FWHM). Spatial smoothing is commonly done on fMRI
171 data to suppress spatially random noise and enhance the signal-to-noise ratio (SNR). However, when mapping the fMRI
172 data to a parcellation with relatively large parcels such as the parcels in the Gordon and MIST atlases, spatial smoothing
173 is implicitly done. Therefore, we chose to omit spatial smoothing for these two atlases. We performed spatial smoothing
174 before conducting the mapping to the Seitzman atlas because this atlas consists of small spherical ROIs of 8 mm diameter
175 (Seitzman et al., 2020) and, thus, if spatial smoothing is not performed, the parcel time series extracted from these ROIs
176 may suffer from low SNR.

177 To speed up the preprocessing step, the regression of the nuisance regressors for each pipeline was performed in a parcel-
178 rather than voxel-wise manner. In other words, the minimally-preprocessed and FIX-denoised fMRI data were first
179 mapped to parcel time series by averaging the time series of all voxels or vertices within a parcel and, subsequently, the
180 resulted parcel time series were corrected for noise using the techniques described later. The mapping of the fMRI data
181 to the Gordon parcel space was done using the fMRI data in the grayordinate form, while the mapping to the Seitzman
182 and MIST parcel space was done using the volumetric form of the fMRI data. Finally, to mitigate the influence of spurious
183 low-frequency fluctuations on estimations of correlations, all parcel time series were high-pass filtered at 0.008 Hz,
184 complying with the rule of thumb proposed in Leonardi & Van De Ville (2015) of a high-pass cut-off frequency $f_c \geq$
185 $1/(window\ length) = 1/(15\ min)$.

186 2.3 Tissue-based regressors

187 The T1-weighted (T1w) images of each subject are provided in the HCP database in both the native and MNI152 space.
188 To extract the tissue-based regressors used by several pipelines examined here, we initially performed tissue
189 segmentation on the T1w images in the MNI152 space using FAST (FMRIB's Automated Segmentation Tool) in FSL
190 5.0.9, generating probabilistic maps for the GM, WM and CSF compartments (Zhang et al., 2001). Subsequently, the
191 GM, WM and CSF binary masks were defined as follows: voxels with a probability above 0.25 of belonging to GM were
192 assigned to GM, while the same was done for WM and CSF for probability values of 0.9 and 0.8 respectively. The choice
193 of the threshold values was made based on visual inspection while overlaying the binary maps on the T1w images.
194 Finally, based on these maps, the global signal was defined as the mean fMRI time series across all voxels within GM.
195 In addition, PCA regressors were obtained separately for voxels in WM and CSF. The GS and PCA regressors were
196 derived from both the minimally-preprocessed and FIX-denoised fMRI data in the volumetric space.

197 2.4 Model-based regressors related to motion and physiological fluctuations

198 An important goal of this study was to quantify the effect of model-based NCTs with respect to the quality of the fMRI
199 data for atlas-based FC analysis and how they contribute to fMRI denoising when combined with tissue-based regressors.
200 Therefore, for each scan the following four sets of model-based regressors were considered:

- 201 **a. Motion parameters (MPs; 24 regressors):** The 6 MPs derived from the volume realignment during the minimal
202 preprocessing, as well as their temporal derivatives, are provided in the HCP database. In addition to the 12
203 aforementioned time series (12 MPs), we derived their squared terms, yielding in total 24 motion parameters (24
204 MPs).
- 205 **b. Cardiac regressors (6 regressors):** The cardiac regressors were modelled using a 3rd order RETROICOR model
206 (Glover et al., 2000) based on the cardiac signal of each scan. These regressors aimed at accounting for the effect
207 of cardiac pulsatility on the fMRI time series.
- 208 **c. Breathing regressors (6 regressors):** The breathing regressors were modelled using a 3rd order RETROICOR
209 model based on the breathing signal of each scan (Glover et al., 2000). These regressors aimed at accounting for
210 the effect of breathing motion.
- 211 **d. Systemic low frequency oscillations (SLFOs; 1 regressor):** The SLFOs refer to non-neuronal physiological
212 BOLD fluctuations induced by changes in heart rate and breathing patterns, which were modelled following the
213 framework proposed in our previous work (Kassinopoulos and Mitsis, 2019). The heart rate and respiratory flow

214 extracted from the cardiac and breathing signals of each scan were convolved with scan-specific cardiac and
215 respiratory response functions and the outputs of these convolutions were linearly combined to obtain the
216 corresponding SLFOs. To estimate the scan-specific physiological response functions and determine the linear
217 combination of heart rate- and respiratory flow- related components needed to model the SLFOs, numerical
218 optimization techniques that maximize the fit of the model output (i.e., the SLFOs-related time series) to the GS
219 were employed. The GS was used as a fitting target as it is strongly driven by fluctuations in heart rate and
220 breathing patterns. For more information on this method we refer the reader to Kassinosopoulos and Mitsis (2019).
221 The codes for the estimation of SLFOs can be found on https://github.com/mkassinopoulos/PRF_estimation.

222 Even though we selected subjects with good quality of physiological recordings, it was still important to preprocess both
223 the cardiac and breathing signals to ensure the extraction of accurate heart rate and respiratory flow traces. To this end,
224 we applied temporal filtering and correction for outliers as described in Kassinosopoulos and Mitsis (2019). Moreover, as
225 the effect of HR and breathing pattern variations on the fMRI BOLD signal is considered to last about half a minute
226 (Kassinosopoulos and Mitsis, 2019) physiological recordings for at least half a minute before the beginning of the fMRI
227 acquisition would be required to account for these effects. However, due to the lack of data at this period, the first 40
228 image volumes were disregarded from the fMRI data, while the corresponding physiological data were retained so that
229 the SLFOs could be modelled from the beginning of the considered fMRI scan.

230 2.5 Framework data quality indices

231 A common index of quality in fMRI data is the framewise displacement (*FD*) introduced by Power et al. (2012). This
232 index is defined as the sum of absolute values of the first derivatives of the 6 motion (realignment) parameters, after
233 converting the rotational parameters to translational displacements on a sphere of radius 50 mm. *FD* is essentially a time
234 series that reflects the extent of motion during the scan. In this work, *FD* was used for six QC metrics that are described
235 in Section 2.6 to quantify the degree of motion artifacts and biases in the preprocessed data. In addition, it was used to
236 identify volumes associated with relatively large *FD* values that are presumably corrupted by motion, and examine the
237 effect of scrubbing, whereby these flagged volumes are discarded before any further analysis (Section 2.8.4).

238 Another widely used framewise index of data quality is *DVARS* (Derivative of rms VARIance over voxelS) which
239 measures how much the intensity of an fMRI volume varies at each timepoint compared to the previous point (Power et
240 al., 2012). *DVARS* is defined as the spatial root mean square of the voxel time series after they are temporally
241 differentiated. While *DVARS* is obtained from the fMRI time series and is not directly related to head movement, it
242 demonstrates similar trends with *FD* (Power et al., 2012; Suppl. Fig. 10-Suppl. Fig. 11). Similarly to *FD*, *DVARS* was
243 used in this study for two QC metrics related to the effect of motion, as well as to flag volumes corrupted by motion.

245 2.6 Quality control (QC) metrics

246 Nine QC metrics that are described below were used to evaluate the data quality with respect to the identifiability of
247 large-scale networks and the presence of motion-related artifacts and biases. *FCC*, *FD-FCC*, *ICCC*, *FD-FDDVARS* and
248 *FD-MFC* are novel metrics proposed in the present study whereas the rest of the four metrics were proposed in previous
249 studies. Pearson (full) correlation was calculated between the time series of each pair of parcels resulting in an FC matrix
250 per scan, pipeline and atlas. Apart from *FDDVARS* and *FD-FDDVARS*, all other metrics are based on the FC matrix.
251 Note that throughout the text we refer to a pair of parcels as *edge*. Apart from *MICC* and *ICCC*, for all other metrics, only
252 the first of the four scans was considered from each subject. This was done to facilitate the comparison of the scores of
253 those metrics with scores that would have been obtained in conventional datasets which often consist of a single resting-
254 state fMRI scan per subject of 10-15 minutes duration. *MICC* and *ICCC* were calculated using all four scans from each
255 subject, as by definition these two metrics require repeated measures (scans).

257 *Functional connectivity contrast (FCC):*

258 A main property of the three parcellations used in this study is that each parcel is assigned to a specific large-scale
259 network, which implicitly suggests that on average a pair of parcels belonging to the same network, also called within-
260 network edge (WNE), should exhibit a higher (towards positive) correlation value compared to a pair of parcels from
261 different networks (between-networks edge; BNE). Based on this property, we assumed that if a pipeline improves the
262 signal-to-noise ratio (SNR) in the data, it should also lead to a larger difference between correlation values corresponding
263 to WNEs and BNEs. To quantify the extent to which WNEs had higher correlation values than BNEs after applying a
264 preprocessing pipeline on the data, we used the metric FC contrast (*FCC*). *FCC* was defined as the *Z*-statistic of the
265 Wilcoxon rank-sum test related to the null hypothesis that WNEs and BNEs in the FC matrix are samples from continuous
266 distributions with equal medians (note that the real values rather than the absolute values were used in the calculation of
267 the *Z*-statistic). In other words, higher values of *FCC* correspond to higher (towards positive) correlation values for WNEs
268 as compared to BNEs. Furthermore, for the optimal pipeline found in this work, we quantified the identifiability of each
269 of the networks separately using the same metric but considering only WNEs belonging to the network of interest rather
270 than WNEs from all networks when comparing WNEs with BNEs.

271 *FD-FCC:*

272 While it is desired to improve the *FCC* score for the data of each scan, at the same time it is desired that low-motion and
273 high-motion scans demonstrate similar *FCC* scores. Therefore, *FD-FCC* was defined as the correlation between the mean
274 *FD* and *FCC* across scans and was used in this work to assess potential biases due to different levels of motion between
275 scans.

276 *Median of Intraclass correlation values (MICC):*

277 Intraclass correlation (*ICC*) is a widely used metric in statistics to assess how reproducible measurements of the same
278 quantity are across different observers or instruments (Shrout and Fleiss, 1979). Similar to previous studies evaluating
279 the performance of preprocessing strategies in fMRI, we have used *ICC* to assess test-retest reliability across the four
280 sessions of each subject in whole-brain FC estimates (Birn et al., 2014; Parkes et al., 2018; Shirer et al., 2015). For a pair
281 of parcels *i* and *j*, $ICC_{i,j}$ was defined as

$$ICC_{i,j} = \frac{MS_b - MS_w}{MS_b + (k-1)MS_w}, \quad [1]$$

282 where *k* is the number of scans per subject (4), MS_b is the between-subject mean square of correlation values between
283 parcels *i* and *j*, and MS_w is the within-subject mean square of correlation values for the same pair of parcels. The *MICC*
284 score assigned to each pipeline for the assessment of data quality was defined as the median of $ICC_{i,j}$ across all edges.

285 *ICC contrast (ICCC):*

286 A common finding from previous studies is that *MICC* values tend to drop when a preprocessing pipeline is applied (Birn
287 et al., 2014; Parkes et al., 2018; Shirer et al., 2015). This finding suggests that artifacts in fMRI data have high subject-
288 specificity and, thus, when the artifacts are reduced after the preprocessing, *MICC* decreases as well. In addition, Birn et
289 al. (2014) have observed that the 200 most significant connections exhibited higher mean *ICC* after preprocessing as
290 compared to the mean *ICC* across all (16100) connections. Similarly, we also observed that WNEs that exhibited higher
291 connectivity strength than BNEs also exhibited higher *ICC* values. Based on this observation, in the present study we
292 propose a new metric termed *ICC* contrast (*ICCC*), which quantifies the difference in $ICC_{i,j}$ values between WNEs and
293 BNEs. The assumption behind *ICCC* is that only WNEs should demonstrate high subject specificity. Similarly to *FCC*,
294 *ICCC* was defined as the *Z*-statistic of the Wilcoxon rank-sum test related to the null hypothesis that WNEs and BNEs in
295 the *ICC* matrix are samples from continuous distributions with equal medians. In other words, a high value of *ICCC*
296 suggests that WNEs have higher $ICC_{i,j}$ values compared to BNEs.

297

298 *FDDVARS*:

299 To assess the presence of motion artifacts in the parcel time series after preprocessing, we calculated the Pearson
300 correlation coefficient between *FD* and *DVARS* (Muschelli et al., 2014). Even though *FD* was estimated only once based
301 on the motion (realignment) parameters, the framewise data quality index *DVARS* was estimated for each pipeline
302 separately using the parcel (instead of voxel) time series after the preprocessing, as described in Section 2.5 (note that
303 the parcel-wise *DVARS* considered here was computed across all parcels over the whole-brain and should not be confused
304 with the parcel-wise *DVARS* considered in Muschelli et al. (2014) that was computed across voxels within a parcel).
305 Even though the parcel-wise and voxel-wise *DVARS* values were similar (mean correlation of 0.56 ± 0.21), they were not
306 identical (Suppl. Fig. 10-Suppl. Fig. 11). The parcel time series, defined as the average time series of voxels assigned to
307 each parcel, exhibited lower levels of noise compared to voxel time series and, as a consequence, the parcel *FDDVARS*
308 values were also found to be lower (Suppl. Fig. 10-Suppl. Fig. 11). And as it is common practice to conduct the FC
309 analysis at the parcel-level, we performed the assessment of data quality using the parcel *FDDVARS* values. The
310 *FDDVARS* score assigned to each pipeline was obtained by initially calculating the correlation value between *FD* and
311 *DVARS* for each scan and then averaging the correlations across all scans.

312 *FD-FDDVARS*:

313 While the *FDDVARS* score reflects the extent to which motion artifacts are present in the data of a given scan, a low
314 mean value of *FDDVARS* within a group of scans does not necessarily imply that the motion-related biases across scans
315 in the FC estimates are also low. High-motion scans are contaminated by more severe motion artifacts compared to low-
316 motion scans, which has been shown to systematically bias the estimated FC matrices (Power et al., 2015). Even though
317 a preprocessing strategy may reduce the motion artifacts in both high- and low-motion scans, if in the preprocessed data
318 there are still differences in the levels of motion artifacts between the two groups, this would result in a systematic bias
319 for the FC estimates of these groups. To assess the presence of motion-related biases, we used the QC metric *FD-*
320 *FDDVARS*, which was defined as the correlation between the mean *FD* and *FDDVARS* across scans.

321 *FDFC_{median}*:

322 For a pair of parcels *i* and *j*, *FDFC_{i,j}* was defined as the correlation between the Pearson correlation coefficient of this
323 pair (i.e., *FC_{i,j}*) and the mean *FD* across scans. To assess the quality of data with respect to motion-related biases in FC,
324 each pipeline was assigned an *FDFC_{median}* score that corresponded to the median absolute *FDFC_{i,j}* across all edges
325 (Parkes et al., 2018; Power et al., 2012).

326 *FDFC_{dist}*:

327 Earlier studies on the effect of motion in fMRI have shown that, in the case of raw data, the correlation values for short-
328 distance edges are inflated to a greater extent due to motion compared to long-distance edges (Power et al., 2012;
329 Satterthwaite et al., 2013). An interpretation for this distance-dependent effect is that when motion occurs, nearby voxels
330 are typically affected by similar displacements and, thus, present similar spin-history artifacts as well. And even though
331 distant voxels may also exhibit similar displacements that can lead to widespread artifacts, these artifacts are not as
332 pronounced as in the case of nearby voxels (Power et al., 2015). As these distance-dependent motion artifacts are
333 generally considered undesirable, the quality control metric *FDFC_{dist}* is commonly used to quantify the degree of this
334 dependence and assess the capability of a preprocessing strategy to mitigate it (Circic et al., 2018, 2017; Muschelli et al.,
335 2014; Parkes et al., 2018; Power et al., 2015, 2012; Satterthwaite et al., 2019, 2012). *FDFC_{dist}* is defined as the correlation
336 between the *FDFC_{i,j}* value, as defined for the previous QC metric (*FDFC_{median}*) and the Euclidean distance between
337 parcels *i* and *j*, across all edges (Circic et al., 2017; Parkes et al., 2018).

338 *FD – Mean FC (FD-MFC)*:

339 The metric *FDFC_{median}* inherently assumes that the Pearson correlation of an edge is affected by motion in the same
340 way across subjects. However, considering that differences in brain anatomy across subjects exist (Bijsterbosch et al.,

2018), we can not necessarily assume that motion affects edge-wise FC estimates in the exact same way across subjects. Therefore, to assess the effect of motion on FC estimates, without the aforementioned assumption, we propose the *FD-MFC* metric which is defined as follows: First, the mean of all Pearson correlations in the FC matrix (*MFC*) is estimated for each scan separately (considering only unique pairs of parcels) and, subsequently, the correlation between the mean *FD* and *MFC* across all scans (subjects) is obtained.

2.7 Normalization of QC metrics

The nine QC metrics described in [Session 2.6](#) can be categorized into signal-related and motion-related metrics. The signal-related metrics (*FCC*, *MICC* and *ICCC*) reflect the SNR of the data and are expected to yield low scores for data that have not been preprocessed, as high levels of artifacts are likely to obscure the signal of interest. They are also expected to yield low scores for data to which a very aggressive pipeline is applied and the signal of interest is lost. On the other hand, relatively high scores of signal-related metrics would be expected for data whereby a good pipeline is applied and artifacts are reduced while the signal of interest is preserved. Motion-related metrics are expected to yield high absolute scores for data that have not been preprocessed, indicating the presence of motion artifacts or biases, whereas for gradually more aggressive pipelines, these scores are expected to approach zero, reflecting the reduction of motion artifacts and biases.

As the goal of a preprocessing strategy is to remove artifacts while also preserving the signal of interest, ideally a pipeline that yields high scores in signal-related QC metrics and low scores in motion-related metrics would be preferred. However, due to the fact that each QC metric is based on different assumptions and some metrics are based on Pearson correlation while other ones are based on the Wilcoxon rank-sum test, each metric illustrates a different trend across pipelines and yields a different range of scores (see for example [Fig. 2](#)) making the selection of the optimal pipeline difficult. Therefore, to overcome this potential drawback, we followed the following steps:

1. First, we randomly split the 390 subjects to 10 groups of 39 subjects, ensuring that the groups were characterized by similar distributions of mean *FD* values.
2. Then, the QC scores were estimated for each of the 10 groups separately. Apart from *MICC* and *ICCC*, for all other metrics, only the first of the four scans were considered from each subject to avoid estimating correlations with repeated measures. *MICC* and *ICCC* were calculated using all four scans from each subject, as by definition these two *ICC*-based metrics require repeated measures (scans). *FCC* and *FDDVARS* that are calculated on a scan basis, rather than within a group of scans, were averaged across subjects within each group. In this way, the quality of the data for a given atlas, pipeline and group of subjects was assigned with one score for each of the nine QC metrics.
3. Subsequently, all motion-related metrics were normalized to $1 - \text{abs}(x)$, where x is the score of each metric, so that, similarly to signal-related metrics, a high positive score is assigned to good quality data.
4. In the next step, the scores were expressed as *Z*-scores based on the relation $Z_{i,k,p} = \frac{x_{i,k,p} - \mu_i}{\sigma_i}$ where $x_{i,k,p}$ and $z_{i,k,p}$ are respectively the original and *Z*-score values obtained for QC i , group of subjects k and pipeline p and, μ_i and σ_i are respectively the mean and standard deviations of the scores from all groups of subjects related to the QC i obtained from the raw data. For example, considering the case where the *FCC* scores obtained from the raw data for the ten groups of subjects have a mean and standard deviation of 47.3 and 1.6 respectively, if the *FCC* score for a given pipeline (e.g. FIX) and group of subjects is 56.0, the corresponding *Z*-score for that particular pipeline and group of subjects would be 5.4 $[(56.0 - 47.3) / 1.6 = 5.4]$.
5. Subsequently, the *Z*-scores of *FCC* and *ICCC* were averaged to yield the summarized score QC_{signal} and the *Z*-scores of the 6 motion-related metrics *FD-FCC*, *FDDVARS*, *FD-FDDVARS*, *FDFC_{median}*, *FDFC_{dist}* and *FD-MFC* were averaged to yield the summarized score QC_{motion} . The *MICC* was not included in the estimation of the QC_{signal} score as it was proven to reflect subject-specificity due to noise rather than signal of interest.

385 6. Finally, the two latter summarized scores, QC_{signal} and QC_{motion} , were averaged to obtain the score for the
386 combined quality control metric CQC .

387 The normalization described here allowed us to express the scores of the QC metrics as Z-scores that reflect the relative
388 improvement in standard deviations with respect to the raw data. High Z-scores can be interpreted as the associated QC
389 metric exhibiting high sensitivity. If the QC metric for a given pipeline exhibits a high Z-score, it is very likely that in a
390 new dataset the score for the same QC metric will be better when the data are preprocessed with the same pipeline
391 compared to the raw data. After the normalization of the QC metrics, all metrics were summarized into two indices, the
392 QC_{signal} and the QC_{motion} , which, in turn, were averaged to obtain the final CQC score. While we present the results for
393 QC_{signal} and QC_{motion} apart from CQC , the choice for the *optimal* pipeline is based on the third one.

395 2.8 Noise correction techniques (NCTs)

396 We assessed the performance of a large number of preprocessing pipelines using eight QC metrics that quantify the
397 improvement in network identifiability and reduction of motion-related artifacts and biases. The pipelines consisted of
398 commonly used preprocessing strategies, namely scrubbing, temporal low-pass filtering and removal of nuisance
399 regressors through linear regression. To better understand the effect of each of the aforementioned strategies, five
400 different groups of pipelines were examined that are described in the following sections. The QC metrics used to evaluate
401 the performance of each pipeline are described in [Section 2.6](#).

402 2.8.1 Optimizing aCompCor

403 In aCompCor, PCA regressors are obtained from the WM and CSF tissues and the first five components ordered by the
404 variance explained in the WM and CSF voxel time series are used as nuisance regressors. This practice implicitly suggests
405 that the PCA regressors that explain most of the variance in WM and CSF are also the ones with the stronger association
406 to model-based nuisance regressors. To examine whether the latter is the case, we estimated the fraction of variance in
407 WM and CSF PCA regressors explained by each of the following sets of regressors: 1) 24 MPs, 2) breathing regressors,
408 3) cardiac regressors, 4) SLFOs, and 5) all the aforementioned regressors combined. In addition, we estimated the fraction
409 of variance in the model-based regressors explained by an increasing number of WM or CSF regressors (between 1 and
410 100). The estimated explained variances corresponding to each model-based regressor were averaged across regressors
411 associated with the same source of noise.

412 After confirming the hypothesis stated above, a main objective of this study was to examine the performance of WM and
413 CSF denoising independently and determine the number of regressors that improves the quality of the fMRI data the
414 most. To this end, for both noise ROIs, we considered the removal of the most significant PCA regressors with or without
415 including the GS as an additional nuisance regressor for a varying number of PCA regressors between 1 and 600 (to keep
416 the computational time low we varied the number using a logarithmic base of ten as follows:
417 1, 2, ..., 10, 20, ..., 100, 200, ..., 600). Note that each scan consisted of 1160 fMRI volumes, therefore 600 components
418 correspond to about half of the available PCA regressors. Regarding the tissue-based regressors used in aCompCor, we
419 refer to a set of regressors from WM and CSF as $WM_{(GS)}^x$ and $CSF_{(GS)}^x$, respectively, where x indicates the number of
420 PCA regressors considered from each of the two tissue compartments and the presence of the GS as superscript denotes
421 the inclusion of the GS in the set of nuisance regressors. For example, the set of regressors WM_{GS}^{200} refers to the set
422 consisting of the GS and the first 200 PCA regressors from WM. Note that the set WM_{GS}^{200} demonstrated the highest
423 improvement in QC scores and, thus, the subsequent analyses in this work investigate the possibility of further
424 improvement using additional strategies in the preprocessing along with the regression of this set.

425 2.8.2 Evaluation of data-driven NCTs

426 Typically, fMRI studies consider only data-driven regressors for the preprocessing of the data that can be a combination
427 of motion, tissue-based regressors or whole-brain component regressors (e.g., FIX). However, it is still not clear which

Table 1. Preprocessing pipelines based on data-driven approaches

Pipeline	Sets of nuisance regressors considered in the pipeline	(Related to) pipeline used in:
1	6 motion parameters (6 MPs)	—
2	12 motion parameters (12 MPs; i.e., 6 MPs plus their derivatives)	—
3	24 motion parameters (24 MPs; i.e., 12 MPs plus their squared terms)	—
4	Global signal (GS)	—
5	12 MPs, GS	—
6	WM^5 , CSF^5 (i.e., first 5 PCA regressors from white matter (WM) and first 5 PCA regressors from cerebrospinal fluid (CSF))	Behzadi et al., 2007
7	12 MPs, mean WM time-series (WM_{mean}) and mean CSF time-series (CSF_{mean})	Urchs et al., 2017
8	12 MPs, WM_{mean} , CSF_{mean} , GS	Finn et al., 2015
9	24 MPs, [GS, WM_{mean} , CSF_{mean} , plus their derivatives]	Laumann et al., 2017
10	24 MPs, [GS, WM_{mean} , CSF_{mean} , plus their derivatives and the squared terms of the 6 aforementioned time-series]	Ciric et al., 2017; Xia et al., 2018
11	<i>FIX</i> (i.e., the <i>FIX</i> -denoised data as provided from HCP)	Bijsterbosch et al., 2017; Smith et al., 2015; Zhang et al., 2018
12	FIX_{GS} (i.e., <i>FIX</i> followed by GS regression)	Burgess et al., 2016
13	<i>FIX</i> , GS, WM^5 , CSF^5	Siegel et al., 2017
14	PCA regressors needed to explain 50% of variance in WM and CSF	Muschelli et al., 2014
15	GS, WM regressors needed to explain 30% of variance	—
16	GS, WM regressors needed to explain 35% of variance	—
17	GS, WM regressors needed to explain 40% of variance	—
18	GS, WM regressors needed to explain 45% of variance	—
19	GS, WM regressors needed to explain 50% of variance	—
20	WM_{GS}^{200} (i.e., the GS and the first 200 PCA regressors from WM)	—

preprocessing strategy is the best for whole-brain FC as the number and type of regressors included in the preprocessing stage vary across studies. In the present study, a selection of pipelines used in the literature were evaluated using the QC metrics described in Section 2.6 to allow a comparison between them (Table 1). However, as the focus of this analysis was to examine the effect of the regressors *per se* rather than the entire pipeline, steps such as scrubbing (i.e., removal

of motion-contaminated volumes) or temporal low-pass filtering were omitted. In addition, several pipelines were considered in this analysis that consisted of a small number of regressors (e.g. pipelines 1-5), even though, typically, more aggressive pipelines are found in the literature. These pipelines were considered in order to better understand possible differences in QC scores yielded by more aggressive pipelines (e.g. pipelines 7 and 8).

Regarding the pipelines that involve *FIX* (i.e., pipelines 11-13), even though the HCP database provides the results from MELODIC-ICA and, thus, we could have removed noisy ICA components and further nuisance regressors from the minimally-preprocessed fMRI data in one step, we chose to remove the additional nuisance regressors from the *FIX*-denoised data found in the HCP database to be consistent with the approach taken in previous studies (Burgess et al., 2016; Siegel et al., 2017). For pipelines 12 and 13, we used the GS and WM/CSF regressors derived from the *FIX*-denoised data. Note that, as mentioned earlier, the *FIX* denoising performed in HCP included the removal of the 24 MPs.

2.8.3 Evaluation of model-based (motion and physiological) NCTs

Even though the motion parameters are indirectly derived from the data through the process of volume realignment, they do not purely correspond to motion-induced fMRI artifacts, but rather rigid-body displacements (Patriat et al., 2017).

Therefore, treating them as nuisance regressors during preprocessing inherently imposes some assumptions about the effect of motion on the fMRI time series, which may not be valid. Similarly, the efficiency of physiological regressors that are obtained from concurrent physiological recordings (e.g. cardiac and breathing signals) depends on the validity of the employed physiological response function models, as well as the quality of the recordings. Thus, an important question that needs to be addressed is whether the aforementioned model-based regressors contribute to the denoising of the fMRI data, and particularly when combined with tissue-based regressors that do not have the limitations of the model-based approaches. To this end, using the QC metrics, we evaluated 64 combinations of pipelines that employ sets of model-based and tissue-based regressors. Specifically, we considered as model-based regressors the 24 MPs, the cardiac and breathing regressors and the SLFOs regressor, while as tissue-based regressors we considered the GS and 200 PCA regressors from WM (WM_{200}).

2.8.4 Scrubbing

In the analyses preceding scrubbing, it was found that the set of nuisance regressors WM_{GS}^{200} yielded the highest QC scores. Therefore, the next question that we aimed to address is whether scrubbing can provide any further improvement in the QC scores for this specific set of regressors and at what threshold. This analysis was done both using the FD and the $DVARS$ to determine the motion-contaminated volumes that would be discarded. In the case of FD , we repeated the analysis for the values of threshold FD_{thr} 0.15, 0.20, 0.25, 0.30, 0.50, 0.80 and 1.00 mm, and in the case of $DVARS$ we considered the values of threshold $DVARS_{thr}$ 0.5, 1, 1.5, 2, 5, 10 and 20 median absolute deviations (MAD).

2.8.5 Low-pass filtering (LPF)

We also investigated whether low-pass filtering the data and removing nuisance regressors would yield higher QC scores compared to no filtering. Low-pass filtering, however, apart from removing high-frequency noise, it also leads to a substantially decreased number of degrees of freedom (Bright et al., 2017). The degrees of freedom DOF can be roughly estimated by the relation: $DOF = NV \cdot \left(\frac{f_c}{f_N}\right)$ where NV is the number of volumes, f_c is the cut-off frequency and f_N the Nyquist frequency. For instance, in our dataset, low-pass filtering at 0.08 Hz ($NV = 1160$, $f_c = \frac{1}{2TR} = 0.69$ Hz) reduces the degrees of freedom from 1160 to ~ 134 . This property suggests that removing a large set of nuisance regressors (e.g. WM_{GS}^{200}), in addition to applying a strong low-pass filter (e.g. a low-pass filter with 0.08 Hz cut-off frequency), can remove all the degrees of freedom available in the data. Given this, we examined the effect of low-pass filtering for both mild and aggressive variants of WM denoising, considering only cut-off frequencies that yield data with a minimum of 30 degrees of freedom. Specifically, we examined the sets WM_{GS}^{20} and WM_{GS}^{50} with low-pass filtering at 0.05, 0.08, 0.2, 0.3, 0.4, 0.5 and 0.6 Hz, the set WM_{GS}^{100} with values of cut-off frequency between 0.08 Hz and 0.6 Hz, as well as the set WM_{GS}^{200} with values between 0.2 and 0.6 Hz.

475 3. Results

476 Here we present results mainly for the Gordon atlas since the results between the three examined atlases did not yield
 477 significant differences. The results obtained using the Seitzman and MIST atlases can be found in the Supplementary
 478 Material.

479 3.1 Optimizing aCompCor

480 Fig. 1 shows the estimated fraction of variance in WM and CSF PCA regressors explained by various sets of model-
 481 based regressors (left panel), as well as the estimated fraction of variance explained in the sets of model-based regressors
 482 by an increasing number of WM and CSF regressors (right panel). The WM and CSF regressors were ordered with

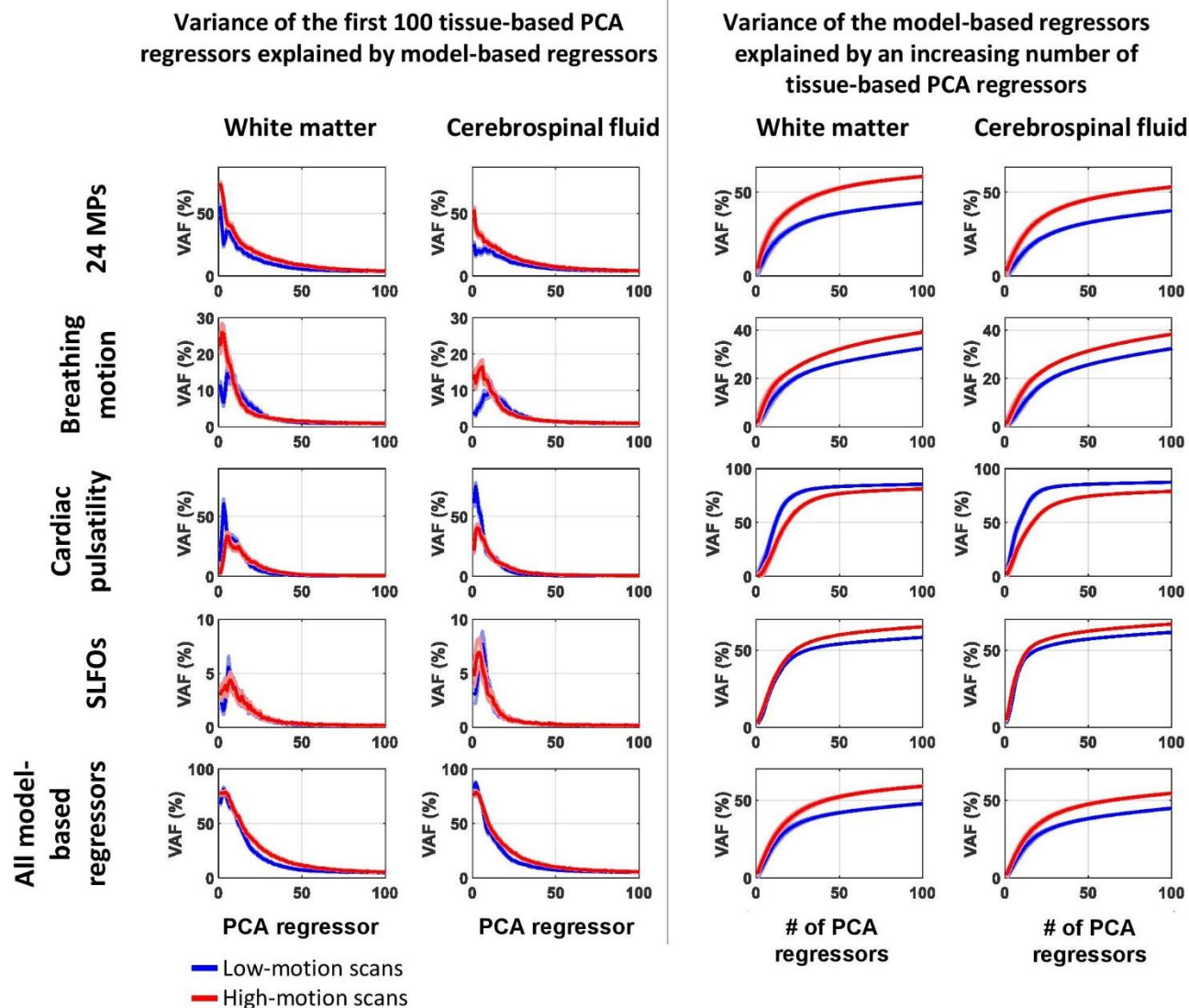


Fig. 1. Relation between model-based regressors and PCA regressors obtained from WM and CSF. Left panel (first two columns): Estimated variance explained in each of the first 100 WM and CSF PCA regressors by the set of model-based regressors stated on the left of each row (for instance, it shows the variance in the 50th principal component of WM explained by the 24 MPs). Right panel (last two columns): Mean estimated variance explained in the regressors stated on the left of each row by an increasing number of WM or CSF regressors (for instance, it shows the variance explained on average in the 24 MPs by the first 50 principal components of WM). To examine the dependence of the curves on the degree of motion in each scan, two groups of scans were considered, referred to as low- and high-motion scans, corresponding to the lower and upper quartile of the distribution of mean *FD* values respectively. The blue and red curves correspond to the variance accounted for (VAF) averaged across low-motion and high-motion scans, respectively, whereas the shaded areas denote the standard error. For all four sources of noise, we observe that the first few PCA regressors demonstrated stronger association to the model-based regressors compared to components found later in the order, justifying the practice of using the most significant PCA components in aCompCor.

483 respect to decreasing tissue signal variance explained (see [Suppl. Fig. 1](#) for the variance explained in the WM and CSF
484 compartments by the corresponding WM and CSF regressors). In the left panel, it can be seen that the model-based
485 regressors explained larger fraction of variance in the first few WM and CSF regressors than in subsequent regressors.
486 Moreover, the high-motion scans demonstrated different trends compared to low-motion scans. For example, in the left
487 panel we can see that high-motion scans exhibited stronger association between the first PCA regressors and the 24 MPs,
488 while low-motion scans exhibited stronger association between the first PCA regressors and regressors related to cardiac
489 pulsatility. Looking at WM vs CSF regressors, we observed several slight differences such as that the first few WM
490 regressors explained better the 24 MPs compared to the CSF regressors, whereas the opposite was observed when looking
491 at the cardiac pulsatility. However, when considering a large number of regressors (e.g. 100) both WM and CSF
492 regressors explained a significant fraction of variance for all four sets of model-based regressors, with mean correlation
493 values above 0.5. This suggests that both WM and CSF regressors can account (to some extent) for BOLD fluctuations
494 due to head and breathing motion as well as cardiac pulsatility and SLFOs.

495 Different trends were observed between the nine QC metrics when varying the number of components ([Fig. 2, Suppl.](#)
496 [Fig. 2](#)). Similar to previous studies, the signal-related metric median intraclass correlation (*MICC*) yielded high scores in
497 the raw data whereas when preprocessing was performed, the *MICC* was decreasing as more WM or CSF regressors
498 were removed ([Fig. 2c](#); Birn et al., 2014; Parkes et al., 2018). This trend is possibly due to that noise in fMRI is
499 characterized by high subject specificity and, hence, removing the noise when using more aggressive pipelines leads to
500 reduction in subject specificity (Birn et al., 2014; Parkes et al., 2018). As the *MICC* metric did not seem to reflect the
501 preservation of signal in the data, we excluded it from the rest of the analysis.

502 [Fig. 3](#) shows the metric QC_{signal} which was defined as the mean Z-score of the two signal-related metrics, *FCC* and
503 *ICCC*, as well as the metric QC_{motion} , defined as the mean Z-score of the six motion-related metrics, *FD-FCC*,
504 *FDDVARS*, *FD-FDDVARS*, *FDFC_{median}*, *FDFC_{dist}* and *FD-MFC*. [Fig. 3](#) also shows the scores for the combined QC
505 metric CQC, defined as the average score between QC_{signal} and QC_{motion} . Note that due to their definition, QC_{signal}
506 reflects the enhancement of SNR in the data, whereas QC_{motion} reflects the reduction in motion artifacts and biases. Even
507 though WM and CSF denoising yielded similar performance in terms of mitigating motion effects, WM denoising
508 achieved a considerably higher SNR compared to CSF denoising ([Fig. 3](#)). Furthermore, including the GS to the nuisance
509 regressors significantly improved the scores for both QC_{signal} and QC_{motion} , particularly for low numbers of PCA
510 components. Due to these observations, the subsequent results and discussion are focused on the performance of WM
511 denoising, and, unless explicitly stated otherwise, it is assumed that the GS is also included in the set of regressors.

512 Overall, we observed that QC_{signal} was high for the sets of regressors WM_{GS}^{30} to WM_{GS}^{200} with a maximum score of 8.9
513 for WM_{GS}^{60} ([Fig. 3](#)). In contrast, QC_{motion} illustrated a sharp peak for the more aggressive set of regressors WM_{GS}^{200} and,
514 as a consequence, the optimal set of regressors according to CQC was the latter one (i.e., WM_{GS}^{200}). Note that the fMRI
515 scans considered in this study consisted of 1160 volumes, therefore the 200 WM regressors used in the preprocessing
516 correspond to ~17% of the total WM regressors. To allow generalization of our results to conventional datasets that
517 typically have a longer TR between 2-4 s, we repeated the analysis for the case of the Gordon atlas after downsampling
518 the fMRI data by a factor of four, resulting in an effective TR of 2.88 s. For this subset of fMRI data that consisted of
519 290 volumes per scan, the best improvement, as assessed with the summarized metric CQC, was observed with the set
520 of regressors WM_{GS}^{30} ([Suppl. Fig. 7](#)).

521 The analysis of optimizing aCompCor was repeated in the Seitzman and MIST parcel space and yielded similar trends
522 for a varying number of PCA regressors ([Suppl. Fig. 3-Suppl. Fig. 6](#)). Similar to the data in the Gordon space, the set
523 WM_{GS}^{200} was found to be the best choice for the data in the Seitzman atlas space, whereas the set WM_{GS}^{300} seemed to
524 perform slightly better for the data in the MIST atlas space. In the following analyses, for both three atlases, we
525 considered WM_{GS}^{200} when comparing the performance with other preprocessing strategies (e.g. scrubbing and low-pass
526 filtering).

Quality control metrics for the Gordon atlas

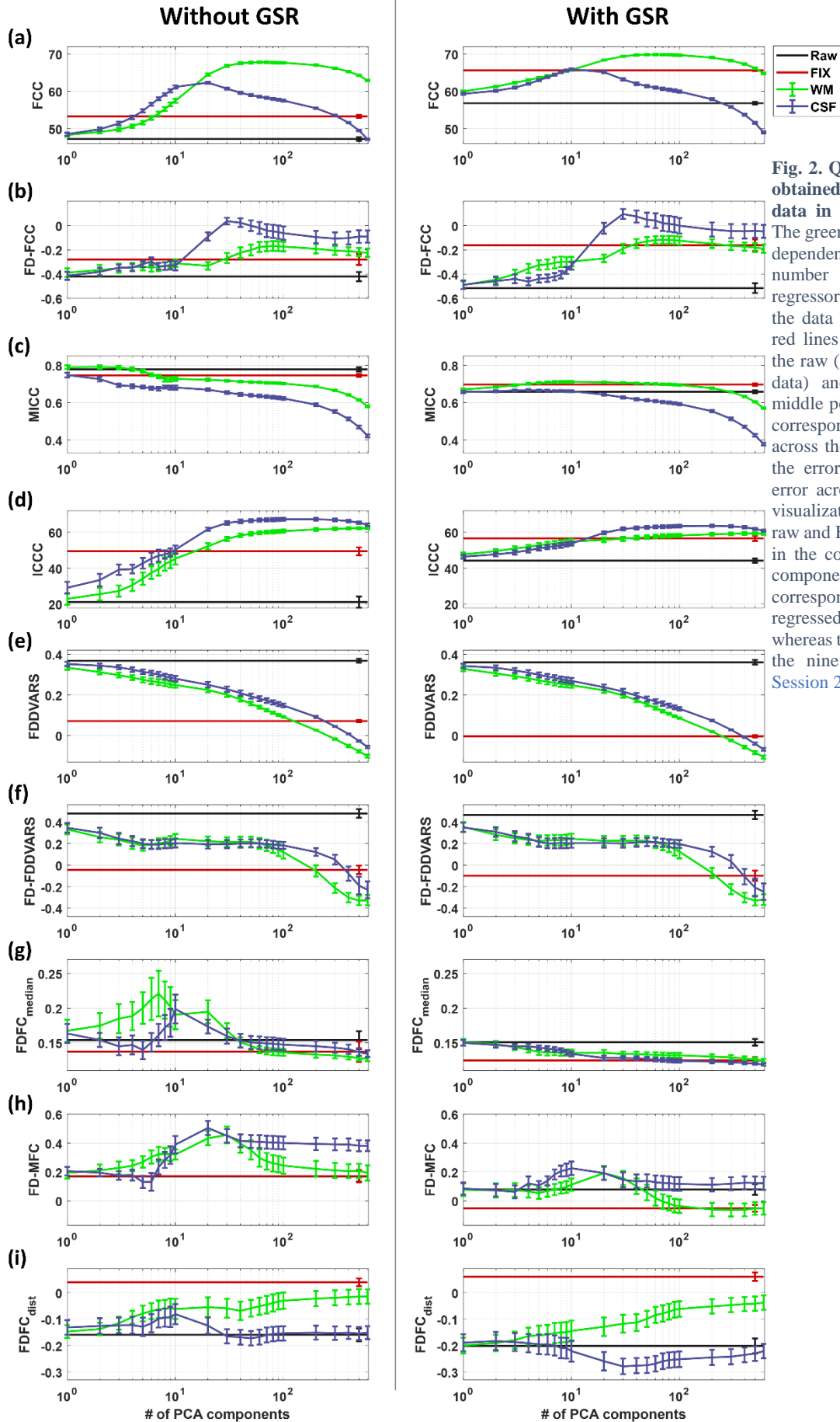


Fig. 2. Quality control (QC) scores obtained by aCompCor using the data in the Gordon parcel space. The green and purple curves show the dependence of the QC scores on the number of WM and CSF PCA regressors that were removed from the data respectively. The black and red lines indicate the QC scores for the raw (i.e., minimally-preprocessed data) and FIX-denoised data. The middle points in the curves and lines correspond to the QC scores averaged across the 10 groups of subjects and the error bars indicate the standard error across the 10 groups. To ease visualization, the error bars for the raw and FIX-denoised data are shown in the column corresponding to 500 components. The two columns correspond to the global signal being regressed out (right) or not (left) whereas the rows (a)-(i) correspond to the nine QC metrics described in [Session 2.6](#).

Summary of quality control (QC) metrics for the Gordon atlas

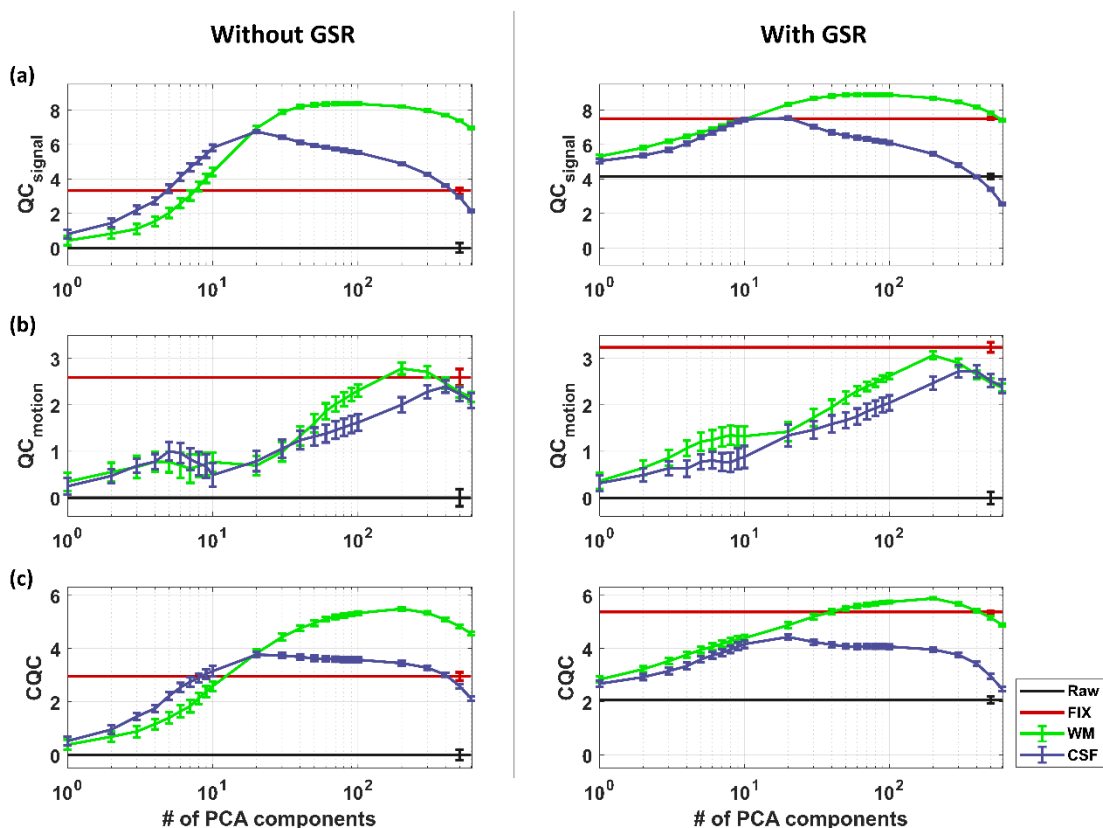


Fig. 3. Summarized quality control (QC) scores obtained by aCompCor using the data in the Gordon parcel space. The Z-scores of the two signal-related metrics FCC and $ICCC$, and six motor-related metrics $FD-FCC$, $FDDVARS$, $FD-FDDVARS$, $FDFC_{median}$, $FDFC_{dist}$ and $FD-MFC$ were averaged to yield the summarized scores QC_{signal} (a) and QC_{motion} (b), respectively. Subsequently, the two latter summarized scores were averaged to obtain the combined QC metric (CQC). We observe that about 50 to 100 PCA regressors from WM were needed in order to achieve high QC_{signal} scores, while 200 components from WM yielded the highest score in QC_{motion} . Including the GS in the set of regressors led to slightly higher scores for both summarized metrics. With respect to the CQC metric, the set of regressors WM_{GS}^{200} yielded the highest score (5.9) with the FIX_{GS} demonstrating the second highest score (5.4). While CSF denoising yielded comparable scores to WM denoising with respect to reduction of motion artifacts and biases (QC_{motion}), it also led to loss of signal of interest based on the low scores of QC_{signal} .

528

529 Signal-related QC metrics

530 Functional connectivity contrast (FCC)

531 The metric FCC proposed in this work for assessing the identifiability of large-scale networks exhibited unimodal curves
 532 for both WM and CSF, both with and without GSR (Fig. 2a). However, WM denoising achieved higher scores with a
 533 maximum score of 69.9 for WM_{GS}^{60} . Fig. 4 shows the FC matrix for the raw (minimally-preprocessed) data and for data
 534 that have been preprocessed with different pipelines for a scan that demonstrated considerable improvement in
 535 identifiability of the networks when regressing out the set WM_{GS}^{200} . It is evident that the raw data were very noisy,
 536 preventing the identification of the networks ($FCC=23.0$) but when denoising was performed with WM_{GS}^{200} , all 12
 537 networks were clearly identified ($FCC=69.4$). Interestingly, when GSR was applied without any other nuisance regressor
 538 or NCT to the raw data, it did not have a strong effect on the contrast but when it was applied after FIX denoising it led
 539 to a significant increase of FCC score from 40.1 to 65.4. Overall, GSR improved the FCC score for both FIX and WM
 540 denoising (Fig. 2a).

541 Fig. 5 shows the FC matrices averaged across all 1560 scans (group-level FC matrices) obtained from raw and four
 542 preprocessed fMRI datasets (i.e., data preprocessed with different pipelines). The FCC estimated from the group-level

FC matrix of subject S896778 (R1a) for different pipelines (Gordon atlas)

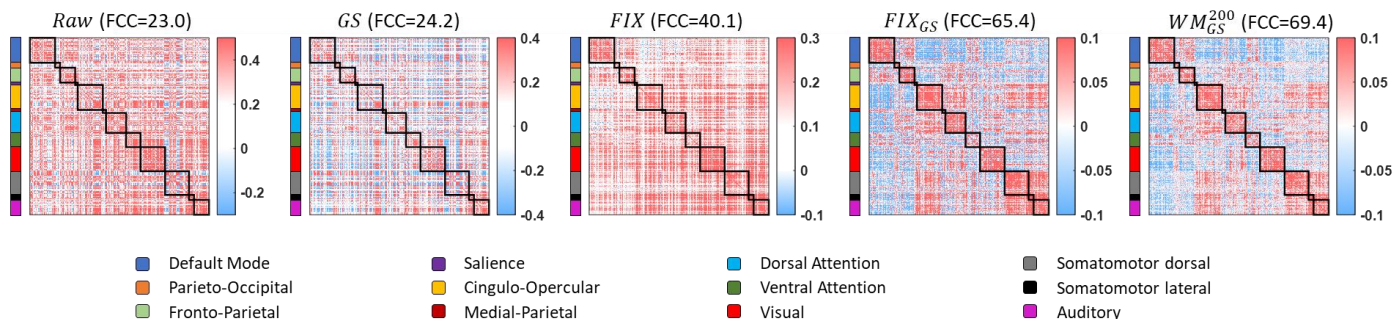


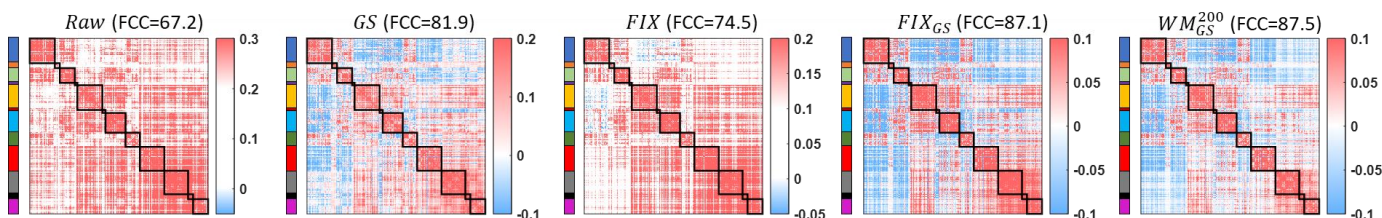
Fig. 4. FC matrix of subject S896778 (R1a) for different pipelines (Gordon atlas). While the networks could not be distinguished by visually inspecting the FC matrix of the raw data, they were easily identified after regressing out the set WM_{GS}^{200} or after FIX denoising, especially when FIX was combined with GSR. Similar conclusions were drawn based on the *FCC* metric, which quantifies the identifiability of the networks (reported on the top of each matrix).

543 FC matrices were substantially higher compared to the *FCC* estimated on a scan basis for the same pipelines (Fig. 2a).
 544 Note that for the raw data, the *FCC* score that was estimated first on a scan-basis and, then, averaged across all scans was
 545 47.3 (Fig. 2a), whereas the *FCC* score estimated from the group-level FC matrix (i.e. the FC matrix was first averaged
 546 across all scans) had a higher value of 67.2 (Fig. 5). In addition, the *FCC* score obtained from the group-level FC matrix
 547 (67.2) was at similar levels with the highest *FCC* score achieved on a scan-specific basis across all pipelines (i.e., when
 548 preprocessed with WM_{GS}^{200}).

549 **Intraclass correlation contrast (ICCC)**

550 The metric *ICCC* proposed in this work to assess subject specificity in the fMRI data, showed an increasingly monotonic
 551 behavior in the range of mild pipelines, for both WM and CSF (with and without GSR), reaching a plateau at about 30

FC matrix averaged across all scans for different pipelines (Gordon atlas)



ICC matrix considering all scans for different pipelines (Gordon atlas)

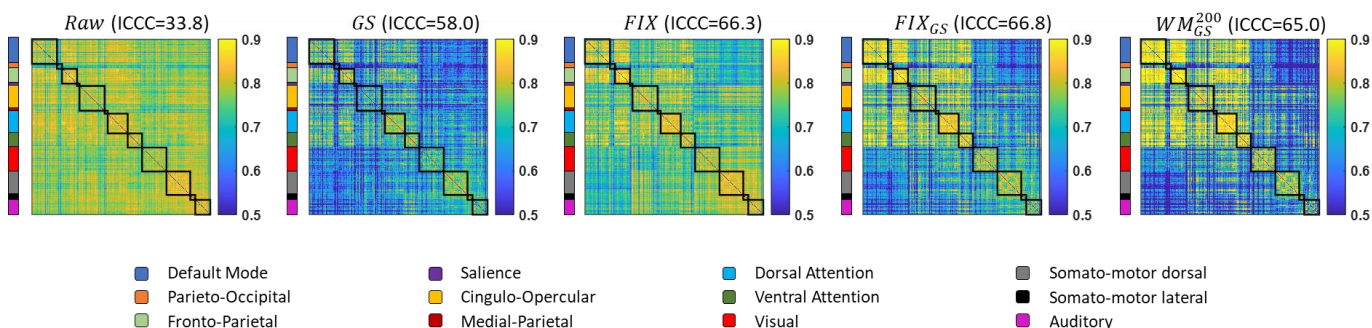


Fig. 5. FC (top) and ICC (bottom) matrices considering all scans for different pipelines obtained from the data in the Gordon parcel space. Averaging the FC matrices across all 1560 scans improved the identifiability of the networks considerably for both the raw and preprocessed data. As a consequence, the associated *FCC* scores reported on the top of each matrix were higher than the scores presented in Fig. 2a, which were obtained on a scan-specific basis and subsequently averaged within groups of 39 subjects. Similarly, the contrast estimated from the *ICCC* matrices (i.e., *ICCC*) when considering all 1560 scans was higher compared to the *ICCC* estimated from the smaller groups of 39 subjects each (Fig. 2d). Interestingly, we observe that a large number of BNEs, and especially edges between the default mode and fronto-parietal networks, exhibited low FC values but high *ICCC* values.

552 components, followed by a small decline for the most aggressive pipelines. However, as shown in [Suppl. Fig. 2 \(a & d\)](#),
553 *FCC* exhibited higher *Z*-scores compared to *ICCC* and, therefore, contributed the most to the scores in the signal-related
554 summarized metric QC_{signal} ([Fig. 3a](#)), which was defined as the average *Z*-score between *FCC* and *ICCC*.

555 [Fig. 5](#) shows the *ICC* matrices for the raw data and four preprocessed fMRI datasets estimated using all 1560 scans. It
556 can be seen that in the case of the raw data the *ICC* values were high for all edges, which resulted in a low *ICCC* score.
557 On the other hand, when an aggressive pipeline was used (e.g. WM_{GS}^{200}), the *ICC* values for most of the BNEs dropped
558 to significantly lower values compared to the rest of the edges leading to an increase in *ICCC* score. Nevertheless, even
559 with aggressive pipelines, many BNEs, and particularly edges corresponding to interactions between the default mode
560 and fronto-parietal networks, demonstrated high *ICC* scores even though the corresponding edges in the group-level FC
561 matrix exhibited low correlation values ([Fig. 5](#)). Similar results were observed for the Seitzman and MIST atlases ([Suppl.](#)
562 [Fig. 8-Suppl. Fig. 9](#)). In addition, note that the *ICCC* scores reported in [Fig. 5](#) were higher compared to the *ICCC* scores
563 extracted from the smaller groups of subjects shown in [Fig. 2d](#) (groups of 39 subjects each). Also, differences in *ICCC*
564 between pipelines found when scores were obtained for each group of subjects separately were decreased when *ICCC*
565 was obtained from all subjects in one step (e.g. differences in *ICCC* scores between *GS* and FIX_{GS}). The aforementioned
566 property of the metric *ICCC* suggests that its sensitivity in comparing the performance between preprocessing strategies
567 decreases when larger number of subjects is considered.

568

569 Motion-related QC metrics

570 *FD-FCC*

571 The raw data yielded a mean *FD-FCC* score of -0.42 implying that lower levels of motion were associated with higher
572 *FCC* scores ([Fig. 2b](#)). Importantly, when performing WM denoising with more than 30 components, the strength of *FD-*
573 *FCC* dropped to about -0.15 (*Z*-score 2.2). [Fig. 6](#) shows scatterplots of mean *FD* vs *FCC* for the first scan of 370 subjects
574 (20 subjects that demonstrated a mean *FD* three median absolute deviations (MADs) above the median were excluded).
575 We observe that even though GSR applied alone on the raw data improved the *FCC* score, it also increased the negative
576 correlation between mean *FD* and *FCC* or, in other words, it enhanced the dependence of *FCC* score on the levels of
577 motion ($r = -0.46$; $p = 10^{-19}$). However, when GSR was performed along with WM denoising of 200 regressors
578 (WM_{GS}^{200}) the negative correlation between *FD* and *FCC* almost vanished ($r = -0.11$; $p < 0.04$).

579 *FDDVARS*

580 The raw data demonstrated an *FDDVARS* score of 0.37, suggesting that the parcel time series were strongly contaminated
581 by motion artifacts ([Fig. 2e](#)). WM denoising with 200 components (WM_{GS}^{200}) was able to drop *FDDVARS* to 0.02,
582 corresponding to a *Z*-score of 11.3. [Suppl. Fig. 10-Suppl. Fig. 11](#) present traces of *FDDVARS* from individual scans,
583 where it can be appreciated that WM denoising led to a strong reduction of motion artifacts during time windows with
584 high levels of motion. Note that *FDDVARS* exhibited significantly higher *Z*-scores than the rest of the motion-related
585 QC metrics ([Suppl. Fig. 2e](#)) and, therefore, contributed the most to the scores of the summarized metric QC_{motion} ([Fig.](#)
586 [3](#)).

587 *FD-FDDVARS*

588 The raw data exhibited a mean correlation *FD-FDDVARS* of 0.48 ([Fig. 2f](#)), implying that higher levels of motion in a
589 scan resulted in significantly larger motion artifacts in the fMRI data. The set of regressors WM_{GS}^{200} achieved the smallest
590 absolute score of *FD-FDDVARS* (score: -0.07), corresponding to a *Z*-score of 2.7. [Fig. 6](#) shows scatterplots of the mean
591 *FD* vs the *FDDVARS* score (i.e., *FD-FDDVARS*) for the raw data and four different preprocessed datasets considering
592 the first scan from 370 subjects (20 subjects were excluded due to extreme values in mean *FD*). As we can see from the
593 raw data, the levels of motion during a scan (as evaluated with mean *FD*) had a strong effect on *FDDVARS*, which
594 reflects the degree of motion artifacts in the fMRI data ($r = 0.47$; $p < 10^{-21}$). The pipelines FIX_{GS} and WM_{GS}^{200} were

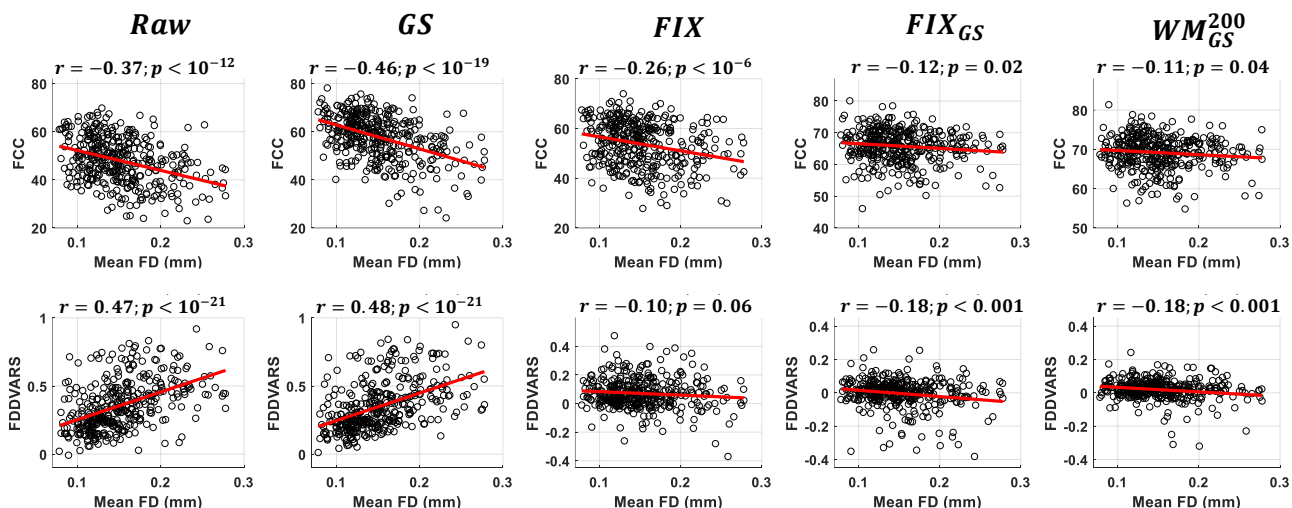


Fig. 6. Scatterplots of mean FD vs FCC (top) and mean FD vs FDDVARS (bottom) considering the first scan from all subjects*. In the case of raw data, higher levels of motion in a scan made network identification more difficult (lower FCC scores) and resulted in significantly larger motion artifacts in the fMRI data (higher FDDVARS values). Using the pipelines WM_{GS}^{200} and FIX , resulted in a significant reduction of the dependence of FCC and FDDVARS on the levels of motions. *Scans with mean FD three median absolute deviations (MADs) above the median were excluded (based on this criterion, 20 out of 390 subjects were excluded).

595 able to reduce the correlation of $FD-FDVARs$ to -0.18 ($p < 0.001$). We also observed that FIX achieved a lower
 596 correlation $FD-FDDVARs$ of -0.10 compared to FIX_{GS} and WM_{GS}^{200} . However, FIX exhibited also larger absolute scores
 597 of $FDDVARs$ than FIX_{GS} and WM_{GS}^{200} .

598 $FDFC_{median}$

599 When GS was included in the sets of regressors, the scores for $FDFC_{median}$ exhibited a monotonically decreasing trend
 600 for an increasing number of components, beginning at 0.15 for raw data (Z-score: 0.1) and reaching 0.13 (Z-score: 0.7)
 601 for both FIX_{GS} and WM_{GS}^{600} (Fig. 2g). However, when GS was not included in the preprocessing, increasing the number
 602 of WM components from 1 to 7 PCA regressors resulted in an increase for $FDFC_{median}$ from 0.15 to 0.22; for an even
 603 higher number of components, $FDFC_{median}$ decreased, reaching 0.13 in the case of WM_{GS}^{500} .

604 $FDFC_{dist}$

605 In the case of raw data, $FDFC_{dist}$ was equal to -0.16 , which reflects that short-distance pairwise correlations were more
 606 severely confounded by motion than long-distance correlations (Fig. 2i). Increasing the number of components in WM
 607 denoising resulted in a decrease in the correlation values, with the more aggressive sets WM^{600} and WM_{GS}^{600} achieving
 608 the minimum $FDFC_{dist}$ scores of -0.01 and -0.04 . However, the associated Z-scores for the latter two sets were relatively
 609 low (1.1 and 1.0; Suppl. Fig. 2i) and, as a consequence, $FDFC_{dist}$ did not have a significant weighting on the CQC
 610 metric.

611 $FD-MFC$

612 $FD-MFC$ was proposed in this work and is based on the assumption that the more a subject moves during a scan, the
 613 higher the mean value of correlations in the FC matrix is. As we can see in Fig. 2h, the score for $FD-MFC$ in the case of
 614 raw data was 0.22, confirming that motion can inflate the estimated correlations in the FC matrix. Importantly, when
 615 GSR was not performed, increasing the number of WM components from 1 to 30 led to an increase of $FD-MFC$, with
 616 WM^{30} exhibiting an $FD-MFC$ score of 0.45. For a higher number of WM components, $FD-MFC$ decreased
 617 monotonically reaching 0.19 for WM^{600} . Overall, when WM denoising was combined with GSR, a lower $FD-MFC$ was

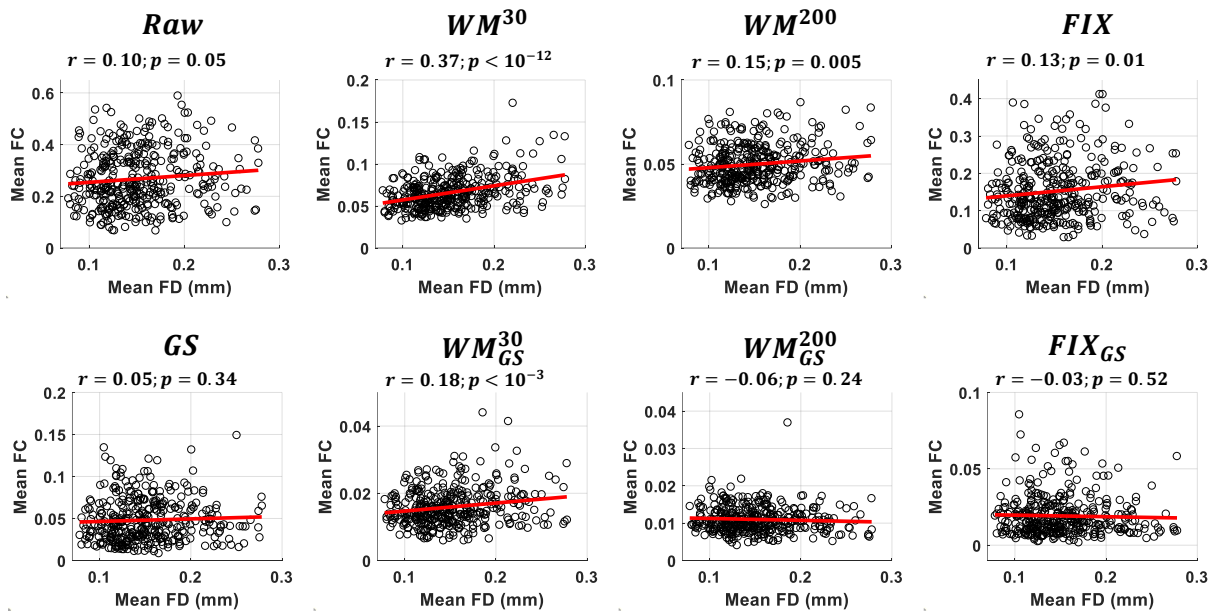


Fig. 7. Scatterplots of mean *FD* vs mean *FC* for different pipelines with (bottom) or without (top) GSR considering the first scan from all subjects*. In the case of raw data, scans with high levels of motion were associated to high correlation values in *FC*. This dependence on the levels of motion vanished when the data were preprocessed with WM_{GS}^{200} or FIX_{GS} . Importantly, when a relatively low number of components were removed (e.g., WM^{30}), the effect of motion was enhanced compared to the raw data. *Scans with mean *FD* three median absolute deviations (MADs) above the median were excluded (based on this criterion, 20 out of 390 subjects were excluded).

618 achieved, with WM_{GS}^{200} yielding a score of -0.06 (Z-score: 0.7). Similar results were found when *FD-MFC* was estimated
 619 using the first scan from all subjects, even though there was a mild decrease in the scores for all pipelines (Fig. 7).

620 3.2 Evaluation of data-driven NCTs

621 In this analysis, we used the QC metrics to compare twenty different pipelines involving the removal of data-driven
 622 nuisance regressors from the fMRI data (Table 1). Fig. 8 shows the scores for the summarized metrics QC_{signal} and
 623 QC_{motion} , as well as the combined metric CQC for the Gordon atlas (the results for the Seitzman and MIST atlas are
 624 shown in Suppl. Fig. 12-Suppl. Fig. 13). Looking at the first three pipelines that correspond to the 6, 12 and 24 MPs, we
 625 observe that motion regressors reduced the effect of motion and (to a less extent) improved the SNR in the data, with the
 626 more aggressive pipeline (24 MPs) exhibiting the strongest impact for all three atlases. GSR alone (pipeline 4)
 627 significantly improved the SNR even though, for the Seitzman and MIST atlas, it also led to a small decrease in the
 628 QC_{motion} score (Suppl. Fig. 12-Suppl. Fig. 13). As can be seen from Suppl. Fig. 3-Suppl. Fig. 4, $FD\text{-}FCC$ and $FD\text{-}MFC$
 629 increased after GSR, while $FDDVARS$ was at similar or lower levels compared to the raw data, suggesting that even

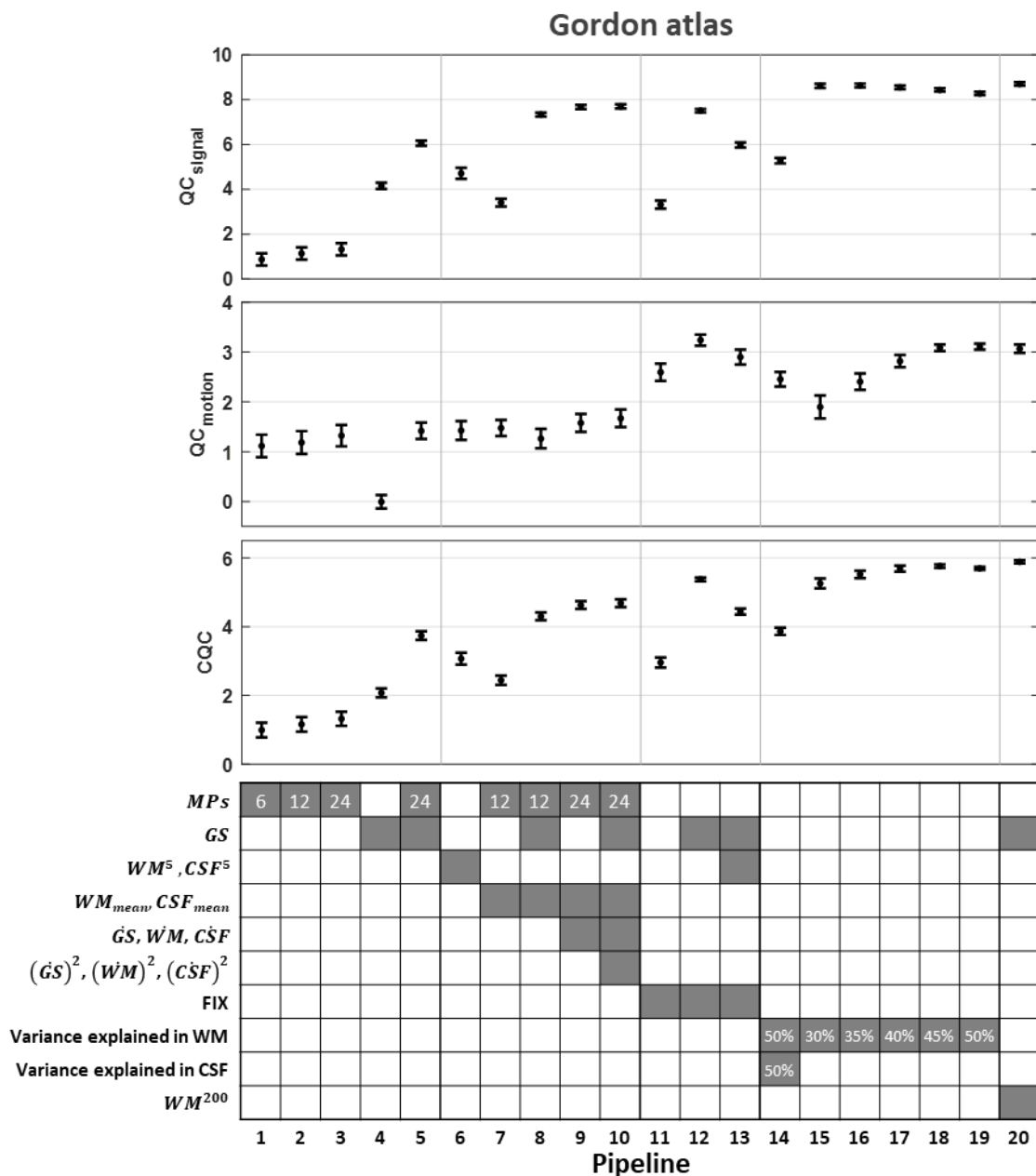


Fig. 8. Evaluation of data-driven NCTs (Gordon atlas). Twenty different data-driven pipelines were examined, as listed in Table 1. Among all pipelines, pipelines that included GSR and WM or FIX denoising yielded the highest scores in QC_{signal} , QC_{motion} and CQC (i.e., pipelines 12 and 17-20).

630 though there was not any enhancement of motion artifacts, the systematic differences across scans due to motion
631 increased.

632 Several studies employ aCompCor as NCT, removing five WM and five CSF regressors (Wang et al., 2017; Xiao et al.,
633 2016). Our results derived from the HCP data suggest that this set of regressors demonstrates a moderate improvement
634 with respect to both QC_{signal} and QC_{motion} (pipeline 6). Similar improvement in the quality of data was achieved when
635 the mean time series from WM and CSF, and the 12 MPs were regressed out (pipeline 7; Urchs et al., 2017) whereas
636 when including also the GS to the set of regressors, the QC_{signal} score reached a higher value (pipeline 8; Finn et al.,
637 2015). Pipelines 9 and 10 were more aggressive variants of pipeline 8, including 24 instead of 12 MPs, as well as the
638 derivatives and squared terms of the tissue mean time series from GM, WM and CSF (Ciric et al., 2017; Laumann et al.,
639 2017; Xia et al., 2018). Considering more nuisance regressors in the preprocessing (36 rather than 15 regressors), pipeline
640 10 exhibited a small but significant improvement compared to pipeline 8, with respect to QC_{signal} and QC_{motion} for the
641 Gordon and Seitzman atlases, whereas for the MIST atlas QC_{motion} increased and QC_{signal} slightly decreased.

642 Pipelines 11 to 13 evaluated the data quality for the FIX-denoised data provided in HCP with and without further
643 denoising (Fig. 8). We observe that, as proposed in Burgess et al. (2016), regressing out the GS from the FIX-denoised
644 data improved both QC_{signal} and QC_{motion} scores (pipelines 11 vs 12). However, when five WM and five CSF regressors
645 were removed in addition to the GS (pipeline 13; Siegel et al., 2017) both summarized metrics were lower compared to
646 performing only GSR (pipeline 12).

647 Pipeline 14 was based on the NCT recommended by Muschelli et al. (2014), which considers as set of regressors the
648 necessary number of WM and CSF regressors needed to explain 50% of variance in their associated compartments. As
649 we see, in all three atlases pipeline 14 achieved a satisfactory reduction in motion artifacts, even though the SNR was
650 much lower compared to other pipelines. Earlier results presented here showed that, the scores of the QC_{signal} metric
651 were relatively low when CSF denoising was performed and high for WM denoising, particularly when GSR was also
652 performed (Fig. 3). Based on these results, we also considered pipelines 15 to 19 that consider the GS as well as the WM
653 regressors needed to explain a predefined fraction of variance in WM ranging from 30 to 50%. Our results suggest that
654 pipelines 15 to 19 achieved high scores for both QC_{signal} and QC_{motion} , with the highest scores achieved when 45-50%
655 of the variance was used as a threshold to select the WM regressors.

656 Finally, the set of regressors WM_{GS}^{200} that was found in the previous section to perform the best was considered as pipeline
657 20. For all pipelines, we observed that the highest QC scores were obtained when GSR was performed in combination
658 with FIX or WM denoising (i.e., pipelines 12 and 17-20).

659

660 3.3 Evaluation of model-based (motion and physiological) NCTs

661 Four sets of model-based regressors were examined with respect to improvement in SNR and reduction of motion
 662 artifacts and biases. The four sets were related to head motion (24 MPs), cardiac pulsatility, breathing motion and SLFOs
 663 To assess their contribution when tissue-based regressors were also included in the set of nuisance regressors, we
 664 examined 64 pipelines presented in Fig. 9 in the form of a design matrix that refers to combinations of the four sets of
 665 model-based regressors, the GS and a set of 200 PCA regressors from WM. When only model-based regressors were
 666 considered, accounting for SLFOs improved the QC_{signal} score, whereas correcting for either head or breathing motion
 667 improved both QC_{signal} and QC_{motion} scores. Accounting for cardiac pulsatility led to an increase in QC_{signal} and
 668 decrease in QC_{motion} , even though the effect of cardiac regressors was lower compared to the rest of the model-based
 669 regressors. Finally, when GS and 200 WM regressors were considered (WM_{GS}^{200}), accounting also for breathing motion,
 670 cardiac pulsatility or SLFOs, using model-based regressors, did not have any impact on the data quality, whereas
 671 correcting for motion with the 24 MPs led to a small decrease in the score for QC_{motion} .

672

673

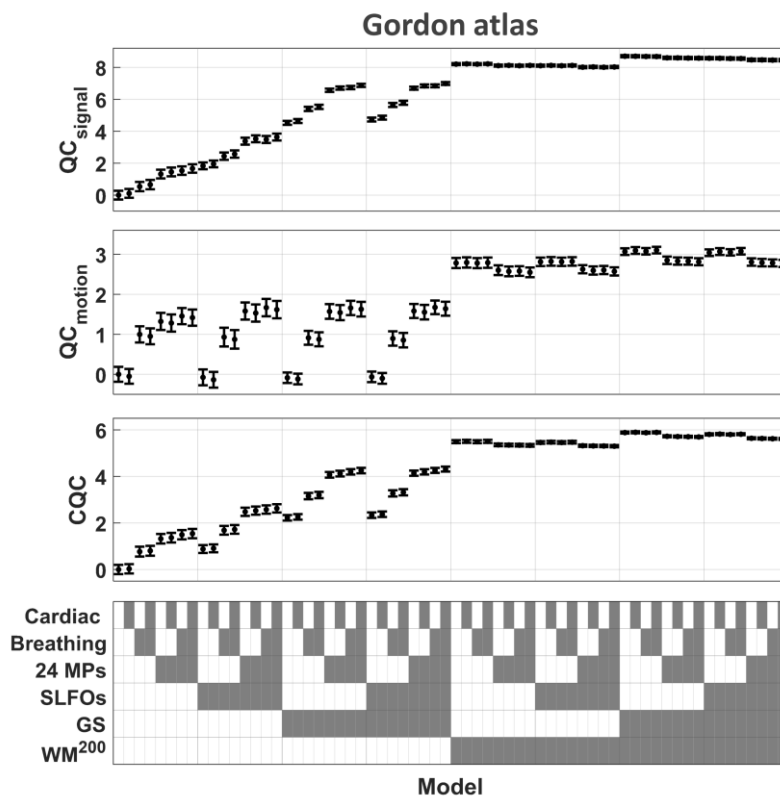


Fig. 9. Evaluation of model-based NCTs (Gordon parcel space). Model-based regressors were obtained from the motion (realignment) parameters and physiological recordings to correct for artifacts due to head motion (24 MPs), cardiac pulsatility (Cardiac), breathing motion (Breathing) and SLFOs (i.e., BOLD fluctuations due to changes in heart rate and respiratory flow; Kassinopoulos and Mitsis, 2019). Overall, none of the examined model-based NCTs contributed further to data quality improvement beyond that achieved with the set of tissue-based regressors WM_{GS}^{200} . Similar results were found using the data in the Seitzman and MIST parcel space (Suppl. Fig. 14).

674 3.4 Evaluation of scrubbing

675 Discarding volumes contaminated with motion artifacts before regressing out the set of nuisance regressors WM_{GS}^{200} did
 676 not provide any gain with respect to the fMRI data quality (Fig. 10). Instead, stricter threshold values FD_{thr} resulted in
 677 lower scores for QC_{signal} and QC_{motion} . Also, discarding volumes with $DVARS$ values beyond the threshold did not have
 678 any impact on the QC_{motion} score, while it significantly decreased QC_{signal} .

679

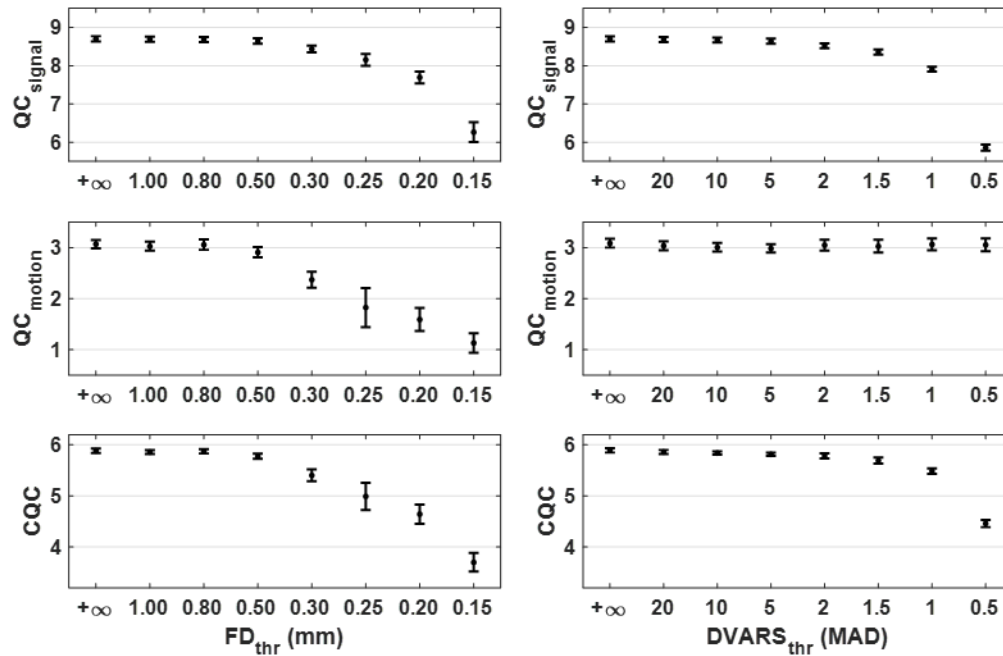


Fig. 10. Effect of scrubbing in data quality for different threshold values. The framewise data quality indices FD and $DVARS$ were used to flag volumes contaminated with motion artifacts. Subsequently, the motion-contaminated volumes were discarded before preprocessing the data with the set WM_{GS}^{200} and estimating the QC_{signal} , QC_{motion} and CQC scores. The obtained scores for varying values of thresholds FD_{thr} and $DVARS_{thr}$ are shown on the left and right columns, respectively. For both FD and $DVARS$ scrubbing, the lower (stricter) were the threshold values, the worse was the resulting data quality. Similar results were found using the data in the Seitzman and MIST parcel space (Suppl. Fig. 15). For the fraction of volumes retained after scrubbing at a given threshold please see Suppl. Fig. 18.

680 3.5 Evaluation of low-pass filtering

681 To examine the effect of low-pass filtering on data quality as well as its dependence on the cut-off frequency, we repeated
 682 the denoising of the data with variants of WM denoising (i.e. WM_{GS}^{20} , WM_{GS}^{50} , WM_{GS}^{100} and WM_{GS}^{200}) after low-pass
 683 filtering the data and the regressors at different cut-off frequencies. For all variants of WM denoising, the highest CQC
 684 scores were achieved when low-pass filtering was performed at 0.20 Hz (Fig. 11). At this cut-off frequency, the sets of
 685 regressors WM_{GS}^{50} and WM_{GS}^{100} outperformed the larger set WM_{GS}^{200} . In addition, we observed that the lower cut-off
 686 frequency 0.08 Hz that is commonly used in the literature, as well as the cut-off frequency 0.05 Hz, led to a decrease in
 687 the CQC score which was attributed to a reduction in QC_{signal} . The pipelines that consisted of a low-pass filtering at 0.20
 688 and removal of WM_{GS}^{50} or WM_{GS}^{100} were among the pipelines that achieved the highest CQC scores for the Seitzman and
 689 MIST atlas as well (Suppl. Fig. 19). Overall, we observed that mild variants of WM benefitted the most from low-pass
 690 filtering, particularly in terms of reducing motion artifacts and biases (Fig. 11, Suppl. Fig. 19).

691

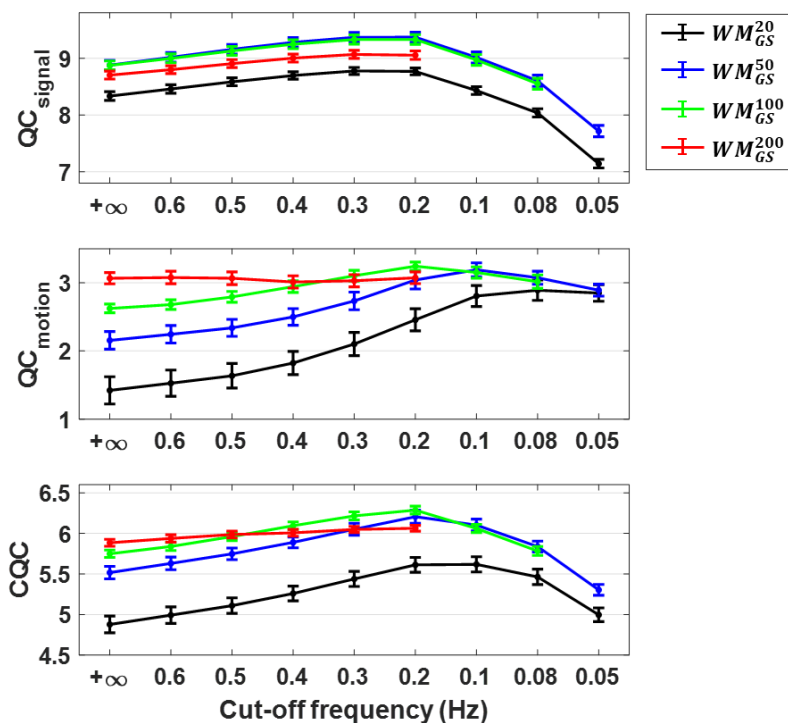


Fig. 11. Effect of low-pass filtering in data quality for different cut-off frequencies. For all variants of WM denoising examined, low-pass filtering with a cut-off frequency of 0.2 Hz yielded the highest CQC score. At this cut-off frequency, WM_{GS}^{50} and WM_{GS}^{100} yielded the highest CQC scores with mean scores 6.2 and 6.3, respectively. No significant difference was observed between WM_{GS}^{50} and WM_{GS}^{100} ($p > 0.05$, two-sample t -test). The cut-off frequency of 0.2 Hz, and particularly when combined with WM_{GS}^{50} and WM_{GS}^{100} , yielded the highest CQC score also for the data registered to the Seitzman and MIST atlases (Suppl. Fig. 19). Note that the lowest cut-off frequencies examined for WM_{GS}^{100} and WM_{GS}^{200} were 0.08 Hz and 0.2 Hz, as for these sets of regressors lower cut-off frequencies lead to fMRI data with a substantially low number of degrees of freedom (Bright et al. 2017). Data that had not been filtered are indicated with a ∞ cut-off frequency.

3.6 Identifiability of large-scale networks

Finally, we sought to quantify the identifiability of each of the large-scale networks defined in the three functional atlases employed here and its dependence on the preprocessing pipeline. To this end, we calculated the *FCC* score of each network for the raw dataset as well as four preprocessed datasets. To obtain the *FCC* score per network, for a given network, when estimating the *FCC* score, we compared WNEs with BNEs considering only WNEs that belonged to the examined network (for more information see [Section 2.6](#)).

In [Suppl. Fig. 20](#), we see that for the Gordon and Seitzman atlases, there was larger variability in *FCC* score across networks rather than across pipelines. Networks consisting of a small number of parcels, such as the salience network in the Gordon atlas and the medial temporal lobe network in Seitzman atlas, exhibited small negative *FCC* scores for the raw data, whereas when the data were preprocessed with a pipeline that included GSR the *FCC* scores were increased to small positive values. On the other hand, large networks such as the default mode network exhibited significantly higher *FCC* scores.

In the case of the MIST atlas there was less variability in *FCC* score across networks compared to the Gordon and Seitzman atlas, which may be due to the fact that these networks consisted of a similar number of parcels. However, two out of the seven networks demonstrated a somewhat unexpected behavior. Specifically, the mesolimbic network demonstrated a large negative *FCC* score for the raw and FIX-denoised data, despite the fact that it consists of a similar number of parcels to other networks in the atlas. Furthermore, regarding the cerebellum network, even though the *FCC* score in the raw data was relatively high, when FIX denoising was applied the *FCC* score dropped to zero.

Finally, while some networks in the three atlases were assigned the same name, they did not necessarily demonstrate the same behavior in terms of differences in *FCC* across the five fMRI datasets. For example, in the Gordon atlas we observe that the fronto-parietal network yielded the highest *FCC* score when the data were preprocessed using WM_{GS}^{200} , whereas in the MIST atlas, for the same network, the highest *FCC* score was observed with the raw data. Nevertheless, for the majority of networks, *FCC* scores were maximized when preprocessing was done with FIX_{GS} or WM_{GS}^{200} .

4. Discussion

In this study, we have rigorously examined the effects of different preprocessing steps on SNR and degree of motion artifacts and biases in resting-state fMRI data, focusing on functional networks. As in previous studies, the QC metrics used to compare preprocessing pipelines illustrated different trends between them (Fig. 2). Therefore, to facilitate the comparison across pipelines, we introduced a novel framework that initially normalizes each of the 8 QC metrics to Z-scores so that they reflect relative improvement in standard deviations with respect to the raw data. Subsequently, the two normalized signal-related metrics FCC and $ICCC$, and the six normalized motion-related metrics $FD-FCC$, $FDDVARS$, $FD-FDDVARS$, $FDFC_{\text{median}}$, $FDFC_{\text{dist}}$ and $FD-MFC$ are averaged to obtain the metrics QC_{signal} and QC_{motion} , respectively. Finally, the combined QC metric CQC defined as the mean of the QC_{signal} and QC_{motion} scores is calculated. Using this framework and resting-state fMRI data from the HCP registered to the Gordon atlas, we found that the largest improvement in the score of CQC was obtained when the GS and 200 PCA regressors from WM were regressed out (Fig. 3). Similar results were found when the fMRI data were registered to the Seitzman and MIST atlases (Suppl. Fig. 3-Suppl. Fig. 6). Note that 200 WM regressors correspond to about 17% of the regressors derived with PCA from WM as the fMRI scans consisted of 1160 volumes each, and explain on average $36\pm 6\%$ of the variance in the WM voxel time series (Suppl. Fig. 1).

Although we considered only subjects with good quality physiological data in all four scans, none of the model-based techniques examined here yielded further improvement in terms of data quality when compared to WM denoising (Fig. 9). Note that similar conclusions were derived from a subsequent study from our lab in which the effects of physiological processes on FC were more systematically examined (Xifra-Porxas et al., 2021). Specifically, in Xifra-Porxas et al. (2021), we provided evidence that data decomposition techniques (FIX and WM denoising) combined with GSR lead to a substantial mitigation of the effects of head motion and physiological fluctuations on FC but also improve connectome-based subject discriminability. In addition, when data decomposition techniques were considered, model-based preprocessing approaches did not provide any additional benefit. These observations may not be surprising as it has been previously shown that artifacts due to head motion and physiological fluctuations can be corrected by removing WM and CSF regressors (aCompCor) as well (Behzadi et al., 2007; Muschelli et al., 2014). Also, WM denoising, and in general model-free approaches such as FIX (Salimi-Khorshidi et al., 2014) and AROMA (Pruim et al., 2015b), have the benefit that they do not require physiological data and are not based on any assumptions related to the mechanisms by which physiological processes affect the BOLD signal. For example, the convolution models used here to account for the effect of heart rate and breathing pattern assume that a linear stationary system can describe these effects, which may not be entirely true (Kassinopoulos and Mitsis, 2019).

Even though the model-based techniques were not found to yield any additional improvement as compared to data decomposition techniques, it is important to bear in mind that the QC metrics considered in the present study are mainly intended for whole-brain FC studies and, thus, are not necessarily informative or even applicable in different contexts. Model-based techniques are of great importance in several cases, such as studies with limited field-of-view (e.g. laminar fMRI, brainstem imaging) where data-driven techniques (e.g. FIX denoising) cannot be directly used. Furthermore, model-based techniques are useful in studies of the autonomic nervous system (Kassinopoulos et al., 2021; Mulcahy et al., 2019) and task-based studies whereby physiological noise is often correlated to the signal of interest (Glasser et al., 2018) and, therefore, conservative approaches based on concurrent physiological recordings and physiologically-inspired models are needed to account for the associated noise, while also preserving the signal of interest.

Performing scrubbing before WM denoising (WM_{GS}^{200}) was found to deteriorate the quality of the data rather than improving it (Fig. 10). As this result contradicts with the benefits of scrubbing reported in the literature (Ciric et al., 2017; Gratton et al., 2020; Parkes et al., 2018; Power et al., 2015), we repeated the analysis using standard aCompCor, which removes a significantly smaller number of regressors (i.e. five WM and five CSF regressors), and found that scrubbing at specific threshold values ($FD > 0.20$ mm and $DVARS > 1.5$ MAD) improved the data quality with respect to motion-related QC metrics and, to a smaller extent, signal-related metrics (Suppl. Fig. 16). However, our findings

765 suggest that the improvement in data quality observed with mild preprocessing and scrubbing was still inferior to that
766 obtained with more aggressive pipelines (e.g. WM denoising and FIX) that are not preceded by scrubbing.

767 Recent studies have suggested that in multi-band fMRI datasets with short TR, such as the HCP dataset, the effect of
768 breathing activity on *FD* traces should be suppressed to ease the identification of motion-contaminated volumes and
769 avoid removing presumably noise-free volumes (Gratton et al., 2020; Power et al., 2019). With this in mind, we removed
770 the effects of breathing from the six motion realignment parameters using concurrent breathing recordings and 3rd order
771 RETROICOR, and estimated *FD* traces free of breathing effects. Consistent with previous studies (Gratton et al., 2020;
772 Power et al., 2019), these *FD* traces were characterized by lower amplitude and smaller oscillatory fluctuations and
773 yielded in turn lower numbers of motion-contaminated volumes for a given threshold value (Suppl. Fig. 18). However,
774 when the data were preprocessed using WM_{GS}^{200} , even with the proposed *FD* traces, scrubbing was found to deteriorate
775 the quality of the data (Suppl. Fig. 17). Note that, for the motion-related metrics examined in this study that are based on
776 *FD*, we considered the standard *FD* traces, which include breathing-related fluctuations. Breathing, apart from shifting
777 the acquired images due to disturbances in the magnetic field, can also alter the intensity in fMRI voxel time series (Raj
778 et al., 2001, 2000), and these alterations are not corrected via volume realignment. Therefore, the standard *FD* traces
779 were used in the QC metrics to render them sensitive to the presence of breathing-induced artifacts.

780 Finally, we found that low-pass filtering at 0.2 Hz led to further improvement in data quality beyond the improvement
781 achieved with WM denoising and, importantly, this improvement was more prominent for mild variants of WM denoising
782 (i.e. WM_{GS}^{50} and WM_{GS}^{100} ; Fig. 11). However, a substantial decrease in SNR was observed when the 0.08 Hz cut-off
783 frequency commonly used in fMRI studies was considered. The rationale behind choosing the 0.08 Hz cut-off frequency
784 for low-pass filtering in resting-state FC is that well-established large-scale networks have been found to oscillate at
785 frequencies below 0.10 Hz (Damoiseaux et al., 2006), while breathing motion and other sources of noise appear at
786 frequencies above this frequency (Caballero-Gaudes and Reynolds, 2017; Liu, 2016). Nevertheless, several studies have
787 found activity in RSNs in the range from 0.1 to 0.5 Hz (Chen and Glover, 2015; Niazy et al., 2011), suggesting that low-
788 pass filtering at 0.08 Hz may potentially remove signal of interest. Based on our results, when considering whole-brain
789 FC, low-pass filtering at 0.2 Hz yields the highest SNR, which may be related to reduction in breathing motion artifacts
790 that appear at around 0.3 Hz and may not be fully corrected with WM denoising.

791

792 **4.1 QC metrics**

793 Nine QC metrics were initially considered with three metrics related to the SNR in the fMRI data and six metrics related
794 to motion artifacts and biases. To assess the sensitivity of each metric, the subjects were split into 10 groups of 39 subjects
795 each with similar levels of motion across groups, as assessed with within-scan mean *FD*. Subsequently, the QC scores
796 were estimated for each group separately. Based on the fact that the 10 groups of subjects were characterized by similar
797 distributions of mean *FD* values, we hypothesized that more sensitive QC metrics would be associated with a lower
798 variability (or standard deviation) of scores across groups. Furthermore, to obtain QC metric values that are easier to
799 interpret and compare, the score for a given metric and group of subjects was expressed as a Z-score, which reflects the
800 improvement in standard deviations compared to the distribution of values found in the raw data across the ten groups
801 of subjects (for more information see Section 2.7).

802 To keep the computational load of the present study feasible, we considered three different functional atlases based upon
803 hard non-overlapping parcellations, which do not account for cross-subject variations in the parcel locations (Seitzman
804 atlas) and boundaries (Gordon and MIST atlas), and may therefore provide incomplete descriptions of the brain functional
805 organization (Pervaiz et al., 2020; Van Essen and Glasser, 2018). However, the QC metrics can be easily extended to
806 data-driven soft parcellations as well (e.g. spatial ICA), provided that the main functional connections expected to be
807 observed at the group level, as well as their strength, are known.

808 Signal-related metrics

809 Among the three signal-related metrics (i.e., metrics related to the SNR), *FCC* demonstrated a substantially higher
810 improvement in *Z*-score compared to the other two metrics (Suppl. Fig. 2), and as such was the main determinant of the
811 summarized metric QC_{signal} . The *FCC* is based on the assumption that the strength of correlation for WNEs in FC is on
812 average larger than BNEs. Previous studies have used similar metrics to assess spatial specificity in FC considering
813 though only interactions between specific regions in the brain rather than whole-brain interactions (Birn et al., 2014;
814 Chai et al., 2012; Muschelli et al., 2014), whereas Shirer et al. (2015) used a metric that compares the correlations of
815 WNEs with correlations between brain regions and regions outside the brain. While we acknowledge that some of the
816 BNEs may correspond to neuronal-related connections, these edges would likely be the minority. In addition, the relative
817 magnitude of within- vs -between- network edges allows the identification of clusters or networks. Therefore, we believe
818 that considering all BNEs to form the null distribution, rather than connections with voxels outside the brain, is more
819 appropriate.

820 *FCC* can be considered as a measure of segregation, similar to the modularity index adopted in graph theory approaches
821 for assessing the degree to which a network topology can be subdivided into distinct nonoverlapping communities
822 (Rubinov and Sporns, 2010). Note that our results were consistent with an earlier study that used the modularity index
823 as a signal-related QC metric for the evaluation of preprocessing strategies (Ciric et al., 2017). For instance, in the present
824 study, preprocessing approaches based on decomposition techniques (WM and FIX denoising) were characterized by
825 high *FCC* scores, which is in agreement with the high modularity index reported for the ICA-based technique AROMA
826 (Pruim et al., 2015b) and aCompCor in Ciric et al. (2017). However, a main difference between *FCC* and the modularity
827 index (Ciric et al., 2017; Cisler, 2017) is that *FCC* is based on *a-priori* information about the large-scale network
828 (community) to which each parcel belongs, whereas the modularity index assigns the parcels to communities for each
829 subject separately, a step that, depending on the algorithm employed, can be computationally demanding (Rubinov and
830 Sporns, 2010).

831 The signal-related metric *MICC* was used to assess test-retest reliability across the four sessions of each subject in whole-
832 brain FC estimates. However, as in previous studies, more aggressive pipelines were associated with lower *MICC* scores,
833 which has been interpreted as this metric reflecting subject-specificity due to presence of noise rather than signal of
834 interest (Fig. 2, Birn et al., 2014; Parkes et al., 2018). As *MICC* scores did not seem to correspond to SNR, it was excluded
835 from the rest of the analysis. Interestingly, Birn et al. (2014) reported smaller decreases in ICC for significant connections
836 compared to the remaining connections, which was also confirmed in our data (see for example Fig. 5). Therefore, in the
837 present work, based on these findings, we proposed a novel metric termed *ICCC*, which reflects the extent to which *ICC*
838 values in WNEs are higher as compared to BNEs. *ICCC* was found to behave in a similar manner with *FCC* and, thus,
839 later in the analysis it was combined with the *FCC* score to obtain the summarized metric QC_{signal} .

840 Note that the metrics *FCC* and *ICCC* assume that each parcel belongs to only one large-scale network and that only
841 parcels from the same network interact with each other, which is an oversimplified description of the brain functional
842 organization and can be potentially misleading, as numerous resting-state fMRI studies have documented interactions
843 between networks. For instance, in healthy controls, a positive intrinsic functional connection has been reported between
844 the amygdala and medial prefrontal cortex, which consist of key nodes of the limbic and default mode network,
845 respectively (Roy et al., 2009). In our work, pipelines that yielded some of the highest *FCC* and *ICCC* scores, such as
846 WM and FIX denoising along with GSR, were also characterised by strong functional connections and connections with
847 high subject-specificity for a large fraction of BNEs (Fig. 5 & Suppl. Fig. 13). Therefore, the use of *FCC* and *ICCC* did
848 not seem to suppress connectivity between brain regions of different networks. Nevertheless, to address the potential
849 limitations of *FCC* and *ICCC*, we would need to incorporate information in QC metrics about both within- and between-
850 network interactions associated with the population examined. However, this is challenging as the literature currently
851 lacks a detailed characterization of the brain functional organization at this level of detail.

852 Intriguingly, when the data were preprocessed with FIX_{GS} or WM_{GS}^{200} , edges corresponding to interactions between the
853 default mode and fronto-parietal networks, despite the low correlation values in group-level FC, demonstrated
854 significantly higher *ICC* values compared to other BNEs (Fig. 5). This finding suggests that regions in the default mode

855 and fronto-parietal networks may be functionally connected but in a subject-specific manner. On a side note, the values
856 of connectivity strength between regions in the aforementioned two networks were found in recent studies to contribute
857 to the identification of individuals using fMRI FC (Finn et al., 2015) as well as to the prediction of behavioral measures
858 (Smith et al., 2015).

859 A caveat of using *ICCC* as a metric to compare pipelines is that it requires a dataset with several subjects and more than
860 one scan per subject. As a result, in contrast to *FCC*, it cannot be used to assess the data quality for a specific scan. In
861 addition, looking at Fig. 2 & Fig. 5, we see that *ICCC* was increased both with a better preprocessing strategy or with a
862 larger sample size. In addition, when *ICCC* was estimated from all 390 subjects in one step rather than in groups of 39
863 subjects, apart from the increase in *ICCC* scores for all pipelines, we also observed smaller differences between pipelines
864 which can be translated as a lower sensitivity of *ICCC* when comparing pipelines. We found the dependence of the metric
865 *ICCC* on sample size somewhat puzzling. Due to the aforementioned dependence of *ICCC* sensitivity on the sample size,
866 for future studies with large sample sizes interested in assessing the performance of pipelines, we would recommend
867 estimating *ICCC* in small groups of subjects as done here.

868 Motion-related metrics

869 Head motion during the scan is a major confound in fMRI FC studies as it diminishes the signal of interest in the data
870 but also affects the strength of connectivity across regions and across populations in a systematic manner. While the
871 majority of edges in FC are typically inflated by motion, short-distance edges tend to be inflated even more than long-
872 distance edges (Satterthwaite et al., 2013). In addition, different populations often exhibit different tendency for motion
873 (e.g., young vs older participants), which has been shown to lead to artificial differences in FC (Power et al., 2015). To
874 assess the performance of each preprocessing strategy examined here on the aforementioned aspects of motion effects,
875 three previously proposed metrics (i.e., *FDDVARS*, *FDFC_{median}* and *FDFC_{dist}*) as well as three novel metrics (i.e., *FD-
876 FCC*, *FD-FDDVARS* and *FD-MFC*) were considered in the present study. While the main trend in all motion-related
877 metrics was that removing more WM regressors resulted in bringing the scores closer to zero, a different pipeline was
878 favored by each metric (Fig. 2). For example, in the case of WM denoising with GSR, the metric *FD-FCC* demonstrated
879 the smallest absolute score when 70 WM regressors were removed, whereas the metric *FDFC_{median}* yielded the smallest
880 absolute score for the most aggressive pipeline examined here (600 WM regressors). However, after normalizing the
881 metrics to Z-scores, *FDDVARS* was found to be considerably more sensitive than the remaining metrics (Suppl. Fig. 2)
882 and, thus, was the main determinant of QC_{motion} . As a result, the summarized metric QC_{motion} , despite being defined as
883 the average of all six motion-related metrics, favored the set WM_{GS}^{200} that was characterized by a high Z-score of
884 *FDDVARS*.

885 Combined QC metric

886 While the summarized metric associated to SNR QC_{signal} reached a maximum score for a broad range of pipelines
887 (WM_{GS}^{60} to WM_{GS}^{200}), to ensure an efficient mitigation of motion artifacts and biases, the combined QC metric favored the
888 more aggressive option of WM denoising (i.e., WM_{GS}^{200} ; Fig. 3). Due to the lack of ground truth in resting-state fMRI,
889 we cannot be certain that the combined QC metric is successful in identifying the best preprocessing pipeline. However,
890 it is reassuring that the combined QC metric favors data decomposition techniques combined with GSR as these
891 preprocessing techniques have been shown to improve subject discriminability of functional connectomes the most
892 (Xifra-Porxas et al., 2021). In addition, we find reassuring that the combined QC metric favors the inclusion of GSR in
893 the preprocessing, as GSR has been shown to strengthen the association of functional connectomes with behavioral
894 measurements (Li et al., 2019).

895 We acknowledge that depending on the fMRI study, the researchers may prefer, rather than using the combined QC
896 metric as it is, to give more weighting to the metric QC_{signal} and, thus, apply a milder WM denoising, particularly when
897 two populations with similar levels of motion are compared. In addition, we observe that for the majority of analyses,
898 *FCC* and *FDDVARS* favor similar pipelines with the summarized metrics QC_{signal} and QC_{motion} (e.g. Suppl. Fig. 3 &
899 Suppl. Fig. 5). For example, in the search of the variant of WM denoising and low-pass filter that maximize the SNR,

we observe that *FCC* favors the cut-off frequency 0.2 Hz with the set of regressors WM_{GS}^{50} (Suppl. Fig. 22; Gordon and Seitzman atlas), and this finding is consistent with the indications based on the summarized metric QC_{signal} (Fig. 9; Suppl. Fig. 19). Similarly, in the search of the pipeline that mitigates the effects of motion the most, *FDDVARS* is in favor of the cut-off frequency 0.2 Hz with the set of regressors WM_{GS}^{100} (Suppl. Fig. 22; Gordon and Seitzman atlas), which is also consistent with the indications based on the summarized metric QC_{motion} (Fig. 9; Suppl. Fig. 19). Therefore, considering that *FCC* and *FDDVARS* demonstrate significantly higher sensitivity than the rest of the metrics (Suppl. Fig. 2), it would be sensible for a study to determine the preprocessing strategy based solely on these two metrics. If the levels of motion in a cohort are relatively low, the mild pipeline proposed by *FCC* could be employed, whereas in the case that the levels of motion are high, a more aggressive pipeline towards the indications of *FDDVARS* would be more appropriate.

4.2 PCA-based WM denoising improves SNR and mitigates motion effects

In the original study introducing the aCompCor technique (Behzadi et al. 2007), the authors proposed the removal of 6 PCA regressors from WM and CSF to account for cardiac and breathing artifacts. However, this proposal was based on Monte Carlo simulations using a modified version of the “broken stick” method described in Jackson (2016), which does not take into account QC metrics that reflect in some way improvement in the quality of the fMRI data. A few years later, Chai et al., (2012) also proposed the removal of five PCA regressors from each noise ROI based on observations related to the connectivity between a region in the medial prefrontal cortex with other brain regions. They also showed that regressing out higher number of PCA regressors led to reduced correlation strengths, which may be associated to reduction of degrees of freedom in the data. Very likely based on these findings, many subsequent fMRI studies considered only 5 PCA regressors from each noise ROI (Circic et al., 2017; Wang et al., 2017; Xiao et al., 2016).

In this study, we sought to examine the effect of varying the number of PCA regressors on data quality based on QC metrics that account for the effect of motion, as well as the SNR in whole-brain FC rather than interactions between specific regions. Moreover, as there is evidence that neuronal-related activation can be detected in WM (Grajauskas et al., 2019), we examined separately the effects of WM and CSF denoising to determine whether CSF denoising could be sufficient for preprocessing. Interestingly, our results showed that even though WM and CSF denoising achieved similar reduction with respect motion artifacts and biases, the former exhibited substantially better performance in terms of SNR improvement compared to the latter (Fig. 2-Fig. 3). Particularly, the set of regressors WM_{GS}^{200} , which consists of 200 PCA regressors from WM and the GS illustrated one of the best overall performance among all sets of nuisance regressors examined here (Fig. 8). In addition, our results suggested that a small, albeit significant, further improvement can be achieved when combining mild variants of WM denoising (e.g. WM_{GS}^{50}) with low-pass filtering at 0.2 Hz.

The standard aCompCor technique that employs 5 PCA regressors from each noise ROI was found to increase the summarized metrics QC_{signal} and QC_{motion} compared to the raw data but not as much as the set WM_{GS}^{200} (pipeline 6 vs 20 in Fig. 8). However, we observed that, when GSR was not considered, removing a low number of WM or CSF regressors yielded more negative scores in $FDFC_{\text{median}}$ and $FD-MFC$ compared to the raw data, suggesting that the biases in FC due to differences in motion across scans were enhanced (Fig. 2). While this may seem counterintuitive, a possible explanation, based on Fig. 7, is that in raw data high-motion scans are associated with a larger inflation in connectivity due to motion artifacts as compared to low-motion scans. Even though the first few PCA regressors may correct for this inflation, this correction is more effective for low-motion scans which in turn increases the differences in inflation between low- and high-motion scans even more. This phenomenon was not observed for $FDFC_{\text{median}}$ when GSR was considered and it was diminished for $FD-MFC$, suggesting that the inflation in connectivity may be associated to motion-related fluctuations that are also reflected on the GS.

While the practice of regressing out from the data 200 WM regressors may raise concerns with regards to loss of signal of interest, it is important to bear in mind that the examined fMRI data lasted about 15 minutes and had a repetition time TR of 0.72. Therefore, each of the scans examined here corresponded to the relatively large number of 1200 volumes

945 and the voxel time series in WM and CSF were decomposed into 1200 PCA components (note that the first 40 volumes
946 were subsequently discarded to allow modelling of the SLFOs; for more information see [Section 2.4](#)). Note also that
947 during the training phase of FIX conducted by the HCP group, the average number of components estimated by ICA was
948 229 and from these components, on average 205 components were labelled as noisy (Smith et al., 2013a) which is overall
949 in agreement with the optimal number of WM components reported in the present study (200). Nevertheless, to examine
950 the dependence of the optimal number of regressors on the TR, we repeated the aCompCor analysis for a downsampled
951 version of the dataset that was generated by retaining every 4th functional volume of each scan, resulting this way to an
952 effective TR of 2.88 s. Doing so, we found that for this subset of data that is more similar to a conventional fMRI dataset
953 than the original dataset, the best improvement in data quality was achieved with 30 WM regressors combined with GSR
954 (i.e. WM_{GS}^{30} ; [Suppl. Fig. 7](#)). This result suggests that for data consisting of fewer timepoints a lower number of PCA
955 regressors would likely yield the best performance and vice versa.

956 An alternative preprocessing strategy proposed by Muschelli et al. (2014) is to use the number of PCA regressors needed
957 to explain 50% variance in the two noise ROIs. To compare the performance of this strategy, referred to as aCompCor50,
958 with the original aCompCor they used the QC metric FDDVARS as well as two metrics similar to the *FD-FDDVARS*
959 and *FCC* used here. Based on their results, aCompCor50, as compared to aCompCor, exhibited a larger reduction in
960 motion artifacts and improvement in FC specificity, even though the difference for the latter was only marginal when
961 corrected for multiple comparisons. In our dataset, aCompCor50, which corresponded to about 360 (± 60) WM and 90
962 (± 40) CSF regressors ([Suppl. Fig. 1](#)), also performed better compared to aCompCor (pipelines 14 vs 6 in [Fig. 8](#)). In the
963 present study, however, we also examined variants of aCompCor50 that consisted of GSR and WM denoising with
964 different thresholds of variance for choosing the optimal number of regressors (pipelines 15-19). In the case of the Gordon
965 and Seitzman atlas, GSR combined with WM regressors needed to explain about 45% variance performed almost as well
966 as WM_{GS}^{200} , whereas for the MIST atlas, GSR with WM regressors needed to explain 50% variance performed slightly
967 better than WM_{GS}^{200} ([Fig. 8](#)). It should be noted that, in the case that the number of WM regressors was determined based
968 on the variance accounted for, the exact number of regressors, and equivalently the loss of degrees of freedom from the
969 data, varied across participants. However, despite the varying number of degrees of freedom in the data, this approach
970 performed, overall, as well as WM_{GS}^{200} , both in terms of enhancement of SNR and mitigation of motion artifacts and
971 biases. Based on these observations, we believe that it will be important for future studies to examine more systematically
972 whether choosing the number of regressors based on a specific percentage of variance accounted for can lead to improved
973 data quality for a variety of fMRI datasets that may differ in terms of pulse sequence (single-band vs multi-band fMRI,
974 scan duration, main magnetic field, etc.) or population examined.

975 Another potential means of improving the performance of aCompCor is by defining the WM and CSF masks in a way
976 that partial volume effects are minimized, such as by restricting the CSF mask to the lateral ventricles or by applying
977 erosion along the boundaries, as was done in previous studies (Behzadi et al., 2007; Muschelli et al., 2014). It should be
978 noted that in the present study, the probability thresholds for defining the WM and CSF compartments (0.80 and 0.90,
979 respectively) were determined based on visual inspection. However, based on a secondary analysis, the performance of
980 CSF denoising can be improved if a stricter probability threshold is considered, albeit it still cannot outperform WM
981 denoising ([Suppl. Fig. 21](#)). Given this finding, we believe that future work should also examine the role of the probability
982 threshold for defining the WM and CSF masks in the context of denoising, as well as whether the optimal threshold
983 depends on factors such as the spatial resolution of fMRI data and the software used for tissue segmentation.

984 985 **4.3 GSR combined with WM or FIX denoising further improves SNR and mitigates motion effects**

986 The GS, which is defined as the average fMRI time series across all voxels in the brain or GM, is often regressed out
987 from the data. In our study, GSR improved the scores for the signal-related QC metrics and, to a less extent, the scores
988 for the motion-related QC metrics for both WM and FIX denoising ([Fig. 2-Fig. 3](#)). For a low number of PCA regressors
989 in WM denoising, we observed that the effect of GSR was stronger compared to higher regressor numbers, which implies
990 that WM regressors share common variance with the GS. Previous studies have shown that the GS derived either by the

991 whole brain or GM are very similar to each other and also that the GS is highly correlated with the mean time series
992 across voxels in WM and CSF (Kassinopoulos and Mitsis, 2019; Power et al., 2017), which further lends support to the
993 idea that WM regressors share common variance with the GS. Furthermore, we observed that the SLFOs that reflect
994 BOLD fluctuations due to changes in heart rate and breathing patterns, and account for a significant fraction of GS
995 fluctuations (Falahpour et al., 2013; Kassinopoulos and Mitsis, 2021, 2019), were well explained using the first 20-30
996 WM and CSF regressors (Fig. 1). This result suggests that the practice of considering PCA regressors from WM or CSF
997 exhibits to some extent similar effects to GSR. As a result, the effect of GSR when considering 200 WM regressors (i.e.,
998 WM_{GS}^{200} vs WM^{200}) is relatively small (Fig. 2-Fig. 3). In contrast, GSR has a strong effect on FIX denoising, which
999 suggests that the ICA regressors that are removed by FIX denoising do not share a large fraction of common variance
1000 with the GS. This is not surprising, as it has been suggested that spatial ICA used in FIX is, by design, unable to separate
1001 global temporal artifacts from fMRI data (Glasser et al., 2018). For instance, it has been shown that the default mode
1002 network identified with ICA is often confounded by variations in breathing patterns (Birn et al., 2008a). And since the
1003 BOLD fluctuations due to variations in breathing patterns or heart rate are in low frequencies (~0.1 Hz), FIX is unlikely
1004 to classify components that are confounded by these sources as noisy with the result of preserving global artifacts in the
1005 fMRI data.

1006 Despite the simplicity of GSR, there has been much debate about its use (Liu et al., 2017; Murphy and Fox, 2017). Even
1007 though several studies have shown that a large fraction of the GS is associated to physiological processes such as heart
1008 rate and breathing activity (Birn et al., 2006; Chang et al., 2009; Falahpour et al., 2013; Kassinopoulos and Mitsis, 2021,
1009 2019; Shmueli et al., 2007; Wise et al., 2004) as well as head motion (Power et al., 2014; Satterthwaite et al., 2013),
1010 there is accumulating evidence that GS is also driven by neuronal activity as assessed by intracranial recordings
1011 (Schölvinck et al., 2010) and vigilance-related measures (Chang et al., 2016; Falahpour et al., 2018; Liu and Falahpour,
1012 2020; Wong et al., 2016, 2013). Therefore, while our results are in support of GSR for both WM and FIX denoising, we
1013 cannot exclude the possibility of removing some neuronal-related fluctuations from the data when the GS is removed.
1014 Finally, we should acknowledge that several attempts have been made to address some of the limitations of GSR (Aquino
1015 et al., 2020; Carbonell et al., 2014, 2011; Erdoğan et al., 2016); however, whether the proposed techniques suppress
1016 physiological noise while also preserving neuronal activity still remains an open question.

1018 5. Conclusion

1019 In summary, the current study evaluated the performance of a large range of model-based and model-free techniques
1020 using previously proposed as well as novel QC metrics. As the QC metrics did not uniformly favor a specific
1021 preprocessing strategy, we proposed a framework that evaluates the sensitivity of each metric. Among eight QC metrics,
1022 *FCC* proposed here as well as *FDDVARS* employed in Muschelli et al. (2014) exhibited the highest sensitivity. *FCC*
1023 reflects the difference between WNE and BNE correlation values, whereas *FDDVARS* reflects the levels of motion
1024 artifacts in the parcel time series. Our results suggest that the choice of the preprocessing strategy to be employed in a
1025 study could be based solely on the metrics *FCC* and *FDDVARS*, where the former tends to favor relatively mild strategies
1026 for improving the identification of large-scale networks, while the latter is in favor of more aggressive strategies in an
1027 attempt to minimize the presence of motion artifacts.

1028 The data-driven approaches (WM denoising and FIX denoising) combined with GSR demonstrated the largest increase
1029 in SNR as well as reduction in motion artifacts and biases. In the case of WM denoising, using resting-state fMRI data
1030 from the HCP, we found that removing about 17% of the WM regressors yielded one of the largest improvements in QC
1031 scores. Scrubbing did not provide any gain to the data quality when it was followed by WM denoising, whereas low-pass
1032 filtering at 0.2 Hz led to an additional improvement, particularly when combined with mild variants of WM denoising.

1033 Similar conclusions were derived using three different functional atlases. However, unless the framework followed here
1034 is repeated with different datasets that vary in terms of the population examined or acquisition parameters (e.g. repetition
1035 time TR and duration of scan) we cannot be certain whether our conclusions can be directly generalized to other datasets.

1036 Therefore, we recommend investigators to consult the QC metrics when deciding about the pipeline they want to employ
1037 in a study. Finally, as has been suggested in previous studies (Ciric et al., 2017; Parkes et al., 2018), we recommend
1038 investigators to report scores of QC metrics for the preprocessed data so that readers can independently interpret the
1039 findings with respect to possible biases that can arise due to motion. To assist with this, we provide the codes used in
1040 this study (https://github.com/mkassinopoulos/Estimation_of_QC_metrics), which can be used for preprocessing of the
1041 data and estimation of the QC scores.

1042

1043 **Acknowledgments**

1044 This work was supported by the Natural Sciences and Engineering Research Council of Canada (Discovery Grant 34362
1045 awarded to GDM), the Fonds de la Recherche du Quebec - Nature et Technologies (FRQNT; Team Grant PR191780-
1046 2016 awarded to GDM) and the Canada First Research Excellence Fund (awarded to McGill University for the Healthy
1047 Brains for Healthy Lives initiative). MK acknowledges funding from Québec Bio-imaging Network (QBIN). Data were
1048 provided by the Human Connectome Project, WU-Minn Consortium (Principal Investigators: David Van Essen and
1049 Kamil Ugurbil; 1U54MH091657) funded by the 16 NIH Institutes and Centers that support the NIH Blueprint for
1050 Neuroscience Research; and by the McDonnell Center for Systems Neuroscience at Washington University. The authors
1051 would like to thank Alba Xifra-Porxas for her assistance in the selection of subjects from the HCP database with good
1052 quality physiological recordings.

1053

1054 **Conflict of interest**

1055 The authors declare no conflict of interest.

1056

1057 **Author contributions**

1058 Michalis Kassinosopoulos preprocessed and analyzed the data, designed the figures, interpreted the results, drafted the
1059 manuscript and arranged the final version. Georgios D. Mitsis contributed to the conceptualization of the research,
1060 supervised the findings, and edited and reviewed the manuscripts.

1061

1062 **Data and Code Availability Statement**

1063 For the purposes of this study we used resting-state scans from the Human Connectome Project (HCP) S1200 release
1064 (Matthew F Glasser et al., 2016; Van Essen et al., 2013) which are publicly available and can be found at
1065 <https://www.humanconnectome.org/>. Furthermore, the codes written for this work are publicly available and can be
1066 found at https://github.com/mkassinopoulos/Estimation_of_QC_metrics.

1068

References

- 1069 Aquino, K.M., Fulcher, B.D., Parkes, L., Sabaroedin, K., Fornito, A., 2020. Identifying and removing widespread signal
1070 deflections from fMRI data: Rethinking the global signal regression problem. *Neuroimage* 212, 116614.
1071 <https://doi.org/10.1016/j.neuroimage.2020.116614>
- 1072 Behzadi, Y., Restom, K., Liaw, J., Liu, T.T., 2007. A component based noise correction method (CompCor) for BOLD
1073 and perfusion based fMRI. *Neuroimage* 37, 90–101. <https://doi.org/10.1016/j.neuroimage.2007.04.042>
- 1074 Bijsterbosch, J., Harrison, S., Duff, E., Alfaro-Almagro, F., Woolrich, M., Smith, S., 2017. Investigations into within-
1075 and between-subject resting-state amplitude variations. *Neuroimage* 159, 57–69.
1076 <https://doi.org/10.1016/j.neuroimage.2017.07.014>
- 1077 Bijsterbosch, J.D., Woolrich, M.W., Glasser, M.F., Robinson, E.C., Beckmann, C.F., Van Essen, D.C., Harrison, S.J.,
1078 Smith, S.M., 2018. The relationship between spatial configuration and functional connectivity of brain regions.
1079 *Elife* 7, 210195. <https://doi.org/10.7554/eLife.32992>
- 1080 Birn, R.M., 2012. The role of physiological noise in resting-state functional connectivity. *Neuroimage* 62, 864–870.
1081 <https://doi.org/10.1016/j.neuroimage.2012.01.016>
- 1082 Birn, R.M., Cornejo, M.D., Molloy, E.K., Patriat, R., Meier, T.B., Kirk, G.R., Nair, V.A., Meyerand, M.E., Prabhakaran,
1083 V., 2014. The Influence of Physiological Noise Correction on Test–Retest Reliability of Resting-State Functional
1084 Connectivity. *Brain Connect.* 4, 511–522. <https://doi.org/10.1089/brain.2014.0284>
- 1085 Birn, R.M., Diamond, J.B., Smith, M.A., Bandettini, P.A., 2006. Separating respiratory-variation-related fluctuations
1086 from neuronal-activity-related fluctuations in fMRI. *Neuroimage* 31, 1536–48.
1087 <https://doi.org/10.1016/j.neuroimage.2006.02.048>
- 1088 Birn, R.M., Murphy, K., Bandettini, P.A., 2008a. The effect of respiration variations on independent component analysis
1089 results of resting state functional connectivity. *Hum. Brain Mapp.* <https://doi.org/10.1002/hbm.20577>
- 1090 Birn, R.M., Smith, M. a., Jones, T.B., Bandettini, P. a., 2008b. The respiration response function: The temporal dynamics
1091 of fMRI signal fluctuations related to changes in respiration. *Neuroimage* 40, 644–654.
1092 <https://doi.org/10.1016/j.neuroimage.2007.11.059>
- 1093 Biswal, B., Yetkin, F.Z., Haughton, V.M., Hyde, J.S., 1995. Functional connectivity in the motor cortex of resting human
1094 brain using echo-planar MRI. *Magn. Reson. Med.* 34, 537–541. <https://doi.org/10.1002/mrm.1910340409>
- 1095 Bright, M.G., Tench, C.R., Murphy, K., 2017. Potential pitfalls when denoising resting state fMRI data using nuisance
1096 regression. *Neuroimage* 154, 159–168. <https://doi.org/10.1016/j.neuroimage.2016.12.027>
- 1097 Burgess, G.C., Kandala, S., Nolan, D., Laumann, T.O., Power, J.D., Adeyemo, B., Harms, M.P., Petersen, S.E., Barch,
1098 D.M., 2016. Evaluation of Denoising Strategies to Address Motion-Related Artifacts in Resting-State Functional
1099 Magnetic Resonance Imaging Data from the Human Connectome Project. *Brain Connect.* 6, 669–680.
1100 <https://doi.org/10.1089/brain.2016.0435>
- 1101 Caballero-Gaudes, C., Reynolds, R.C., 2017. Methods for cleaning the BOLD fMRI signal. *Neuroimage* 154, 128–149.
1102 <https://doi.org/10.1016/j.neuroimage.2016.12.018>
- 1103 Carbonell, F., Bellec, P., Shmuel, A., 2014. Quantification of the impact of a confounding variable on functional
1104 connectivity confirms anti-correlated networks in the resting-state. *Neuroimage* 86, 343–353.
1105 <https://doi.org/10.1016/j.neuroimage.2013.10.013>
- 1106 Carbonell, F., Bellec, P., Shmuel, A., 2011. Global and System-Specific Resting-State fMRI Fluctuations Are
1107 Uncorrelated: Principal Component Analysis Reveals Anti-Correlated Networks. *Brain Connect.* 1, 496–510.
1108 <https://doi.org/10.1089/brain.2011.0065>
- 1109 Chai, X.J., Castañán, A.N., Öngür, D., Whitfield-Gabrieli, S., 2012. Anticorrelations in resting state networks without
1110 global signal regression. *Neuroimage* 59, 1420–1428. <https://doi.org/10.1016/j.neuroimage.2011.08.048>

- 1111 Chang, C., Cunningham, J.P., Glover, G.H., 2009. Influence of heart rate on the BOLD signal: The cardiac response
1112 function. *Neuroimage* 44, 857–869. <https://doi.org/10.1016/j.neuroimage.2008.09.029>
- 1113 Chang, C., Glover, G.H., 2009. Effects of model-based physiological noise correction on default mode network anti-
1114 correlations and correlations. *Neuroimage* 47, 1448–1459. <https://doi.org/10.1016/j.neuroimage.2009.05.012>
- 1115 Chang, C., Leopold, D.A., Schölvinck, M.L., Mandelkow, H., Picchioni, D., Liu, X., Ye, F.Q., Turchi, J.N., Duyn, J.H.,
1116 2016. Tracking brain arousal fluctuations with fMRI. *Proc. Natl. Acad. Sci.* 113, 4518–4523.
1117 <https://doi.org/10.1073/pnas.1520613113>
- 1118 Chen, J.E., Glover, G.H., 2015. BOLD fractional contribution to resting-state functional connectivity above 0.1Hz.
1119 *Neuroimage* 107, 207–218. <https://doi.org/10.1016/j.neuroimage.2014.12.012>
- 1120 Chen, J.E., Lewis, L.D., Chang, C., Tian, Q., Fultz, N.E., Ohringer, N.A., Rosen, B.R., Polimeni, J.R., 2020. Resting-
1121 state “physiological networks.” *Neuroimage* 213, 116707. <https://doi.org/10.1016/j.neuroimage.2020.116707>
- 1122 Ciric, R., Rosen, A.F.G., Erus, G., Cieslak, M., Adebimpe, A., Cook, P.A., Bassett, D.S., Davatzikos, C., Wolf, D.H.,
1123 Satterthwaite, T.D., 2018. Mitigating head motion artifact in functional connectivity MRI. *Nat. Protoc.* 13, 2801–
1124 2826. <https://doi.org/10.1038/s41596-018-0065-y>
- 1125 Ciric, R., Wolf, D.H., Power, J.D., Roalf, D.R., Baum, G.L., Ruparel, K., Shinohara, R.T., Elliott, M.A., Eickhoff, S.B.,
1126 Davatzikos, C., Gur, R.C., Gur, R.E., Bassett, D.S., Satterthwaite, T.D., 2017. Benchmarking of participant-level
1127 confound regression strategies for the control of motion artifact in studies of functional connectivity. *Neuroimage*
1128 154, 174–187. <https://doi.org/10.1016/j.neuroimage.2017.03.020>
- 1129 Cisler, J.M., 2017. Childhood trauma and functional connectivity between amygdala and medial prefrontal cortex: A
1130 dynamic functional connectivity and large-scale network perspective. *Front. Syst. Neurosci.* 11, 1–11.
1131 <https://doi.org/10.3389/fnsys.2017.00029>
- 1132 Dagli, M.S., Ingeholm, J.E., Haxby, J. V., 1999. Localization of cardiac-induced signal change in fMRI. *Neuroimage* 9,
1133 407–415. <https://doi.org/10.1006/nimg.1998.0424>
- 1134 Damoiseaux, J.S., Rombouts, S.A.R.B., Barkhof, F., Scheltens, P., Stam, C.J., Smith, S.M., Beckmann, C.F., 2006.
1135 Consistent resting-state networks.
- 1136 Demirtaş, M., Tornador, C., Falcón, C., López-Solà, M., Hernández-Ribas, R., Pujol, J., Menchón, J.M., Ritter, P.,
1137 Cardoner, N., Soriano-Mas, C., Deco, G., 2016. Dynamic functional connectivity reveals altered variability in
1138 functional connectivity among patients with major depressive disorder. *Hum. Brain Mapp.* 00.
1139 <https://doi.org/10.1002/hbm.23215>
- 1140 Erdoğan, S.B., Tong, Y., Hocke, L.M., Lindsey, K.P., deB Frederick, B., 2016. Correcting resting state fMRI-BOLD
1141 signals for blood arrival time enhances functional connectivity analysis. *Front. Hum. Neurosci.* 10, 311.
1142 <https://doi.org/10.3389/FNHUM.2016.00311>
- 1143 Falahpour, M., Chang, C., Wong, C.W., Liu, T.T., 2018. Template-based prediction of vigilance fluctuations in resting-
1144 state fMRI. *Neuroimage* 174, 317–327. <https://doi.org/10.1016/j.neuroimage.2018.03.012>
- 1145 Falahpour, M., Refai, H., Bodurka, J., 2013. Subject specific BOLD fMRI respiratory and cardiac response functions
1146 obtained from global signal. *Neuroimage* 72, 252–264. <https://doi.org/10.1016/j.neuroimage.2013.01.050>
- 1147 Finn, E.S., Shen, X., Scheinost, D., Rosenberg, M.D., Huang, J., Chun, M.M., Papademetris, X., Constable, R.T., 2015.
1148 Functional connectome fingerprinting: identifying individuals using patterns of brain connectivity. *Nat. Neurosci.*
1149 18, 1664–1671. <https://doi.org/10.1038/nn.4135>
- 1150 Fox, M.D., Snyder, A.Z., Vincent, J.L., Corbetta, M., Van Essen, D.C., Raichle, M.E., 2005. The human brain is
1151 intrinsically organized into dynamic, anticorrelated functional networks. *Proc. Natl. Acad. Sci. U. S. A.* 102, 9673–
1152 8. <https://doi.org/10.1073/pnas.0504136102>
- 1153 Glasser, M.F., Coalson, T.S., Bijsterbosch, J.D., Harrison, S.J., Harms, M.P., Anticevic, A., Van Essen, D.C., Smith,

- 1154 S.M., 2018. Using temporal ICA to selectively remove global noise while preserving global signal in functional
1155 MRI data. *Neuroimage* 181, 692–717. <https://doi.org/10.1016/j.neuroimage.2018.04.076>
- 1156 Glasser, Matthew F., Coalson, T.S., Robinson, E.C., Hacker, C.D., Harwell, J., Yacoub, E., Ugurbil, K., Andersson, J.,
1157 Beckmann, C.F., Jenkinson, M., Smith, S.M., Van Essen, D.C., 2016. A multi-modal parcellation of human cerebral
1158 cortex. *Nature* 536, 171–178. <https://doi.org/10.1038/nature18933>
- 1159 Glasser, Matthew F., Smith, S.M., Marcus, D.S., Andersson, J.L.R., Auerbach, E.J., Behrens, T.E.J., Coalson, T.S.,
1160 Harms, M.P., Jenkinson, M., Moeller, S., Robinson, E.C., Sotiropoulos, S.N., Xu, J., Yacoub, E., Ugurbil, K., Van
1161 Essen, D.C., 2016. The Human Connectome Project’s neuroimaging approach. *Nat. Neurosci.* 19, 1175–87.
1162 <https://doi.org/10.1038/nn.4361>
- 1163 Glasser, M.F., Sotiropoulos, S.N., Wilson, J.A., Coalson, T.S., Fischl, B., Andersson, J.L., Xu, J., Jbabdi, S., Webster,
1164 M., Polimeni, J.R., Van Essen, D.C., Jenkinson, M., 2013. The minimal preprocessing pipelines for the Human
1165 Connectome Project. *Neuroimage* 80, 105–124. <https://doi.org/10.1016/j.neuroimage.2013.04.127>
- 1166 Glover, G.H., Li, T.-Q., Ress, D., 2000. Image-based method for retrospective correction of physiological motion effects
1167 in fMRI: RETROICOR. *Magn. Reson. Med.* 44, 162–167. [https://doi.org/10.1002/1522-
1168 2594\(200007\)44:1<162::AID-MRM23>3.0.CO;2-E](https://doi.org/10.1002/1522-2594(200007)44:1<162::AID-MRM23>3.0.CO;2-E)
- 1169 Gordon, E.M., Laumann, T.O., Adeyemo, B., Huckins, J.F., Kelley, W.M., Petersen, S.E., 2016. Generation and
1170 Evaluation of a Cortical Area Parcellation from Resting-State Correlations. *Cereb. Cortex* 26, 288–303.
1171 <https://doi.org/10.1093/cercor/bhu239>
- 1172 Grajauskas, L.A., Frizzell, T., Song, X., D’Arcy, R.C.N., 2019. White Matter fMRI Activation Cannot Be Treated as a
1173 Nuisance Regressor: Overcoming a Historical Blind Spot. *Front. Neurosci.* 13, 2007–2010.
1174 <https://doi.org/10.3389/fnins.2019.01024>
- 1175 Gratton, C., Dworetzky, A., Coalson, R.S., Adeyemo, B., Laumann, T.O., Wig, G.S., Kong, T.S., Gratton, G., Fabiani,
1176 M., Barch, D.M., Tranel, D., Dominguez, O.M., Fair, D.A., Dosenbach, N.U.F., Snyder, A.Z., Perlmuter, J.S.,
1177 Petersen, S.E., Campbell, M.C., 2020. Removal of high frequency contamination from motion estimates in single-
1178 band fMRI saves data without biasing functional connectivity. *Neuroimage* 217, 116866.
1179 <https://doi.org/10.1016/j.neuroimage.2020.116866>
- 1180 Jackson, D.A., 2016. Stopping Rules in Principal Components Analysis : A Comparison of Heuristical and Statistical
1181 Approaches Stable URL : <http://www.jstor.org/stable/1939574> REFERENCES Linked references are available on
1182 JSTOR for this article : You may need to log in to JSTO 74, 2204–2214.
- 1183 Kassinopoulos, M., Harper, R.M., Guye, M., Lemieux, L., Diehl, B., 2021. Altered Relationship Between Heart Rate
1184 Variability and fMRI-Based Functional Connectivity in People With Epilepsy. *Front. Neurol.* 12, 1–13.
1185 <https://doi.org/10.3389/fneur.2021.671890>
- 1186 Kassinopoulos, M., Mitsis, G.D., 2021. Physiological noise modeling in fMRI based on the pulsatile component of
1187 photoplethysmograph. *Neuroimage* 242, 118467. <https://doi.org/10.1016/j.neuroimage.2021.118467>
- 1188 Kassinopoulos, M., Mitsis, G.D., 2019. Identification of physiological response functions to correct for fluctuations in
1189 resting-state fMRI related to heart rate and respiration. *Neuroimage* 202, 116150.
1190 <https://doi.org/10.1016/j.neuroimage.2019.116150>
- 1191 Laumann, T.O., Snyder, A.Z., Mitra, A., Gordon, E.M., Gratton, C., Adeyemo, B., Gilmore, A.W., Nelson, S.M., Berg,
1192 J.J., Greene, D.J., McCarthy, J.E., Tagliazucchi, E., Laufs, H., Schlaggar, B.L., Dosenbach, N.U.F., Petersen, S.E.,
1193 2017. On the Stability of BOLD fMRI Correlations. *Cereb. Cortex* 27, 4719–4732.
1194 <https://doi.org/10.1093/cercor/bhw265>
- 1195 Lemieux, L., Salek-Haddadi, A., Lund, T.E., Laufs, H., Carmichael, D., 2007. Modelling large motion events in fMRI
1196 studies of patients with epilepsy. *Magn. Reson. Imaging* 25, 894–901. <https://doi.org/10.1016/j.mri.2007.03.009>
- 1197 Leonardi, N., Richiardi, J., Gschwind, M., Simioni, S., Annoni, J.M., Schlupe, M., Vuilleumier, P., Van De Ville, D.,

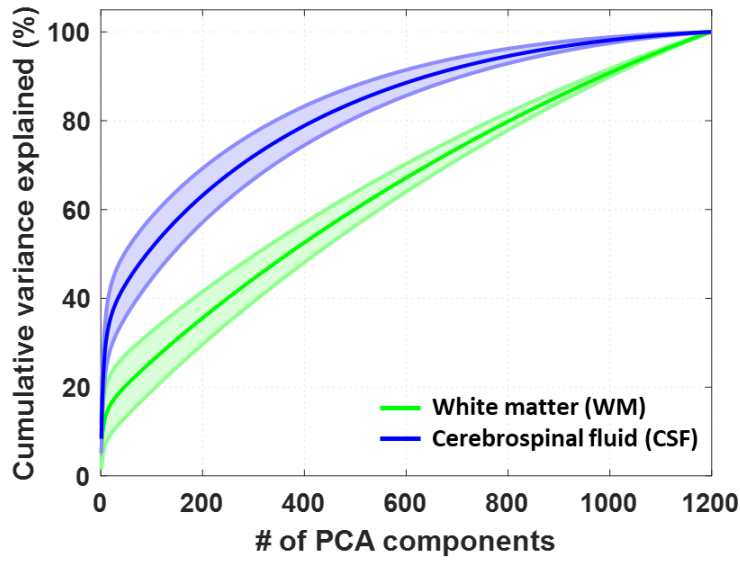
- 1198 2013. Principal components of functional connectivity: A new approach to study dynamic brain connectivity during
1199 rest. *Neuroimage* 83, 937–950. <https://doi.org/10.1016/j.neuroimage.2013.07.019>
- 1200 Leonardi, N., Van De Ville, D., 2015. On spurious and real fluctuations of dynamic functional connectivity during rest.
1201 *Neuroimage* 104, 430–436. <https://doi.org/10.1016/j.neuroimage.2014.09.007>
- 1202 Li, J., Kong, R., Liégeois, R., Orban, C., Tan, Y., Sun, N., Holmes, A.J., Sabuncu, M.R., Ge, T., Yeo, B.T.T., 2019.
1203 Global signal regression strengthens association between resting-state functional connectivity and behavior.
1204 *Neuroimage* 196, 126–141. <https://doi.org/10.1016/j.neuroimage.2019.04.016>
- 1205 Liu, T.T., 2016. Noise contributions to the fMRI signal: An overview. *Neuroimage* 143, 141–151.
1206 <https://doi.org/10.1016/j.neuroimage.2016.09.008>
- 1207 Liu, T.T., Falahpour, M., 2020. Vigilance Effects in Resting-State fMRI 14. <https://doi.org/10.3389/fnins.2020.00321>
- 1208 Liu, T.T., Nalci, A., Falahpour, M., 2017. The global signal in fMRI: Nuisance or Information? *Neuroimage* 150, 213–
1209 229. <https://doi.org/10.1016/j.neuroimage.2017.02.036>
- 1210 Mulcahy, J.S., Larsson, D.E.O., Garfinkel, S.N., Critchley, H.D., 2019. Heart rate variability as a biomarker in health
1211 and affective disorders: A perspective on neuroimaging studies. *Neuroimage* 202, 116072.
1212 <https://doi.org/10.1016/j.neuroimage.2019.116072>
- 1213 Murphy, K., Birn, R.M., Bandettini, P.A., 2013. Resting-state fMRI confounds and cleanup. *Neuroimage* 80, 349–359.
1214 <https://doi.org/10.1016/j.neuroimage.2013.04.001>
- 1215 Murphy, K., Fox, M.D., 2017. Towards a consensus regarding global signal regression for resting state functional
1216 connectivity MRI. *Neuroimage* 154, 169–173. <https://doi.org/10.1016/j.neuroimage.2016.11.052>
- 1217 Muschelli, J., Nebel, M.B., Caffo, B.S., Barber, A.D., Pekar, J.J., Mostofsky, S.H., 2014. Reduction of motion-related
1218 artifacts in resting state fMRI using aCompCor. *Neuroimage* 96, 22–35.
1219 <https://doi.org/10.1016/j.neuroimage.2014.03.028>
- 1220 Niazy, R.K., Xie, J., Miller, K., Beckmann, C.F., Smith, S.M., 2011. Spectral characteristics of resting state networks,
1221 1st ed, Progress in Brain Research. Elsevier B.V. <https://doi.org/10.1016/B978-0-444-53839-0.00017-X>
- 1222 Parkes, L., Fulcher, B., Yücel, M., Fornito, A., 2018. An evaluation of the efficacy, reliability, and sensitivity of motion
1223 correction strategies for resting-state functional MRI. *Neuroimage* 171, 415–436.
1224 <https://doi.org/10.1016/j.neuroimage.2017.12.073>
- 1225 Patriat, R., Reynolds, R.C., Birn, R.M., 2017. An improved model of motion-related signal changes in fMRI. *Neuroimage*
1226 144, 74–82. <https://doi.org/10.1016/j.neuroimage.2016.08.051>
- 1227 Perlberg, V., Bellec, P., Anton, J.L., Péligrini-Issac, M., Doyon, J., Benali, H., 2007. CORSICA: correction of structured
1228 noise in fMRI by automatic identification of ICA components. *Magn. Reson. Imaging* 25, 35–46.
1229 <https://doi.org/10.1016/j.mri.2006.09.042>
- 1230 Pervaiz, U., Vidaurre, D., Woolrich, M.W., Smith, S.M., 2020. Optimising network modelling methods for fMRI.
1231 *Neuroimage* 211, 116604. <https://doi.org/10.1016/j.neuroimage.2020.116604>
- 1232 Power, J.D., Barnes, K.A., Snyder, A.Z., Schlaggar, B.L., Petersen, S.E., 2012. Spurious but systematic correlations in
1233 functional connectivity MRI networks arise from subject motion. *Neuroimage* 59, 2142–2154.
1234 <https://doi.org/10.1016/j.neuroimage.2011.10.018>
- 1235 Power, J.D., Lynch, C.J., Dubin, M.J., Silver, B.M., Martin, A., Jones, R.M., 2020. Characteristics of respiratory
1236 measures in young adults scanned at rest, including systematic changes and “missed” deep breaths. *Neuroimage*
1237 204, 116234. <https://doi.org/10.1016/j.neuroimage.2019.116234>
- 1238 Power, J.D., Lynch, C.J., Silver, B.M., Dubin, M.J., Martin, A., Jones, R.M., 2019. Distinctions among real and apparent
1239 respiratory motions in human fMRI data. *Neuroimage* 201, 116041.

- 1240 <https://doi.org/10.1016/j.neuroimage.2019.116041>
- 1241 Power, J.D., Mitra, A., Laumann, T.O., Snyder, A.Z., Schlaggar, B.L., Petersen, S.E., 2014. Methods to detect,
1242 characterize, and remove motion artifact in resting state fMRI. *Neuroimage* 84, 320–341.
1243 <https://doi.org/10.1016/j.neuroimage.2013.08.048>
- 1244 Power, J.D., Plitt, M., Laumann, T.O., Martin, A., 2017. Sources and implications of whole-brain fMRI signals in
1245 humans. *Neuroimage* 146, 609–625. <https://doi.org/10.1016/j.neuroimage.2016.09.038>
- 1246 Power, J.D., Schlaggar, B.L., Petersen, S.E., 2015. Recent progress and outstanding issues in motion correction in resting
1247 state fMRI. *Neuroimage* 105, 536–551. <https://doi.org/10.1016/j.neuroimage.2014.10.044>
- 1248 Prokopiou, P.C., Pattinson, K.T.S., Wise, R.G., Mitsis, G.D., 2019. Modeling of dynamic cerebrovascular reactivity to
1249 spontaneous and externally induced CO₂ fluctuations in the human brain using BOLD-fMRI. *Neuroimage* 186,
1250 533–548. <https://doi.org/10.1016/j.neuroimage.2018.10.084>
- 1251 Pruim, R.H.R., Mennes, M., Buitelaar, J.K., Beckmann, C.F., 2015a. Evaluation of ICA-AROMA and alternative
1252 strategies for motion artifact removal in resting state fMRI. *Neuroimage* 112, 278–287.
1253 <https://doi.org/10.1016/j.neuroimage.2015.02.063>
- 1254 Pruim, R.H.R., Mennes, M., van Rooij, D., Llera, A., Buitelaar, J.K., Beckmann, C.F., 2015b. ICA-AROMA: A robust
1255 ICA-based strategy for removing motion artifacts from fMRI data. *Neuroimage* 112, 267–277.
1256 <https://doi.org/10.1016/j.neuroimage.2015.02.064>
- 1257 Raichle, M.E., MacLeod, A.M., Snyder, A.Z., Powers, W.J., Gusnard, D.A., Shulman, G.L., 2001. A default mode of
1258 brain function. *Proc. Natl. Acad. Sci. U. S. A.* 98, 676–682. <https://doi.org/10.1073/pnas.98.2.676>
- 1259 Raj, D., Anderson, A.W., Gore, J.C., 2001. Respiratory effects in human functional magnetic resonance imaging due to
1260 bulk susceptibility changes. *Phys. Med. Biol.* 46, 3331–3340. <https://doi.org/10.1088/0031-9155/46/12/318>
- 1261 Raj, D., Paley, D.P., Anderson, A.W., Kennan, R.P., Gore, J.C., 2000. A model for susceptibility artefacts from
1262 respiration in functional echo-planar magnetic resonance imaging. *Phys. Med. Biol.* 45, 3809–3820.
1263 <https://doi.org/10.1088/0031-9155/45/12/321>
- 1264 Roy, A.K., Shehzad, Z., Margulies, D.S., Kelly, A.M.C., Uddin, L.Q., Gotimer, K., Biswal, B.B., Castellanos, F.X.,
1265 Milham, M.P., 2009. Functional connectivity of the human amygdala using resting state fMRI. *Neuroimage* 45,
1266 614–626. <https://doi.org/10.1016/j.neuroimage.2008.11.030>
- 1267 Rubinov, M., Sporns, O., 2010. Complex network measures of brain connectivity: Uses and interpretations. *Neuroimage*
1268 52, 1059–1069. <https://doi.org/10.1016/j.neuroimage.2009.10.003>
- 1269 Salimi-Khorshidi, G., Douaud, G., Beckmann, C.F., Glasser, M.F., Griffanti, L., Smith, S.M., 2014. Automatic denoising
1270 of functional MRI data: Combining independent component analysis and hierarchical fusion of classifiers.
1271 *Neuroimage* 90, 449–468. <https://doi.org/10.1016/j.neuroimage.2013.11.046>
- 1272 Satterthwaite, T.D., Ciric, R., Roalf, D.R., Davatzikos, C., Bassett, D.S., Wolf, D.H., 2019. Motion artifact in studies of
1273 functional connectivity: Characteristics and mitigation strategies. *Hum. Brain Mapp.* 40, 2033–2051.
1274 <https://doi.org/10.1002/hbm.23665>
- 1275 Satterthwaite, T.D., Elliott, M.A., Gerraty, R.T., Ruparel, K., Loughhead, J., Calkins, M.E., Eickhoff, S.B., Hakonarson,
1276 H., Gur, R.C., Gur, R.E., Wolf, D.H., 2013. An improved framework for confound regression and filtering for
1277 control of motion artifact in the preprocessing of resting-state functional connectivity data. *Neuroimage* 64, 240–
1278 256. <https://doi.org/10.1016/j.neuroimage.2012.08.052>
- 1279 Satterthwaite, T.D., Wolf, D.H., Loughhead, J., Ruparel, K., Elliott, M.A., Hakonarson, H., Gur, R.C., Gur, R.E., 2012.
1280 Impact of in-scanner head motion on multiple measures of functional connectivity: Relevance for studies of
1281 neurodevelopment in youth. *Neuroimage* 60, 623–632. <https://doi.org/10.1016/j.neuroimage.2011.12.063>
- 1282 Schölvinck, M.L., Maier, A., Ye, F.Q., Duyn, J.H., Leopold, D.A., 2010. Neural basis of global resting-state fMRI

- 1283 activity. *Proc. Natl. Acad. Sci. U. S. A.* 107, 10238–43. <https://doi.org/10.1073/pnas.0913110107>
- 1284 Seitzman, B.A., Gratton, C., Marek, S., Raut, R. V., Dosenbach, N.U.F., Schlaggar, B.L., Petersen, S.E., Greene, D.J.,
1285 2020. A set of functionally-defined brain regions with improved representation of the subcortex and cerebellum.
1286 *Neuroimage* 206, 116290. <https://doi.org/10.1016/j.neuroimage.2019.116290>
- 1287 Shirer, W.R., Jiang, H., Price, C.M., Ng, B., Greicius, M.D., 2015. Optimization of rs-fMRI Pre-processing for Enhanced
1288 Signal-Noise Separation, Test-Retest Reliability, and Group Discrimination. *Neuroimage* 117, 67–79.
1289 <https://doi.org/10.1016/j.neuroimage.2015.05.015>
- 1290 Shmueli, K., van Gelderen, P., de Zwart, J. a., Horovitz, S.G., Fukunaga, M., Jansma, J.M., Duyn, J.H., 2007. Low-
1291 frequency fluctuations in the cardiac rate as a source of variance in the resting-state fMRI BOLD signal.
1292 *Neuroimage* 38, 306–320. <https://doi.org/10.1016/j.neuroimage.2007.07.037>
- 1293 Shrout, P.E., Fleiss, J.L., 1979. Intraclass correlations: Uses in assessing rater reliability. *Psychol. Bull.* 86, 420–428.
1294 <https://doi.org/10.1037/0033-2909.86.2.420>
- 1295 Siegel, J.S., Mitra, A., Laumann, T.O., Seitzman, B.A., Raichle, M., Corbetta, M., Snyder, A.Z., 2017. Data Quality
1296 Influences Observed Links Between Functional Connectivity and Behavior. *Cereb. Cortex* 27, 4492–4502.
1297 <https://doi.org/10.1093/cercor/bhw253>
- 1298 Smith, S.M., Beckmann, C.F., Andersson, J., Auerbach, E.J., Bijsterbosch, J., Douaud, G., Duff, E., Feinberg, D.A.,
1299 Griffanti, L., Harms, M.P., Kelly, M., Laumann, T., Miller, K.L., Moeller, S., Petersen, S., Power, J., Salimi-
1300 Khorshidi, G., Snyder, A.Z., Vu, A.T., Woolrich, M.W., Xu, J., Yacoub, E., Uğurbil, K., Van Essen, D.C., Glasser,
1301 M.F., 2013a. Resting-state fMRI in the Human Connectome Project. *Neuroimage* 80, 144–168.
1302 <https://doi.org/10.1016/j.neuroimage.2013.05.039>
- 1303 Smith, S.M., Fox, P.T., Miller, K.L., Glahn, D.C., Fox, P.M., Mackay, C.E., Filippini, N., Watkins, K.E., Toro, R., Laird,
1304 A.R., Beckmann, C.F., 2009. Correspondence of the brain’s functional architecture during activation and rest. *Proc.*
1305 *Natl. Acad. Sci. U. S. A.* 106, 13040–5. <https://doi.org/10.1073/pnas.0905267106>
- 1306 Smith, S.M., Nichols, T.E., Vidaurre, D., Winkler, A.M., Behrens, T.E.J., Glasser, M.F., Ugurbil, K., Barch, D.M., Van
1307 Essen, D.C., Miller, K.L., 2015. A positive-negative mode of population covariation links brain connectivity,
1308 demographics and behavior. *Nat. Neurosci.* 18, 1565–1567. <https://doi.org/10.1038/nn.4125>
- 1309 Smith, S.M., Vidaurre, D., Beckmann, C.F., Glasser, M.F., Jenkinson, M., Miller, K.L., Nichols, T.E., Robinson, E.C.,
1310 Salimi-Khorshidi, G., Woolrich, M.W., Barch, D.M., Uğurbil, K., Van Essen, D.C., 2013b. Functional
1311 connectomics from resting-state fMRI. *Trends Cogn. Sci.* 17, 666–682. <https://doi.org/10.1016/j.tics.2013.09.016>
- 1312 Tong, Y., Hocke, L.M., Frederick, B.B., 2019. Low frequency systemic hemodynamic “noise” in resting state BOLD
1313 fMRI: Characteristics, causes, implications, mitigation strategies, and applications. *Front. Neurosci.* 13.
1314 <https://doi.org/10.3389/fnins.2019.00787>
- 1315 Urchs, S., Armoza, J., Benhajali, Y., St-Aubin, J., Orban, P., Bellec, P., 2017. MIST: A multi-resolution parcellation of
1316 functional brain networks. *MNI Open Res.* 1, 3. <https://doi.org/10.12688/mniopenres.12767.1>
- 1317 van Dijk, K.R.A., Sabuncu, M.R., Buckner, R.L., 2012. The influence of head motion on intrinsic functional connectivity
1318 MRI. *Neuroimage* 59, 431–438. <https://doi.org/10.1016/j.neuroimage.2011.07.044>
- 1319 Van Essen, D.C., Glasser, M.F., 2018. Parcellating Cerebral Cortex: How Invasive Animal Studies Inform Noninvasive
1320 Mapmaking in Humans. *Neuron* 99, 640–663. <https://doi.org/10.1016/j.neuron.2018.07.002>
- 1321 Van Essen, D.C., Smith, S.M., Barch, D.M., Behrens, T.E.J., Yacoub, E., Ugurbil, K., 2013. The WU-Minn Human
1322 Connectome Project: An overview. *Neuroimage* 80, 62–79. <https://doi.org/10.1016/j.neuroimage.2013.05.041>
- 1323 Wang, J., Ren, Y., Hu, X., Nguyen, V.T., Guo, L., Han, J., Guo, C.C., 2017. Test–retest reliability of functional
1324 connectivity networks during naturalistic fMRI paradigms. *Hum. Brain Mapp.* 38, 2226–2241.
1325 <https://doi.org/10.1002/hbm.23517>

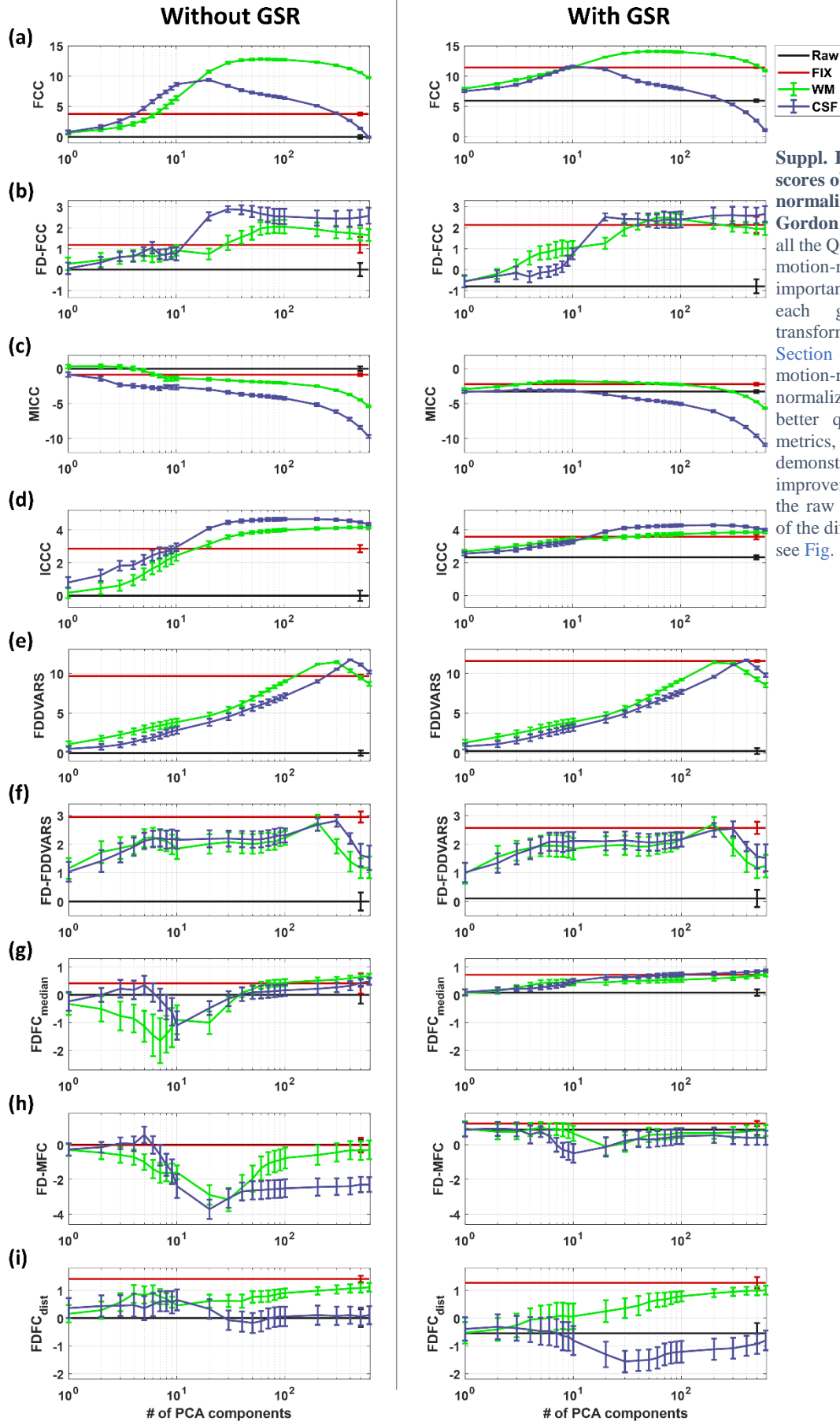
- 1326 Whittaker, J.R., Driver, I.D., Venzi, M., Bright, M.G., Murphy, K., Chen, J., Whittaker, J.R., 2019. Cerebral
1327 Autoregulation Evidenced by Synchronized Low Frequency Oscillations in Blood Pressure and Resting-State fMRI
1328 13, 1–12. <https://doi.org/10.3389/fnins.2019.00433>
- 1329 Wise, R.G., Ide, K., Poulin, M.J., Tracey, I., 2004. Resting fluctuations in arterial carbon dioxide induce significant low
1330 frequency variations in BOLD signal. *Neuroimage* 21, 1652–1664.
1331 <https://doi.org/10.1016/j.neuroimage.2003.11.025>
- 1332 Wong, C.W., DeYoung, P.N., Liu, T.T., 2016. Differences in the resting-state fMRI global signal amplitude between the
1333 eyes open and eyes closed states are related to changes in EEG vigilance. *Neuroimage* 124, 24–31.
1334 <https://doi.org/10.1016/j.neuroimage.2015.08.053>
- 1335 Wong, C.W., Olafsson, V., Tal, O., Liu, T.T., 2013. The amplitude of the resting-state fMRI global signal is related to
1336 EEG vigilance measures. *Neuroimage* 83, 983–990. <https://doi.org/10.1016/j.neuroimage.2013.07.057>
- 1337 Woodward, N.D., Cascio, C.J., 2015. Resting-State Functional Connectivity in Psychiatric Disorders. *JAMA psychiatry*
1338 72, 743–744. <https://doi.org/10.1001/jamapsychiatry.2015.0101.2>
- 1339 Xia, C.H., Ma, Z., Ciric, R., Gu, S., Betzel, R.F., Kaczkurkin, A.N., Calkins, M.E., Cook, P.A., García de la Garza, A.,
1340 Vandekar, S.N., Cui, Z., Moore, T.M., Roalf, D.R., Ruparel, K., Wolf, D.H., Davatzikos, C., Gur, R.C.R.E., Gur,
1341 R.C.R.E., Shinohara, R.T., Bassett, D.S., Satterthwaite, T.D., Figures, S., Tables, S., 2018. Linked dimensions of
1342 psychopathology and connectivity in functional brain networks. *Nat. Commun.* 9, 1–14.
1343 <https://doi.org/10.1038/s41467-018-05317-y>
- 1344 Xiao, Y., Friederici, A.D., Margulies, D.S., Brauer, J., 2016. Longitudinal changes in resting-state fMRI from age 5 to
1345 age 6years covary with language development. *Neuroimage* 128, 116–124.
1346 <https://doi.org/10.1016/j.neuroimage.2015.12.008>
- 1347 Xifra-Porxas, A., Kassinosopoulos, M., Mitsis, G.D., 2021. Physiological and motion signatures in static and time-varying
1348 functional connectivity and their subject identifiability. *Elife* 10, e62324. <https://doi.org/10.7554/eLife.62324>
- 1349 Yan, C.G., Cheung, B., Kelly, C., Colcombe, S., Craddock, R.C., Di Martino, A., Li, Q., Zuo, X.N., Castellanos, F.X.,
1350 Milham, M.P., 2013. A comprehensive assessment of regional variation in the impact of head micromovements on
1351 functional connectomics. *Neuroimage* 76, 183–201. <https://doi.org/10.1016/j.neuroimage.2013.03.004>
- 1352 Zhang, C., Dougherty, C.C., Baum, S.A., White, T., Michael, A.M., 2018. Functional connectivity predicts gender:
1353 Evidence for gender differences in resting brain connectivity. *Hum. Brain Mapp.* 39, 1765–1776.
1354 <https://doi.org/10.1002/hbm.23950>
- 1355 Zhang, Y., Brady, M., Smith, S., 2001. Segmentation of brain MR images through a hidden Markov random field model
1356 and the expectation-maximization algorithm. *IEEE Trans. Med. Imaging* 20, 45–57.
1357 <https://doi.org/10.1109/42.906424>
- 1358
- 1359

Supplementary Material

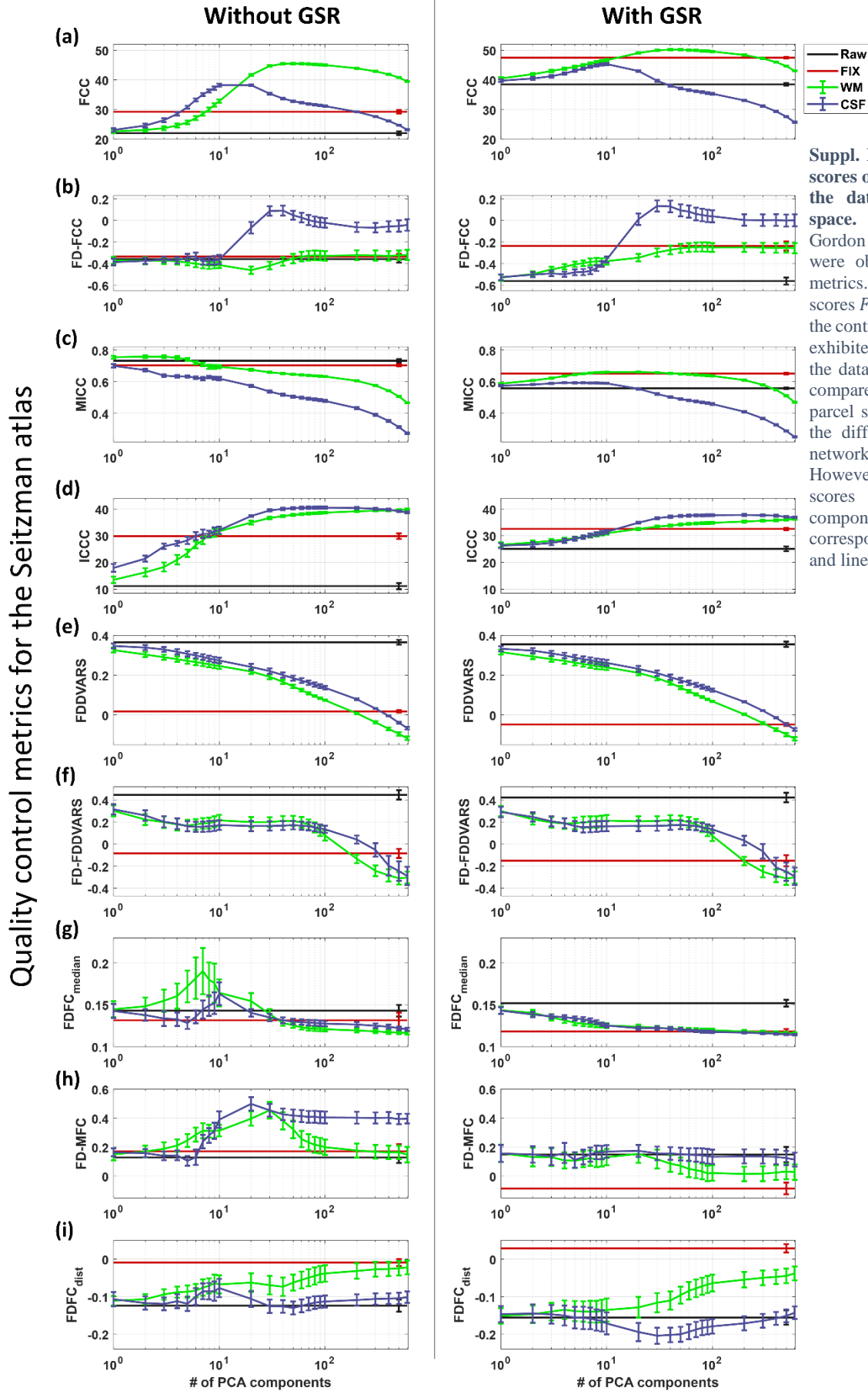


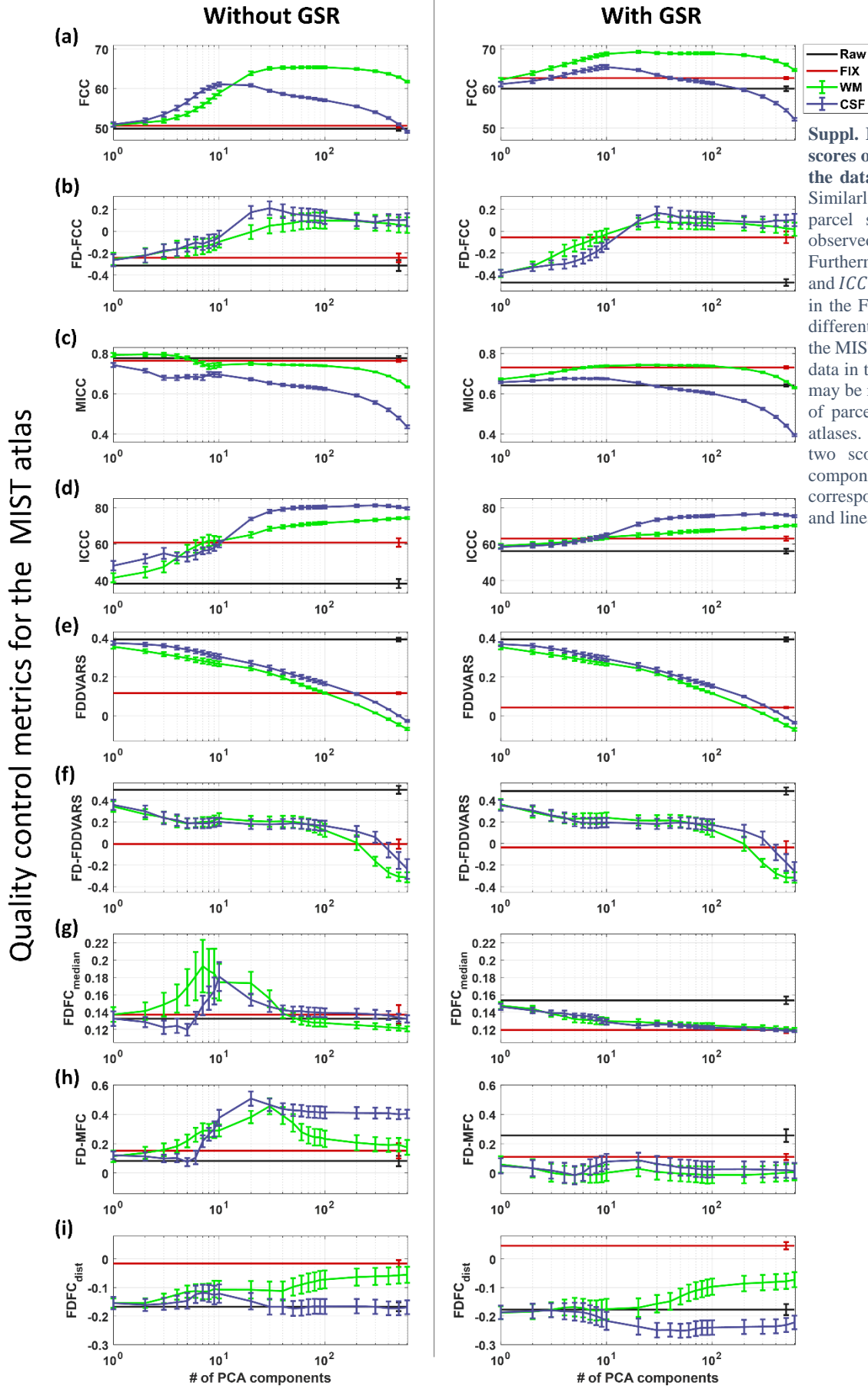
Suppl. Fig. 1. Cumulative variance explained (%) for PCA regressors obtained from WM and CSF. About 360 (± 60) WM and 90 (± 40) CSF regressors were required to explain 50% of the variance in the WM and CSF compartments, respectively. These numbers correspond to the number of PCA regressors to be removed from the fMRI data according to the variant of aCompCor proposed in Muschelli et al. (2014). The first 200 WM regressors used in WM^{200} correspond to an average explained variance of $36 \pm 6\%$.

Quality control metrics for the Gordon atlas (normalized)

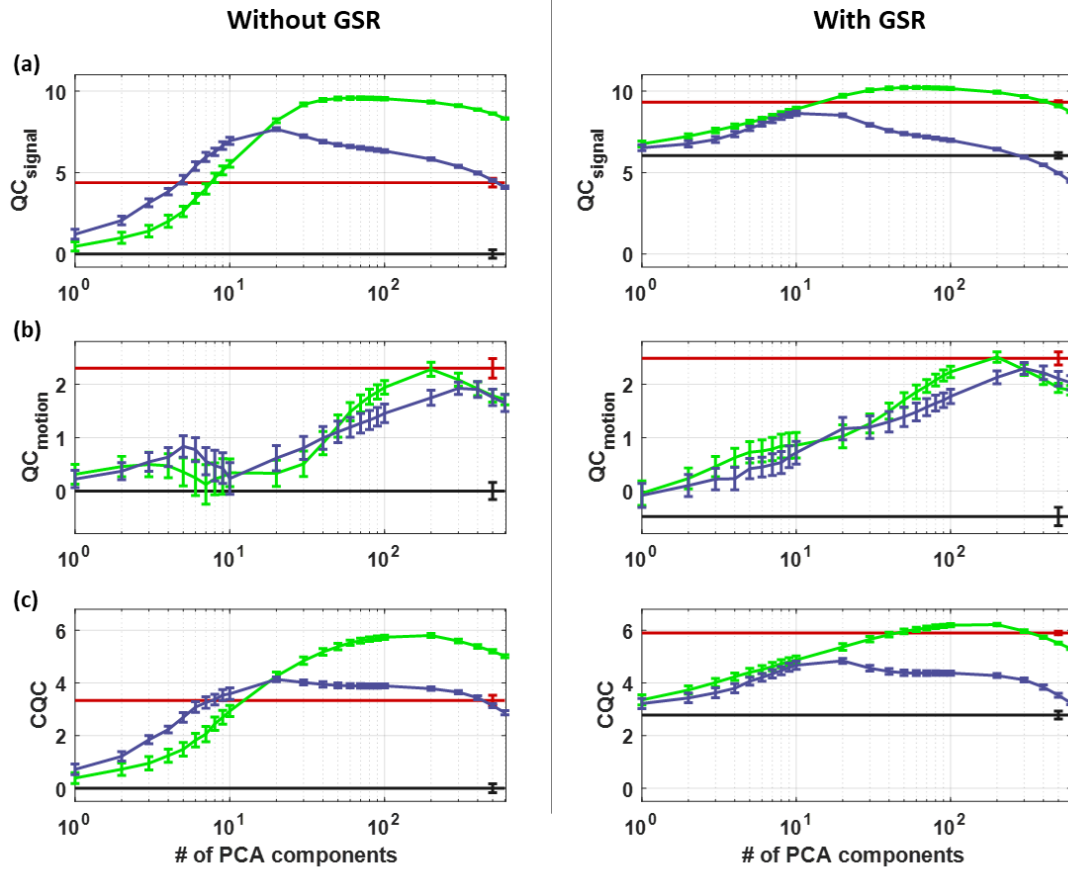


Suppl. Fig. 2. Quality control (QC) scores obtained by aCompCor, after normalization, using the data in the Gordon parcel space. To summarize all the QC metrics to signal-related and motion-related metrics it was important that the obtained scores from each group of subjects were transformed to Z-scores as described in Section 2.7. For both signal- and motion-related metrics, high normalized scores corresponded to better quality of data. Among all metrics, *FCC* and *FDDVARS* demonstrated the most significant improvement in quality with respect to the raw data. For the correspondence of the different curves and lines please see Fig. 2.



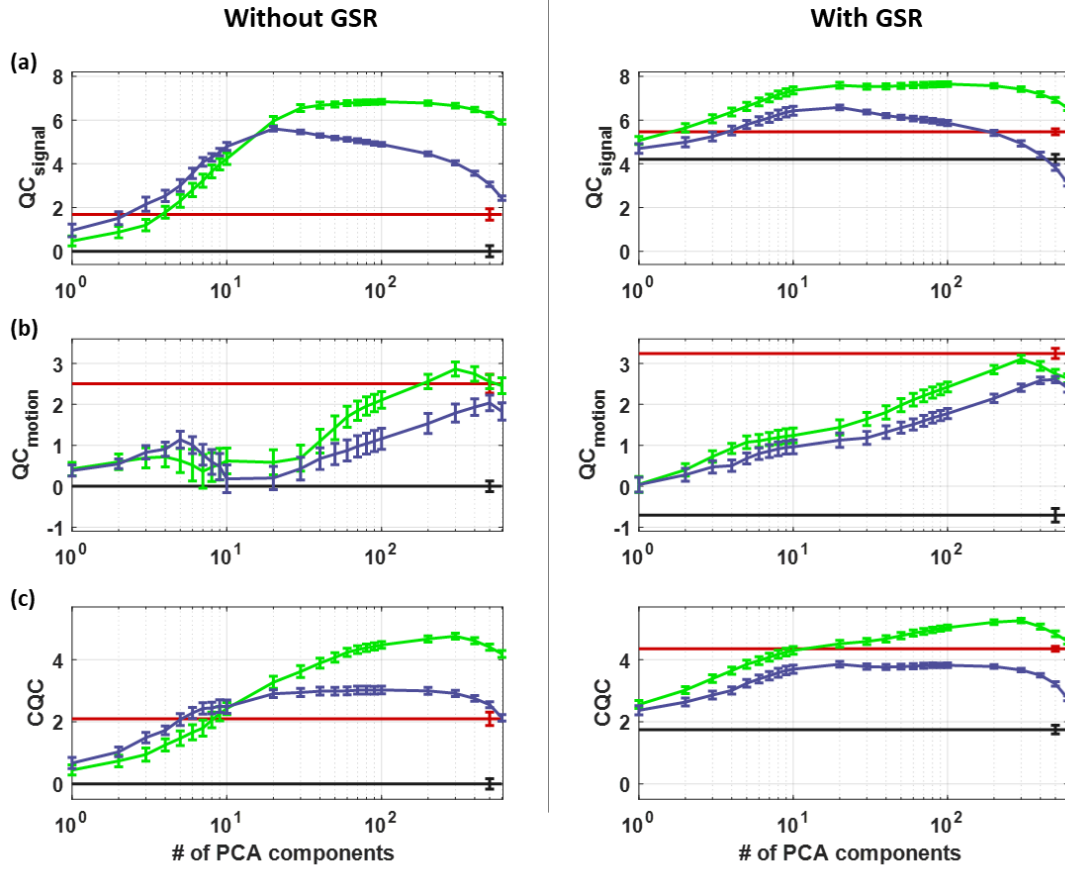


Summary of quality control (QC) metrics for the Seitzman atlas



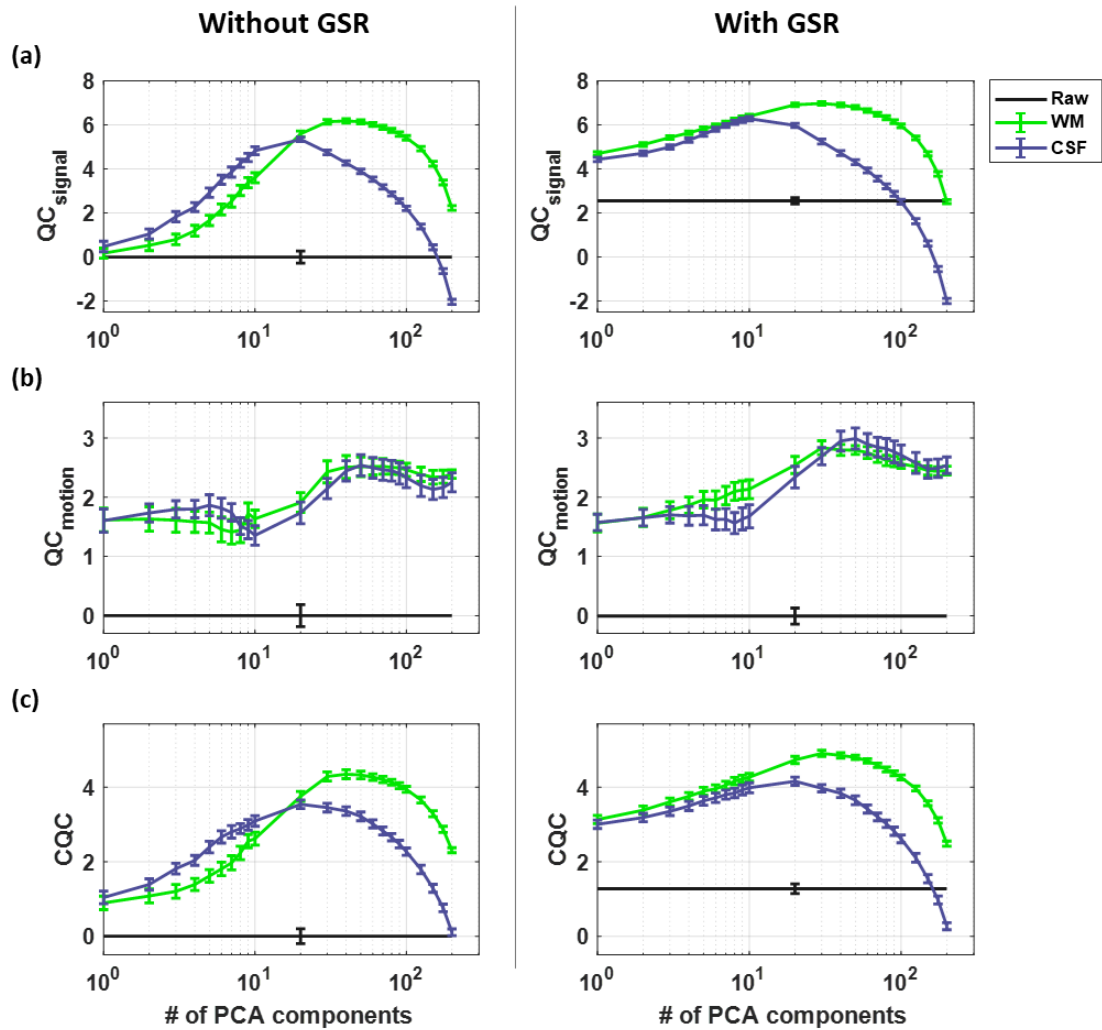
Suppl. Fig. 5. Summarized QC scores obtained by aCompCor using the data in the Seitzman parcel space. Similarly to the data in the Gordon parcel space (Fig. 3), GSR and white matter denoising with 50 to 100 PCA regressors yielded the highest scores for QC_{signal} whereas the more aggressive set of regressors WM_{GS}^{200} achieved the highest score in QC_{motion} . Overall, the CQC score that accounts for both C_{signal} and QC_{motion} yielded its highest value when the set WM_{GS}^{200} was used.

Summary of quality control (QC) metrics for the MIST atlas



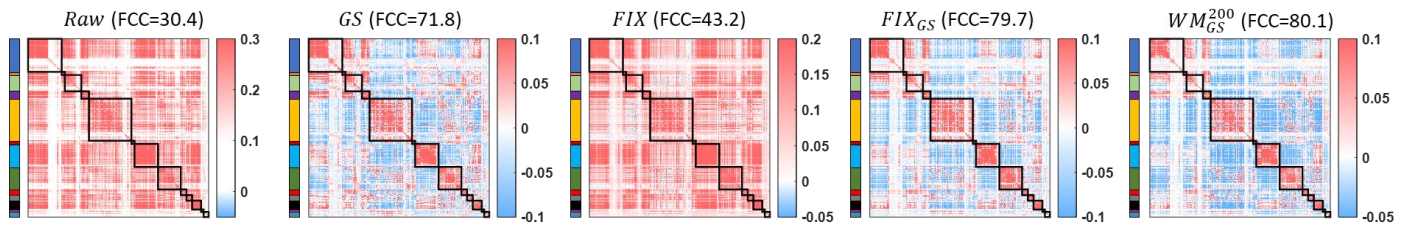
Suppl. Fig. 6. Summarized QC scores obtained by aCompCor using the data in the MIST parcel space. In the MIST parcel space, the QC_{signal} was kept relatively stable at its highest score for a larger range of sets ($WM_{GS}^{10} - WM_{GS}^{200}$) compared to the QC_{signal} in the Gordon and Seitzman parcel space. Moreover, the QC_{motion} yielded its highest score for the set WM_{GS}^{300} . As a result, the set WM_{GS}^{300} exhibited the highest score for the CQC as well.

Summary of QC metrics for fMRI data downsampled to TR=2.88 s (Gordon atlas)

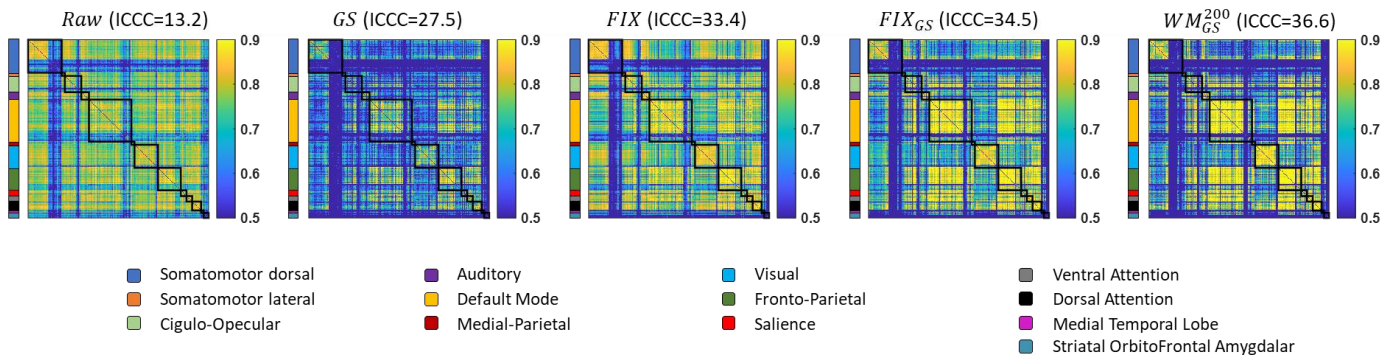


Suppl. Fig. 7. Summarized QC scores obtained from the fMRI data after being downsampled to TR=2.88 s (Gordon atlas). About 20 to 40 PCA regressors from WM were needed in order to achieve high QC_{signal} scores, while 50 regressors from either WM or CSF yielded the highest score in QC_{motion} . Among all sets of regressors, WM_{65}^{30} yielded the highest score (4.9) for the CQC metric.

FC matrix averaged across all scans for different pipelines (Seitzman atlas)

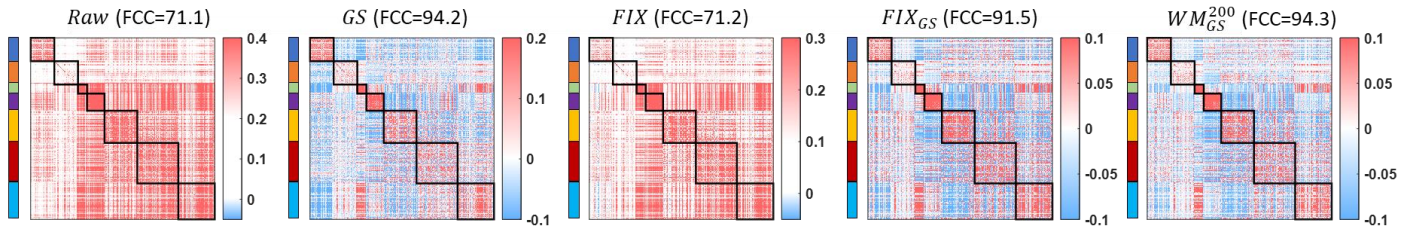


ICC matrix considering all scans for different pipelines (Seitzman atlas)

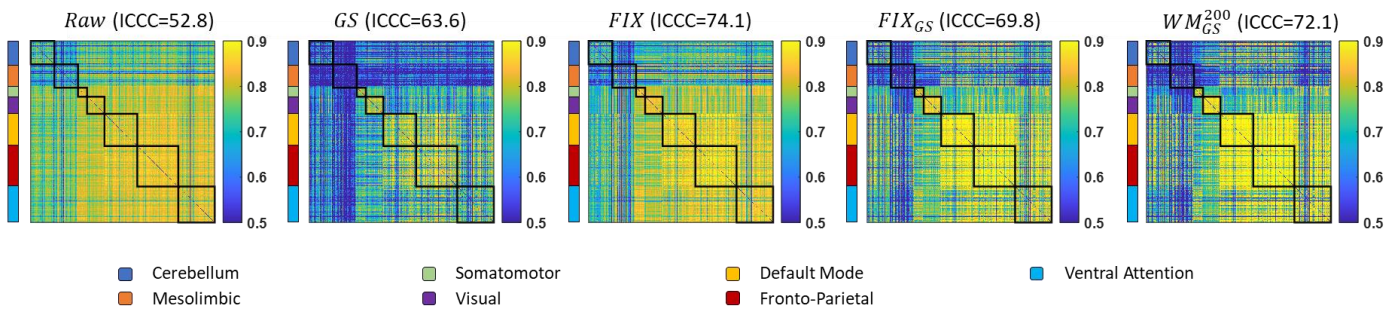


Suppl. Fig. 8. FC (top) and ICC (bottom) matrices considering all scans for different pipelines obtained from the data in the Seitzman parcel space. The pipelines WM_{GS}^{200} and FIX_{GS} significantly improved the identifiability of the networks. Note that many parcels appeared at the end of each network illustrated low correlation and ICC values. These parcels correspond to subcortical parcels and as reported by Seitzman et al. (2020), those parcels demonstrated low temporal signal-to-noise (SNR) in the HCP data which may explain the low correlation and ICC values observed here. Similar to the data in the Gordon parcel space, a large number of BNEs, and especially edges corresponding to interactions between the default mode and fronto-parietal networks, exhibited low FC values but high ICC values.

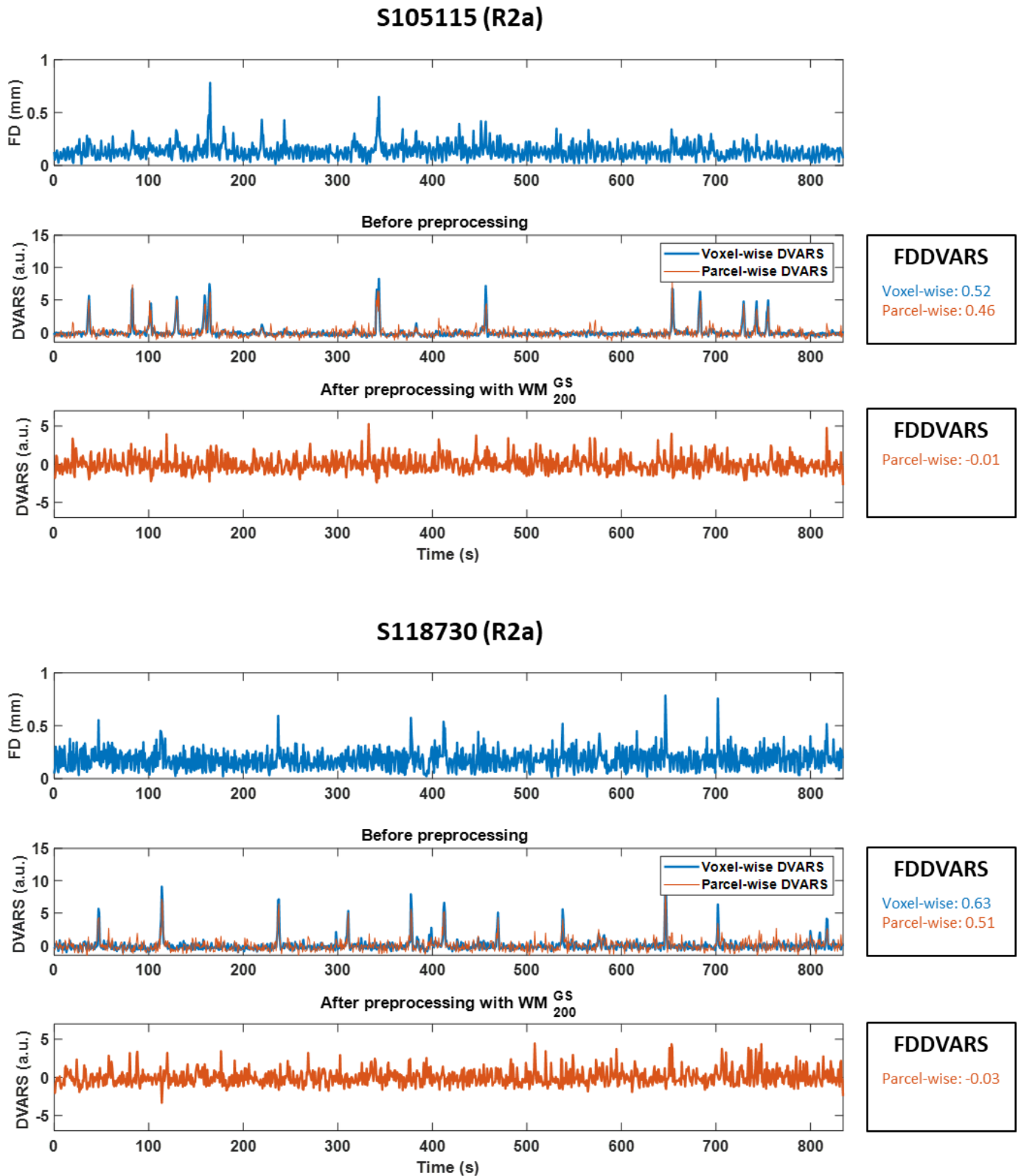
FC matrix averaged across all scans for different pipelines (MIST atlas)



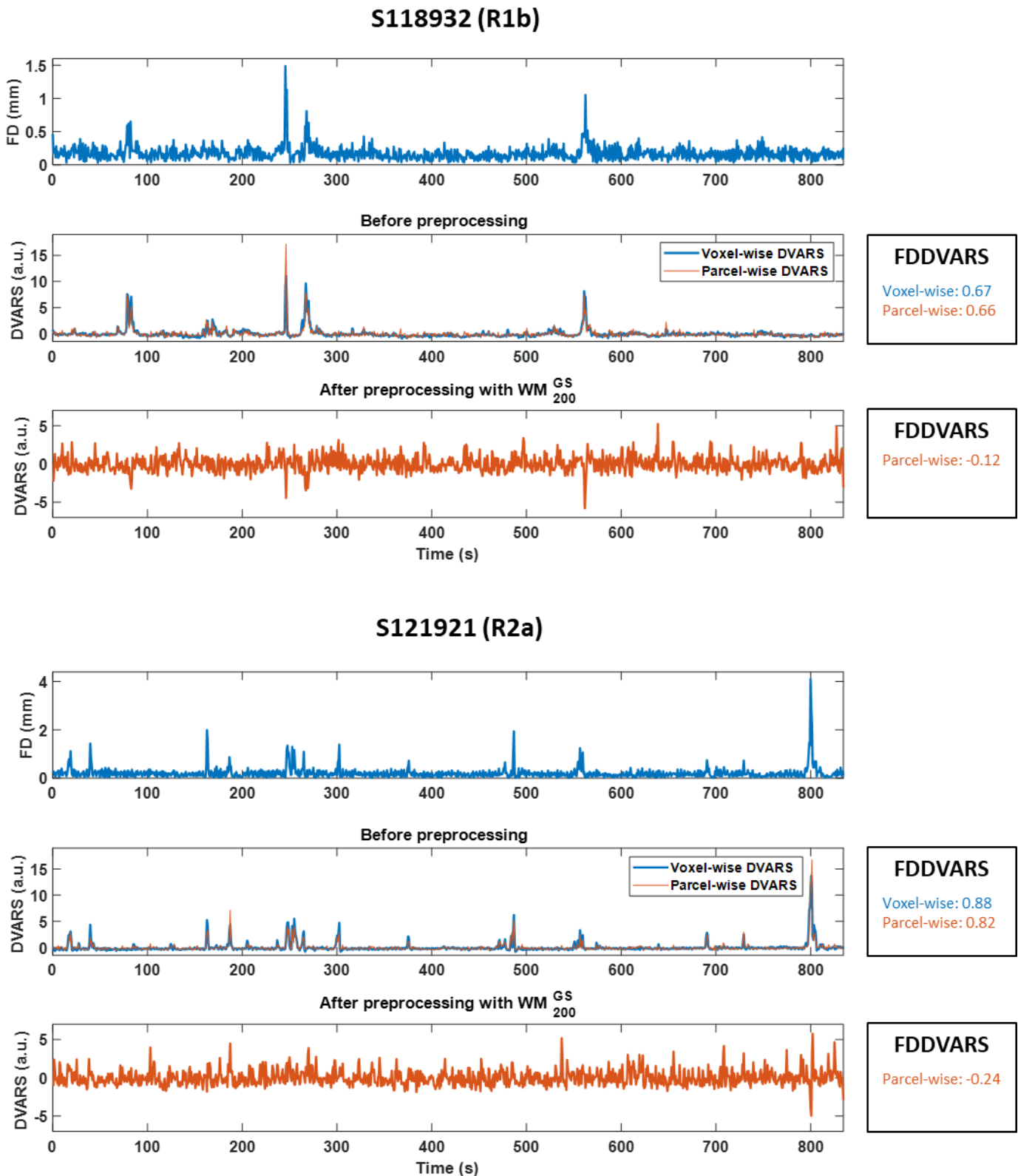
ICC matrix considering all scans for different pipelines (MIST atlas)



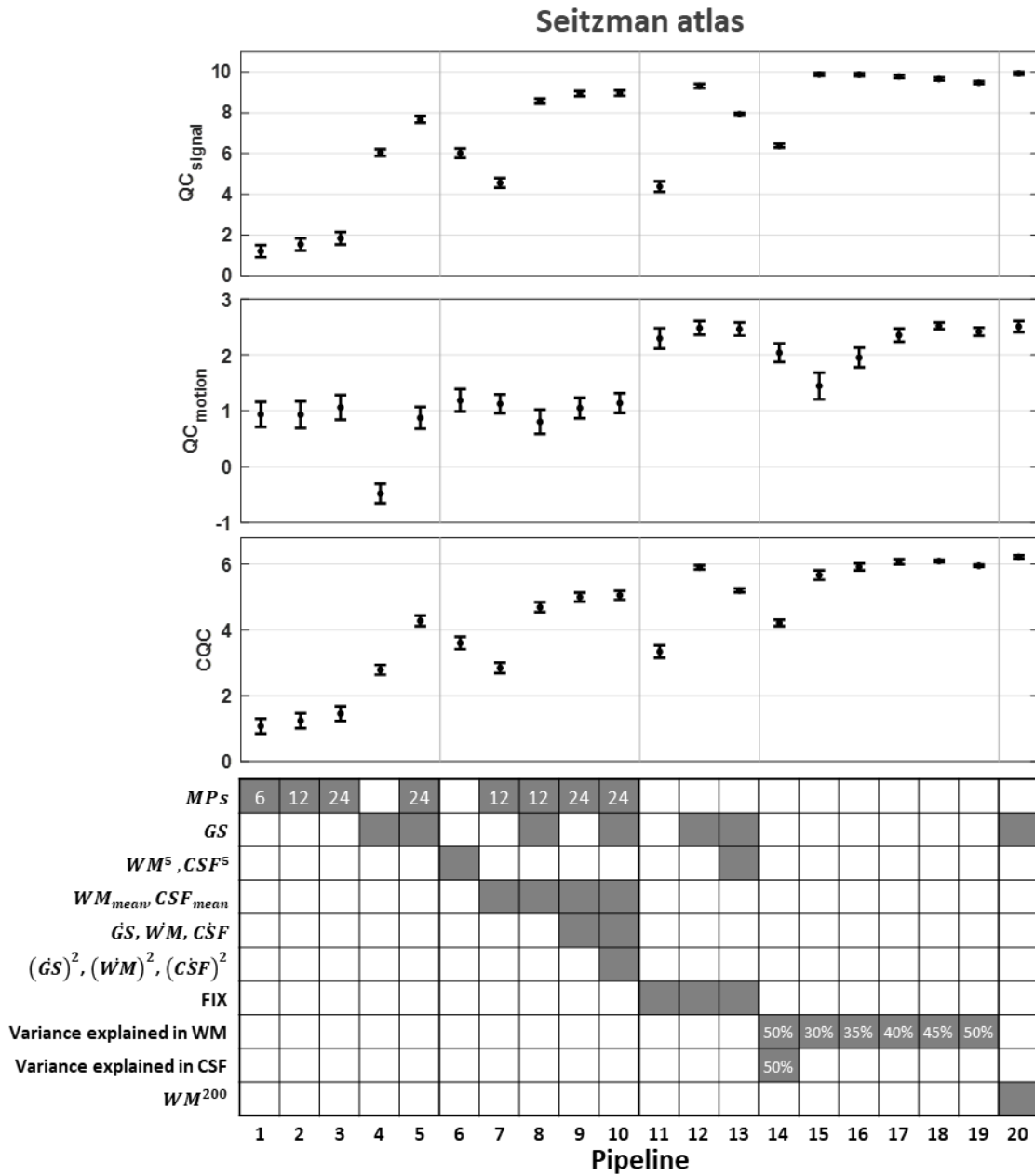
Suppl. Fig. 9. FC (top) and ICC (bottom) matrices considering all scans for different pipelines obtained from the data in the MIST parcel space. Based on the *FCC* scores obtained from the group-level FC matrices, the pipelines WM_{GS}^{200} and FIX_{GS} significantly improved the identifiability of the networks. However, similar *FCC* score was observed when only the GS was regressed out. On the other hand, as seen in [Suppl. Fig. 3a](#), on a scan-specific basis analysis, the *FCC* scores between the pipelines *GS*, FIX_{GS} and WM_{GS}^{200} presented significant differences. Moreover, we observe that, similar to the data in the Gordon parcel space, a large number of BNEs, and especially edges corresponding to interactions between the default mode and fronto-parietal networks, exhibited low FC values but high ICC values.



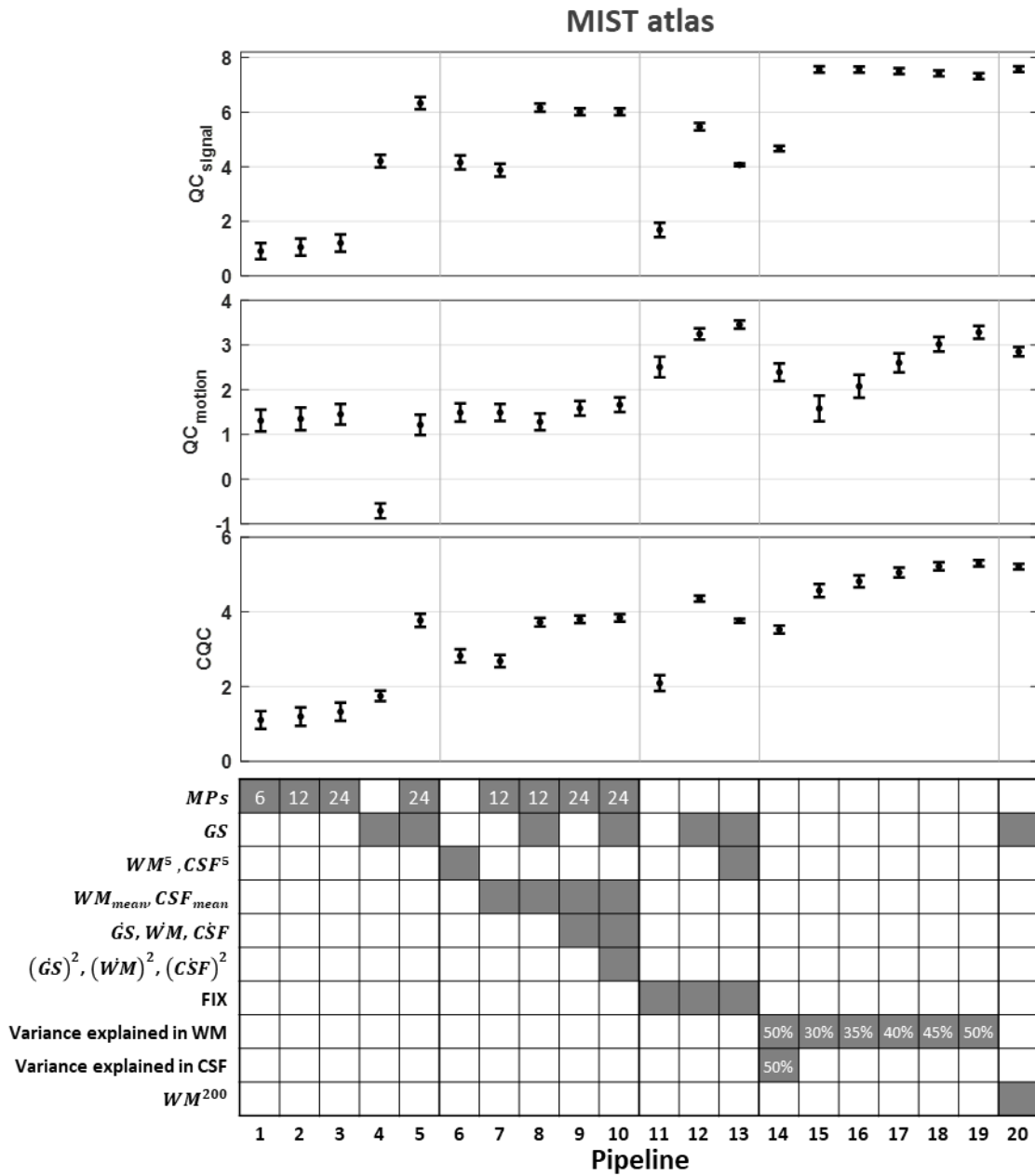
Suppl. Fig. 10. Traces of *DVARS* time-series for two scans for which WM denoising (WM_{GS}^{200}) reduced the corresponding *FDDVARS* values (i.e. correlation of *FD* and *DVARS*) close to zero. For the raw data, *DVARS*, either estimated at the voxel- or parcel-level, exhibited frequent spikes at times of motion, as assessed with *FD*, which resulted in *FDDVARS* values above 0.45. Parcel-wise *FDDVARS* values were on average lower than voxel-wise *FDDVARS* (0.37 ± 0.19 vs 0.53 ± 0.20). After WM denoising, the spikes in *DVARS* were significantly attenuated, resulting in *FDDVARS* values close to zero (0.02 ± 0.06).



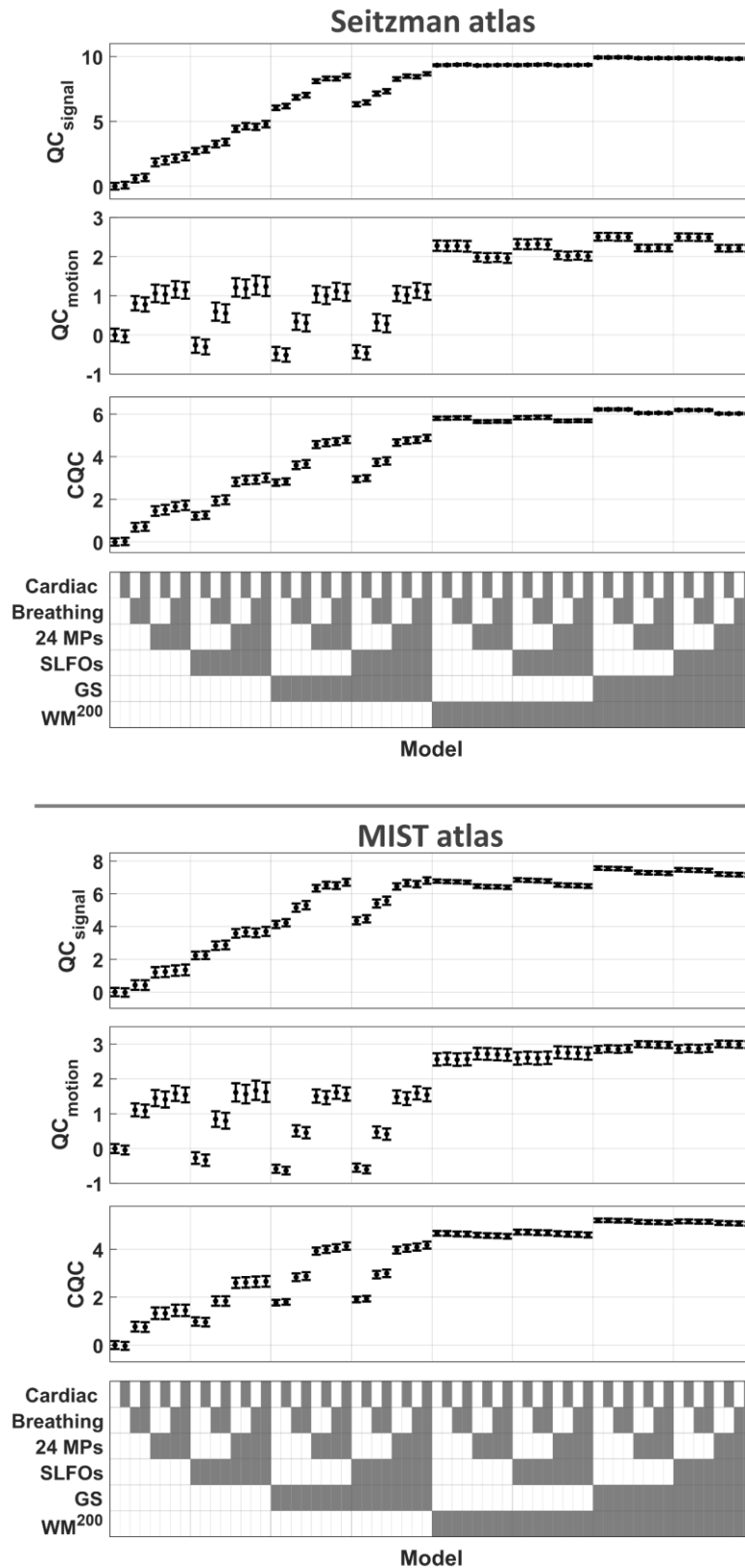
Suppl. Fig. 11. Traces of *DVARS* time-series for two scans for which WM_{GS}^{200} resulted in negative *FDDVARS* values. In some scans, while most of the spikes in *DVARS* were significantly attenuated after WM_{GS}^{200} , the sign of some spikes reversed from positive to negative which resulted in negative *FDDVARS* values (e.g. spikes at 670 s and 800 s for scans S118932 (R1b) and S121921 (R2a), respectively). As suggested by Power et al. (2020), these *DVARS* dips indicate that the framewise changes in fMRI time series are abnormally low at those times. As negative *FDDVARS* values may be associated with the presence of *DVARS* dips at times with motion, and these dips can presumably lead to systematic confounds, *FDDVARS* values, similar to the rest of the motion-related QC metrics, were normalized to $1 - \text{abs}(FDDVARS)$ so that a high positive value of normalized *FDDVARS* is assigned to good quality data.



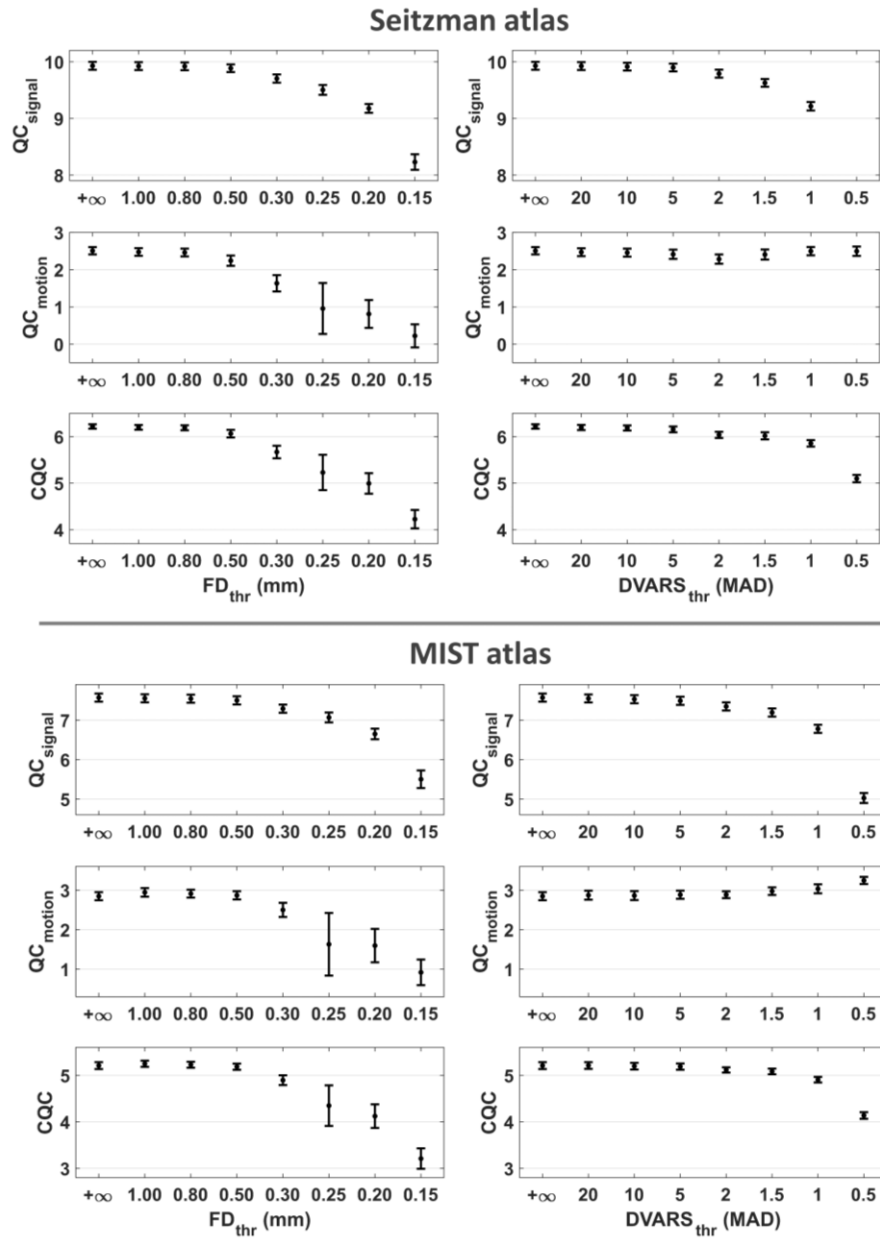
Suppl. Fig. 12. Evaluation of data-driven NCTs (Seitzman atlas). Twenty different data-driven pipelines were examined, as listed in Table 1. Similar to the Gordon atlas, among all pipelines, pipelines that included GSR and WM or FIX denoising yielded the highest scores in QC_{signal} , QC_{motion} and CQC (i.e., pipelines 12 and 17-20).



Suppl. Fig. 13. Evaluation of data-driven NCTs (MIST atlas). Twenty different data-driven pipelines were examined, as listed in Table 1. Similar to the Gordon atlas, among all pipelines, pipelines that included GSR and WM denoising yielded the highest scores in QC_{signal} , QC_{motion} and CQC (i.e., pipelines 17-20). The FIX denoising (pipeline 12) yielded a smaller improvement in QC_{signal} compared to the Gordon and Seitzman atlases.

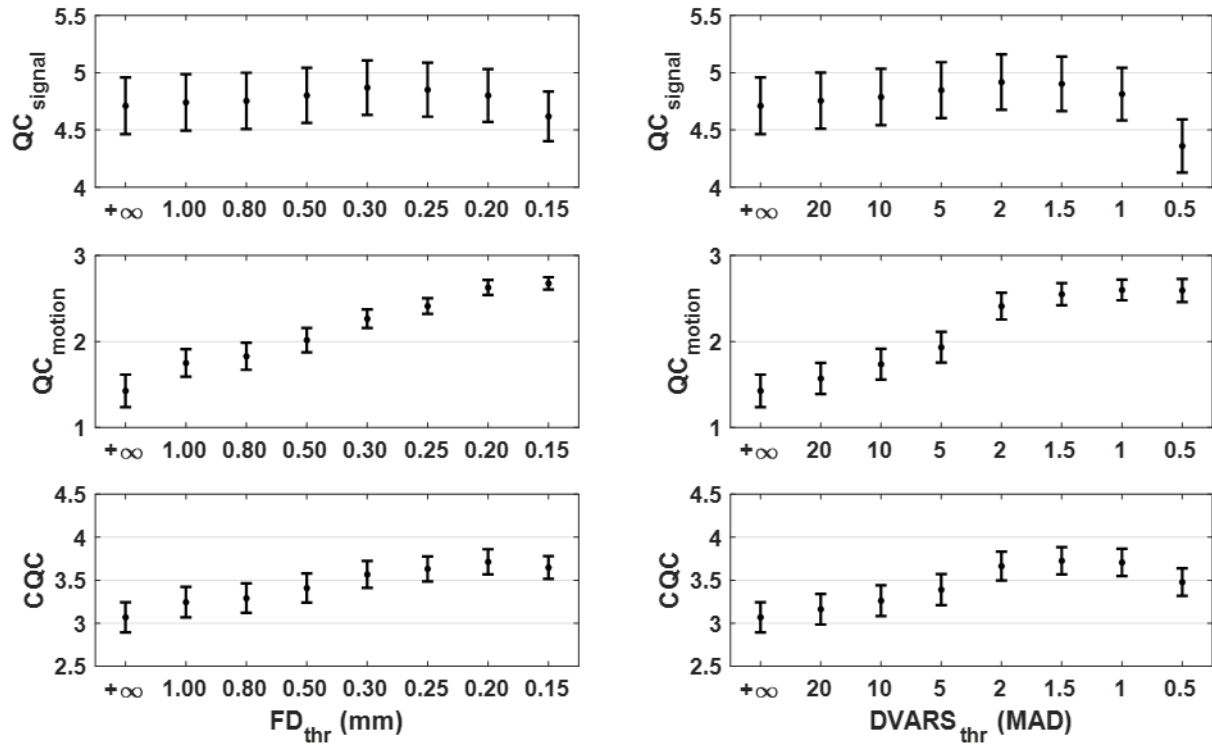


Suppl. Fig. 14. Evaluation of model-based NCTs using the fMRI data in the Seitzman (top) and MIST (bottom) parcel space. As with the data in the Gordon parcel space (Fig. 9), when the model-based regressors related to SLFOs, head motion and breathing motion were used without tissue-based regressors, the data quality as assessed with the three QC metrics QC_{signal} , QC_{motion} and CQC , was improved. However, when the set of nuisance regressors included the GS and the 200 components from WM, none of the model-based regressors was found to provide any additional improvement on the data quality.

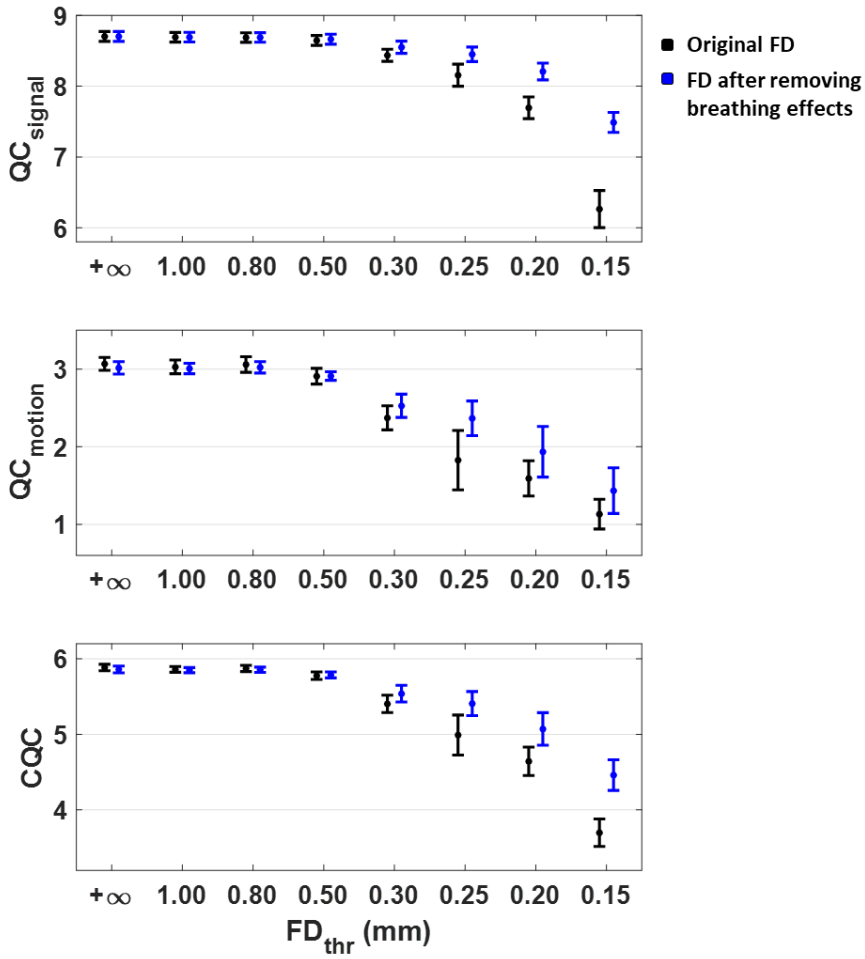


Suppl. Fig. 15. Effect of scrubbing in data quality for different threshold values on fMRI data in the Seitzman (top) and MIST (bottom) parcel space. When the data were preprocessed with the set of regressors WM_{GS}^{200} , scrubbing before the removal of the regressors did not provide any improvement in the combined summarized QC metric *CQC*. In contrast, thresholds of FD_{thr} below 0.50 mm led to a significant decrease of the *CQC* score. In the case of the *DVARS*, the *CQC* score was decreased when the threshold was below 1.5 MAD. However, typically, higher values of $DVARS_{thr}$ are used in the literature.

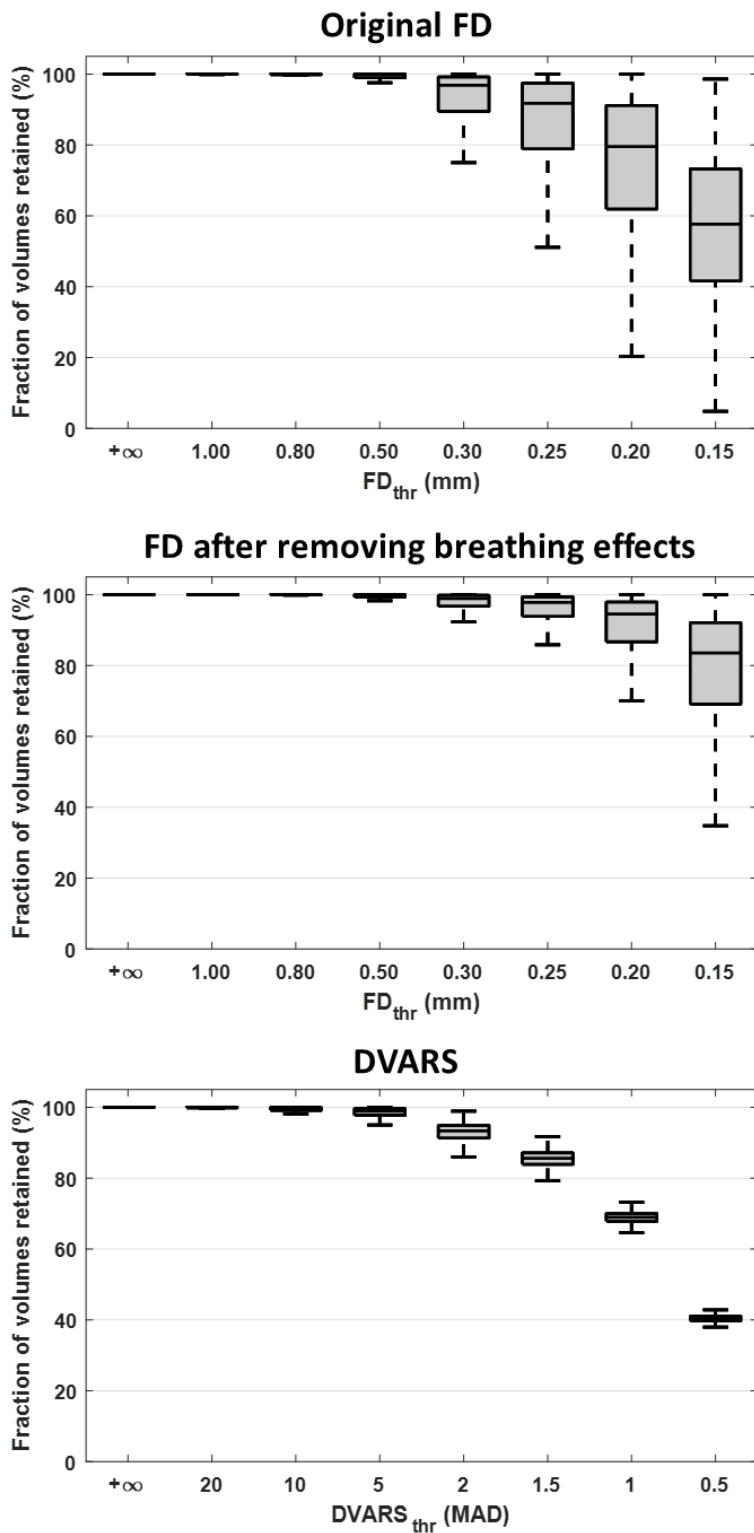
Effect of scrubbing for a *mild* pipeline (standard aCompCor)



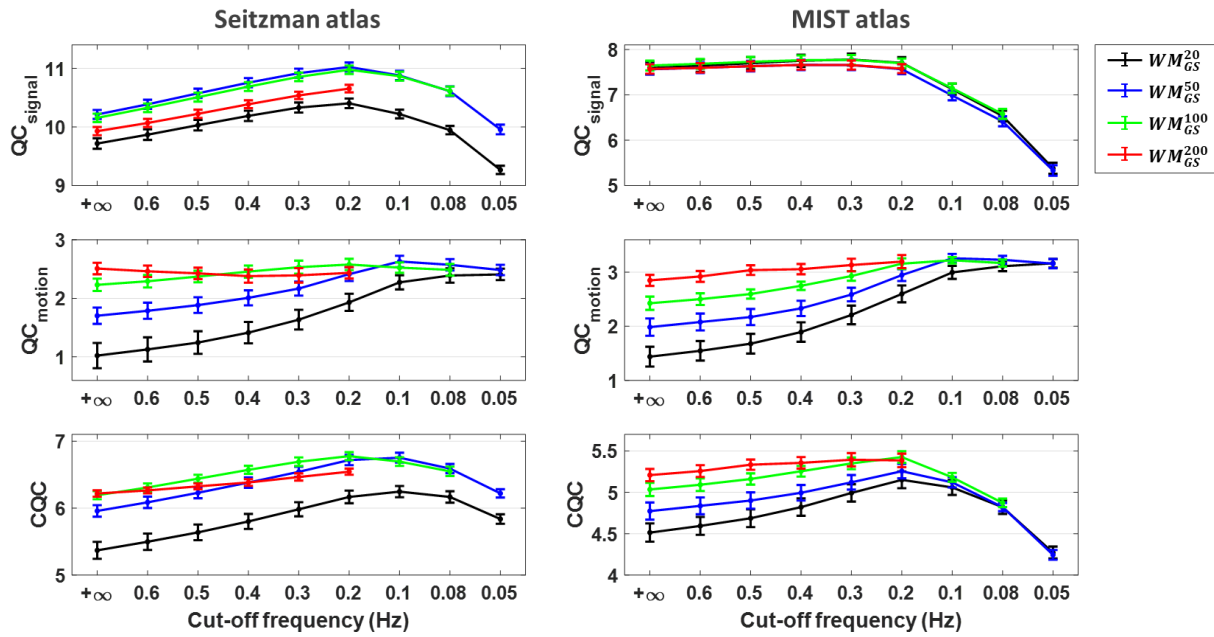
Suppl. Fig. 16. Effect of scrubbing for a mild pipeline that consists of removing five WM and five CSF regressors (Gordon atlas). When the data were preprocessed with the standard aCompCor approach (i.e. removal of five WM and CSF regressors), scrubbing before the removal of the regressors provided an additional improvement in the combined summarized QC metric CQC . The largest improvement was observed for a threshold FD_{thr} equal to 0.20 mm, which is commonly used in the literature (Power et al., 2015) and for a threshold $DVAR_{thr}$ equal to 1.5 MAD.



Suppl. Fig. 17. Effects of scrubbing for an *FD* trace that is free of breathing motion effects (Gordon atlas). To remove the effects of breathing motion from the *FD* trace, the six motion realignment parameters that are used in the estimation of *FD* were first filtered out for breathing-related fluctuations using 3rd order RETROICOR. When the data were preprocessed using WM_{GS}^{200} , scrubbing resulted in lower QC metric values, regardless of whether the influence of breathing in *FD* traces was removed or not. Removing the influence of breathing motion from *FD* traces was found to attenuate the effects of scrubbing, which is likely due to the smaller number of volumes marked as motion-contaminated for a given value of threshold FD_{thr} .

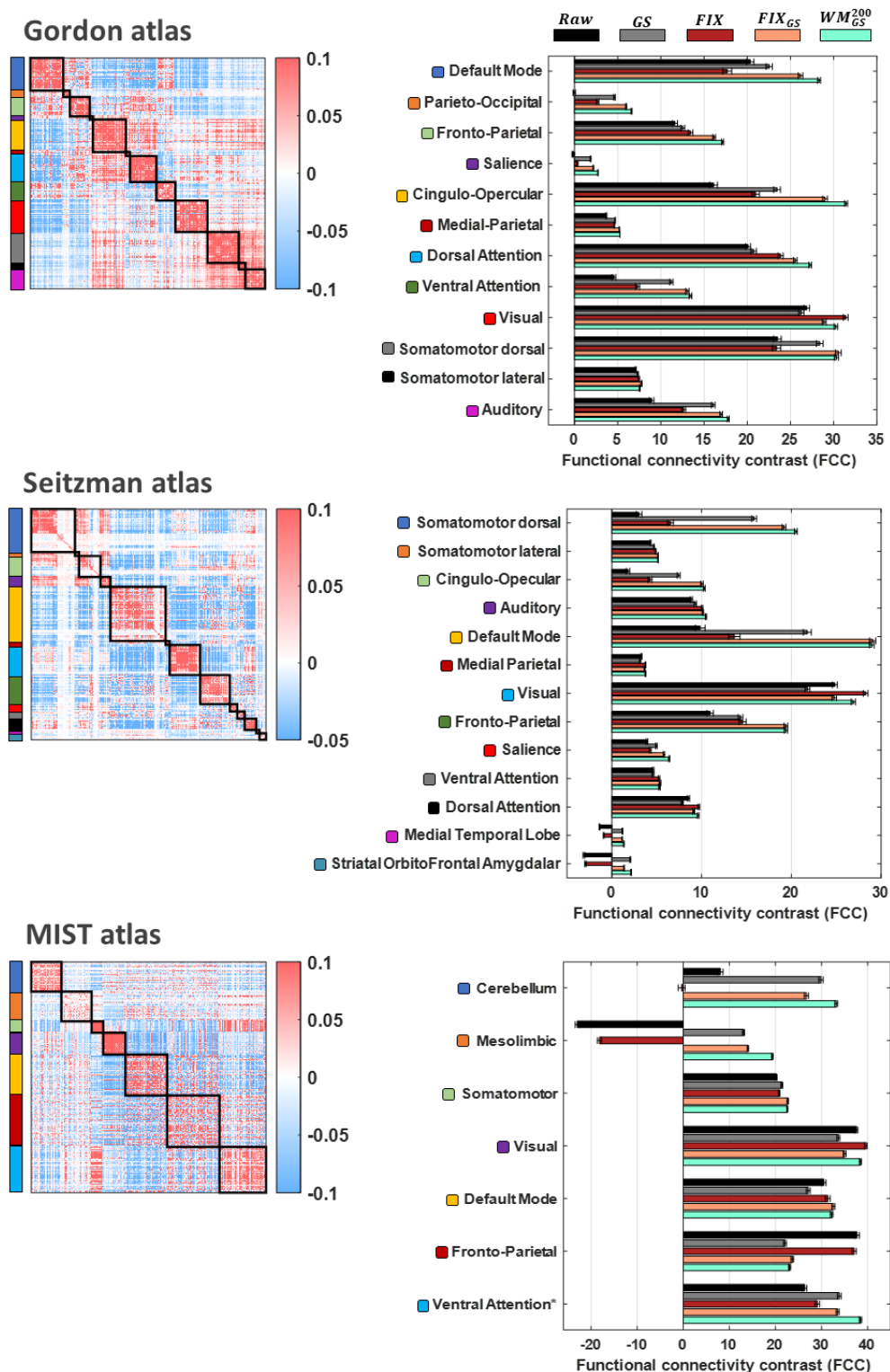


Suppl. Fig. 18. Fraction of volumes retained after scrubbing based on the original *FD* trace (top row), an *FD* trace free of breathing motion effects (middle row) and *DVARS* (bottom row). The bottom and top of each box correspond to the 25th and 75th percentiles of the sample distribution and the line in the box corresponds to the median (the outliers are not shown for ease of visualization).



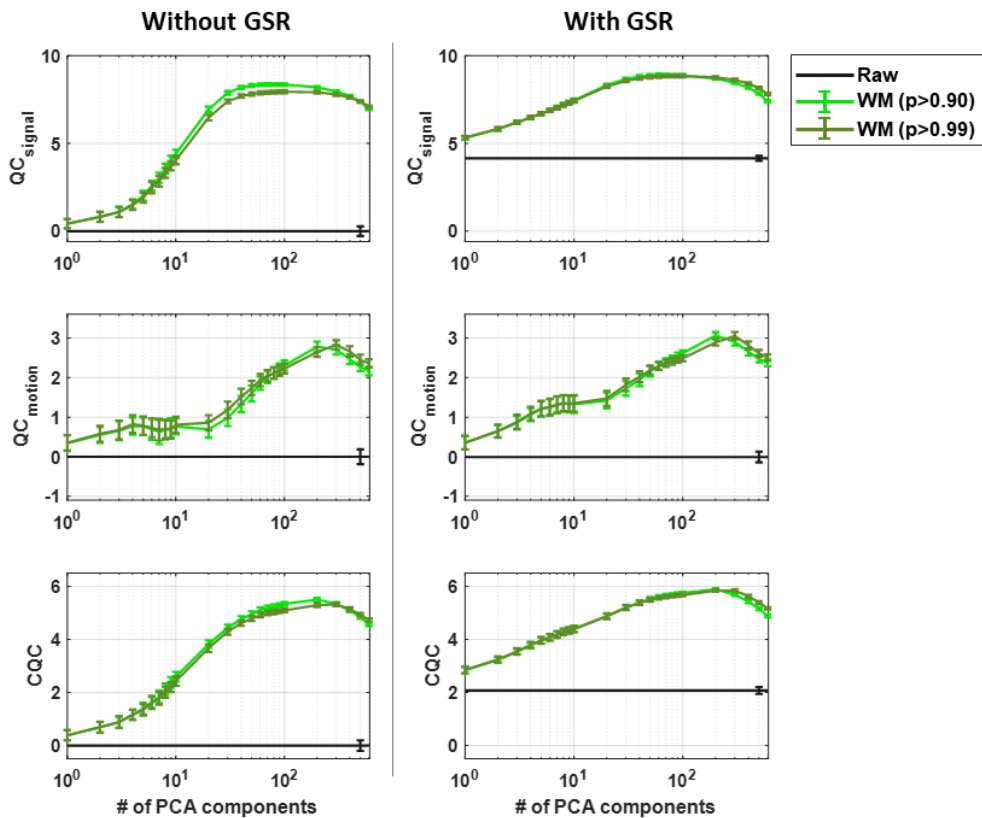
Suppl. Fig. 19. Effect of low-pass filtering in data quality for different cut-off frequencies on fMRI data in the Seitzman (left) and MIST (right) parcel space. For both atlases, the highest CQC score was achieved when low-pass filtering was done with a cut-off frequency of 0.2 Hz, and removal of nuisance regressors was done with WM_{GS}^{50} or WM_{GS}^{100} . In the case of the Seitzman atlas, similar levels of CQC score were also achieved with WM_{GS}^{50} and WM_{GS}^{100} at a cut-off frequency of 0.1 Hz. For both atlases, mild variants of WM denoising (i.e. WM_{GS}^{20} and WM_{GS}^{50}) benefited significantly from low-pass filtering in terms of QC_{motion} .

Identifiability of each network



Suppl. Fig. 20. Identifiability of each network for the three examined functional atlases (Gordon, Seitzman and MIST). The *FCC* score of each network was defined as the *Z*-statistic of the Wilcoxon rank-sum test related to the null hypothesis that WNEs of the examined network and BNEs in the FC matrix are samples from continuous distributions with equal medians. In the case of the Gordon and Seitzman atlases, there was larger variability in *FCC* scores across networks rather than across pipelines, which might be due to the variability in the number of parcels of each network. In the majority of networks, pipelines *FIX_{GS}* and *WM_{GS}²⁰⁰* exhibited the highest *FCC* scores. * The last network in the MIST atlas, apart from the ventral attention network, consists also of the salience network, the basal ganglia and the thalamus.

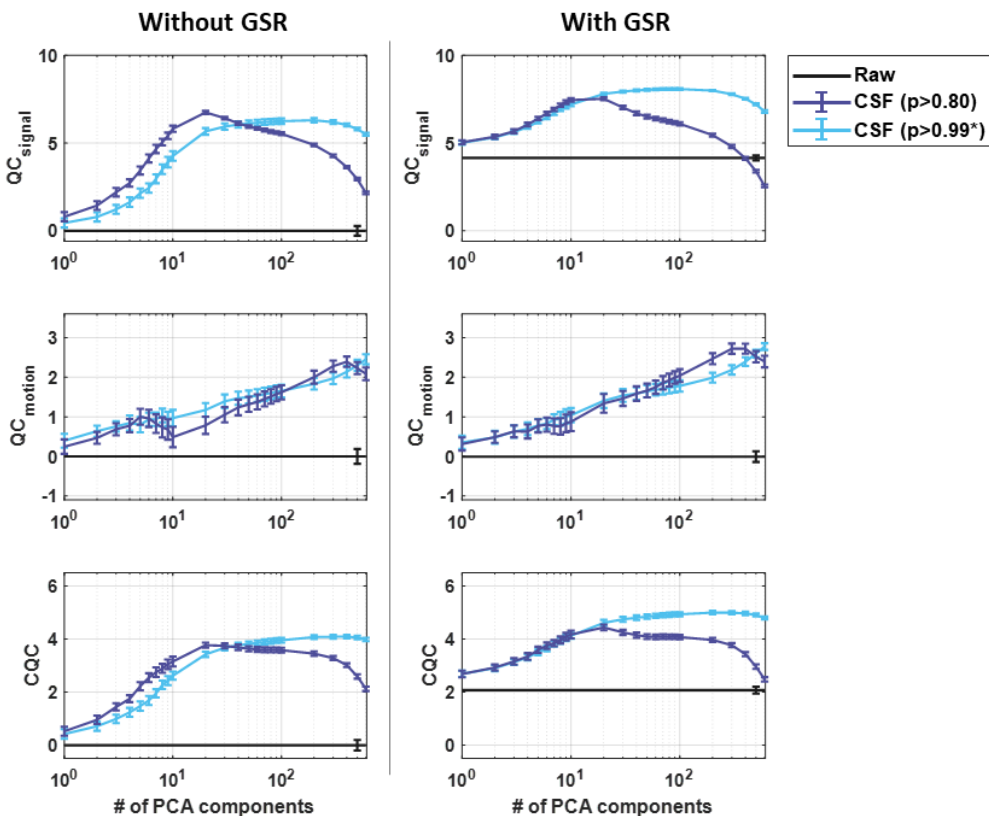
Performance of WM denoising for two different masks

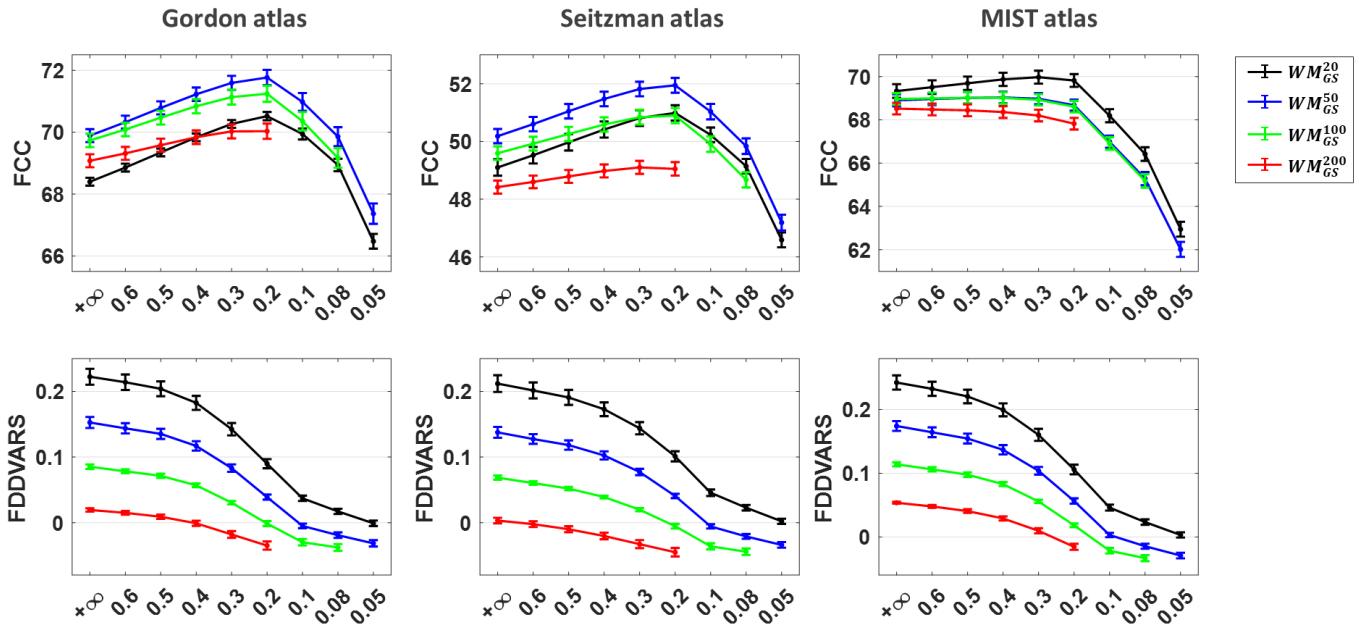


Suppl. Fig. 21. Performance of WM (top panel) and CSF (bottom panel) denoising for two different masks (Gordon atlas). For the case of WM denoising, using a stricter probability threshold for defining the mask of WM compartment ($p > 0.99$ instead of $p > 0.90$) did not have any significant impact on the performance of WM denoising. In contrast, for the case of CSF denoising with nuisance sets consisting of more than 20 regressors, a stricter probability threshold for defining the CSF mask ($p > 0.99$ instead of $p > 0.90$) led to substantially higher scores of QC_{signal} .

*For several scans, a probability threshold of $p > 0.99$ led to masks with an inadequate number of CSF voxels (<600) for performing principal component analysis (PCA), and thus, in those cases, the threshold was iteratively decreased (up to $p < 0.90$) until a sufficient number of CSF voxels was found.

Performance of CSF denoising for two different masks





Suppl. Fig. 22. Effect of low-pass filtering in FCC and FDDVARS on fMRI data in the Gordon (left), Seitzman (middle) and MIST (right) parcel space. For the Gordon and Seitzman atlas, the highest FCC score was achieved with WM_{GS}^{50} and a cut-off frequency of 0.2 Hz, whereas for the MIST atlas it was achieved with WM_{GS}^{20} and a cut-off frequency of 0.3 Hz. For all three atlases, a cut-off frequency lower than 0.2 Hz led to a significant decrease in FCC score. In the case of $FDDVARS$, the pipeline that yielded the lowest absolute scores (i.e. lowest levels of motion) varied across the three atlases. However, for all atlases, WM_{GS}^{100} with low-pass filtering at 0.2 Hz led overall to scores very close to zero (i.e. low levels of motion artifacts).